Motion Estimation Using Radiofrequency Scattering of a Parallel Transmit Coil for Cardiac Magnetic Resonance Imaging at 7T



Sven Hannes Franz Jaeschke

Keble College

University of Oxford

A thesis submitted for the degree of

Doctor of Philosophy

Trinity 2019

ABSTRACT

Magnetic resonance imaging (MRI) at ultra-high magnetic field strengths offers an increased signal-to-noise ratio (SNR) and has the potential to boost the MR image resolution. Cardiovascular applications remain challenging, as high-resolution image acquisitions are still too slow to capture a fast moving organ like the heart. Synchronisation of the acquisition to the heart motion is necessary to acquire an image over several consecutive heartbeats. The current gold-standard method for cardiac synchronisation is the electrocardiogram (ECG), which measures the electrical activity of the heart. Magnetohydrodynamic effects of the blood flow interfere with the ECG measurement and can affect reliable gating, which is particularly significant at higher magnetic field strengths.

The work of this thesis presents new motion estimation methods that are based on radiofrequency (RF) scattering of a parallel-transmit coil and directly assess the heart motion, independent of the electrical activity of the heart. A cardiac motion signal is derived with a high SNR and with a number of potential gating features, which have a high accuracy when compared to ECG gating. No additional motion-monitoring hardware is needed other than the commercially available pTx system. Different RF pulse designs are proposed to integrate the scattering measurements into the normal MR image acquisition to estimate cardiac and respiratory motion in real-time on the MRI scanner. The integrated cardiac-respiratory motion framework is combined with a new MR imaging acquisition strategy to acquire high-resolution, 3D images of the heart during free breathing.

ACKNOWLEDGMENTS

A DPhil is a truly life-changing experience and a challenging journey. This thesis would not have been possible without the generous support from so many individuals along my way.

First, I would like to thank my supervisor Aaron Hess for his incredible support and everlasting patience and engagement. Without his guidance and in-depth feedback, this DPhil would not have been achievable. I would also like to thank my supervisor Matthew Robson for the challenging and engaging advices that have helped me to improve my scientific work and never let me forget the bigger picture.

A big thank you to the entire OCMR Physics team at the John Radcliffe Hospital for all the advices, best-practice tips, the constant feedback as well as for the endless hours spent in the MRI, participating in one of my experiments.

Special thanks go to Aleksander Petrović for being my inspiration to apply to the University of Oxford. Without his help and encouragement, I would have not started the journey to pursue a DPhil.

I also gratefully acknowledge the funding from the Clarendon and Keble College de Breyne scholarship that lifted the financial burden and helped me to focus on my research.

Furthermore, I am extremely grateful for all my friends with whom I am not only sharing the best memories of my life but who also have helped and supported me in darker, troubling times. I could not have done it without them. Special thanks go to my DPhil family and closest friends Victoria Pereira, Andrew Linden,

Jack O’Sullivan, and Dylan James as well as to Henrike Puchta and Raphael Heim. Their rather spontaneous hugs, exceptional procurement skills, philosophic and countless stories, inspiring political discussions, numerous office kitchen coffee chats, and pub skills provided a reliable source of happiness beyond the scientific work.

I would also like to thank Lena Fuldauer for her trust, patience, love and encouragement during my final DPhil year and for enabling productive thesis writing retreats in the Alps.

Finally yet importantly, I like to thank my mother, father, and my sister for all their love and unconditional support throughout the years.

PUBLICATIONS

Peer-Reviewed Journal Articles

[1] S. H. F. Jaeschke, M. D. Robson, and A. T. Hess, “Scattering matrix imaging pulse design for real-time respiration and cardiac motion monitoring,” Magn. Reson. Med., vol. 82, no. 6, pp. 2169–2177, 2019.

[2] S. H. F. Jaeschke, M. D. Robson, and A. T. Hess, “Cardiac gating using scattering of an 8-channel parallel transmit coil at 7T,” *Magn. Reson. Med.*, vol. 80, no. 2, pp. 633–640, 2018.

Conference Abstracts

[1] S. H. F. Jaeschke, M. D. Robson, and A. T. Hess, “Prospective, Respiratory-Cardiac Gating for Free-Breathing, Cardiac CINE at 7T MRI Monitoring the Scattering Matrix”, ISMRM Workshop on Ultrahigh Field Magnetic Resonance, Croatia, 2019.

[2] S. H. F. Jaeschke, M. D. Robson, and A. T. Hess, “Monitoring the Complete Scattering Matrix of a Parallel Transmit Coil during Image Acquisition for Retrospective Cardiac Gating at 7T MRI”, In Proc. Intl. Soc. Mag. Reson. Med., 2018, p. 1006.

[3] D. Papp, **S. H. F. Jaeschke**, S. W. Rieger, S. Clare, and A. T. Hess, “Simultaneous detection of cardiac respiratory and rigid body head motion”, In Proc. Intl. Soc. Mag. Reson. Med. 26, 2018, p. 1168.

[4] S. H. F. Jaeschke, M. D. Robson, and A. T. Hess. “Evaluating the Influence of B1-Shimming on Contact-free Cardiac Gating using Scatter of a Parallel Transmit Coil at 7T MRI”, In Proc. Intl. Soc. Mag. Reson. Med., 2017, p. 1131

[5] S. H. F. Jaeschke, C. O’Brien, A. T. Hess, M. D. Robson. “Contact-Free Cardiac Motion Estimation Using the Scatter of a Parallel Transmit Coil at 7T MRI”, In Proc. Intl. Soc. Mag. Reson. Med., 2017, p. 3262

[6] S. H. F. Jaeschke, C. O’Brien, A. T. Hess, M. D. Robson. “Contact free cardiac gating using the transmit RF coil by monitoring the scattering matrix on a parallel transmit scanner”, the Annual Scientific Session of the Society for Cardiovascular Magnetic Resonance 2017, Washington, DC, USA.

Patents

[1] Sven Jaeschke, Aaron Hess, Matthew Robson. Inventor of US Patent Application; OUI Project Number: 15450, “Integrated Scattering Matrix Measurements, Patent pending.

[2] Aaron Hess, Matthew Robson, Chris Rodgers, **Sven Jaeschke**. “Methods for Extracting Subject Motion from Multi-transmit Electrical Coupling in Imaging of the Subject”, US Patent Application Serial No. 62/676,651, Oxford University Innovation (OUI) Project Number: 13465, patent filed.

Contents

LIST OF FIGURES ..... **XII**

LIST OF TABLES ..... **XV**

LIST OF ABBREVIATIONS ..... **XVI**

1 INTRODUCTION **1**

1.1 MOTIVATION 1

1.2 OBJECTIVES 3

1.3 OUTLINE OF THE THESIS 3

2 MAGNETIC RESONANCE IMAGING **5**

2.1 MR PHYSICS 5

2.1.1 Polarisation and Precession *5*

2.1.2 Excitation *6*

2.1.3 Relaxation *8*

2.1.4 The Bloch Equations *9*

2.2 IMAGE FORMATION 9

2.2.1 Gradient Fields and Gradient Echo *9*

2.2.2 Slice Selection *12*

2.2.3 In-plane Localisation: Frequency and Phase Encoding *14*

2.2.4 k-Space *15*

2.2.5 Resolution and FOV *17*

2.2.6 MR-Hardware *18*

2.3 ULTRA-HIGH FIELD MRI 19

2.3.1 Advantages and Challenges *19*

2.3.2 Parallel Transmit RF Coils *20*

2.4 RADIOFREQUENCY COILS FOR UHF-MRI 21
2.4.1 Designs of RF Coil Elements 21
2.4.2 Tuning and Matching 22
2.4.3 Q-Factor, Coupling and Scattering Parameter 24
2.4.4 Complex Conductivity of Tissue and the Scattering Matrix 28

3 MR IMAGING OF THE HEART 30
3.1 ANATOMY, PHYSIOLOGY AND PATHOLOGY OF THE HEART 30
3.1.1 Anatomy of the Heart 30
3.1.2 The Cardiac Cycle 31
3.1.3 Electrical Activity of the Heart and the Electrocardiogram 34
3.1.4 Arrhythmias of the Heart 36
3.2 CARDIOVASCULAR MRI 40
3.2.1 Image Positioning and Slice Orientations 40
3.2.2 Respiratory and Cardiac Motion in CMR 41
3.3 MR SYNCHRONISATION 42
3.3.1 Cine Imaging 42
3.3.2 Prospective Triggering and Retrospective Gating 44
3.3.3 Electrocardiogram Trigger: The Magneto-Hydrodynamic Effect 46
3.4 DEALING WITH MOTION: EXISTING TECHNIQUES 48
3.4.1 Raw MR-Data based Motion Estimation 49
3.4.2 Image-based Motion Methods 50
3.4.3 External Devices and Sensors 51
3.4.4 RF Coil and Electromagnetic Properties-based Motion Estimation 52

4 CARDIAC MOTION ESTIMATION USING RF SCATTERING OF AN PTX COIL .. 53

4.1 THEORY 54

4.2 MATERIALS AND METHODS 56

4.2.1 In-vivo Experiments 56

4.2.2 Scattering Matrix Measurements 56

4.2.3 Scattering Coefficients 57

4.2.4 B_1^+ Shim and Scattering Coefficients 58

4.2.5 Scattering Coefficients Measurement in Retrospective Cine 59

4.2.6 Cardiac Signal Extraction Algorithm 59

4.2.7 Gating Features from Cardiac Signal 61

4.2.8 Evaluation of Gating Accuracy 63

4.3 RESULTS 64

4.4 DISCUSSION AND CONCLUSION 70

4.5 SUMMARY 73

5 S-MATRIX IMAGING PULSE DESIGN FOR REAL-TIME RESPIRATION AND CARDIAC MOTION MONITORING 74

5.1 INTRODUCTION 75

5.2 PULSE DESIGN FOR S-MATRIX MEASUREMENTS 76

5.2.1 Frequency Division Multiplexing 76

5.2.2 Time Division Multiplexing 77

5.2.3 Code Division Multiplexing 78

5.3 CARDIAC AND RESPIRATORY MOTION ESTIMATION 80

5.3.1 Cardiac Motion Estimation 80

5.3.2 Respiratory Motion Estimation 80

5.3.3 Prospective, Dual Respiratory-Cardiac Gating 81

5.4 IN VIVO EXPERIMENTS AND DATA ACQUISITION 82
5.4.1 RF Pulse Design Evaluation 83
5.4.2 Prospective Image Acquisition 84
5.5 RESULTS 86
5.5.1 Scattering Matrix Measurements: Monitoring Power and Image Artefacts 86
5.5.2 Physiological Motion Estimation and Prospective Image Acquisition 88
5.6 DISCUSSION AND CONCLUSION 90
5.7 SUMMARY 93
6 PROSPECTIVE *K*-SPACE SAMPLING STRATEGY FOR COMPRESSED SENSING CARDIAC CINE DURING FREE BREATHING 94
6.1 OVERVIEW OF FAST, 3D IMAGING STRATEGIES 95
6.2 *K*-SPACE UNDERSAMPLING PATTERN AND TRAJECTORY 97
6.2.1 K-Space Sampling Pattern 98
*6.2.2 **CI**ustered, Randomly **O**rdered **C**artesian **K**-Space (CLOCK) Trajectory ... 99*
6.2.3 Simulation of Motion and Influence on k-space Sampling Pattern 104
6.3 HIGH-RESOLUTION CARDIAC CINE FRAMEWORK 107
6.3.1 Compressed Sensing Reconstruction 107
6.3.2 Motion Estimation and Navigation 107
6.3.3 Data Acquisition 108
6.3.4 Image Reconstruction using Compressed Sensing 110
6.4 RESULTS 113
6.4.1 Overview of Physiological Traces used in Simulations 113
6.4.2 Simulations of K-Space Trajectories in the Presence of Motion 115
6.4.3 Phantom Measurements and Eddy Current Effects 120
6.4.4 High Resolution Cardiac CINE 121
6.5 DISCUSSION AND CONCLUSION 126
6.6 SUMMARY 131

7 SUMMARY AND RECOMMENDATIONS 132

7.1 SUMMARY OF CONTRIBUTIONS 132

7.2 RECOMMENDATIONS FOR FUTURE WORK 134

7.2.1 Advanced Cardiac Gating and Motion Adaptation 134

7.2.2 Application in Lower Field Strengths and Patients 135

7.2.3 Motion Monitoring beyond Cardiac MRI 136

APPENDIX A 138

APPENDIX B 139

APPENDIX C 144

BIBLIOGRAPHY 150

LIST OF FIGURES

Figure 2.1: Excitation of the magnetisation 7

Figure 2.2: A Gradient-Recalled Echo sequence diagram 11

Figure 2.3: Example of a slice-selective excitation 13

Figure 2.4: An example of in-plane spatial encoding 15

Figure 2.5: Common 2D *k*-space sampling trajectories 17

Figure 2.6: Different RF-coil element types 22

Figure 2.7: Simplified, single RLC-circuit model of a RF coil 23

Figure 2.8: An *N*-port electrical network. 25

Figure 2.9: Example of a 2-port electrical network with S-matrix elements. 27

Figure 2.10: Simulated conductivity distribution in the human body 29

Figure 3.1: Anatomy of the heart 31

Figure 3.2: The Wiggers diagram 33

Figure 3.3: The electrical network of the human heart 36

Figure 3.4: Gradient Recalled Echo images of the heart at 7T MRI 41

Figure 3.5: Cardiac cine imaging with segmented *k*-space data acquisition 44

Figure 3.6: Prospective cardiac triggering/gating 45

Figure 3.7: The magneto-hydrodynamic effects on the ECG signal 48

Figure 4.1: Example measurement of the S-matrix 57

Figure 4.2: Different gating features and underlying traces 62

Figure 4.3: The extracted cardiac signal using the scattering coefficients and the scattering matrix 65

Figure 4.4: Histogram of the standard deviation of the difference in trigger time 66

Figure 4.5: Scatter plot of the RR-interval and the peak-to-peak feature interval 67

Figure 4.6: Boxplot of the difference between the gating features and ECG trigger....68
Figure 4.7: Short-axis, mid-ventricular slice and temporal profiles of a retrospectively reconstructed cine 70
Figure 5.1: Example of overlaid imaging and S-matrix RF pulses. 79
Figure 5.2: Diaphragm position extraction 81
Figure 5.3: Example of two selected cardiac cycles and the prospectively measured cardiac motion 82
Figure 5.4: S-Matrix gated images....86
Figure 5.5: SNR for different monitoring energy 87
Figure 5.6: Influence of movements of body extremities....89
Figure 5.7: Four-chamber view of a prospectively, cardiac gated 2D cine during breath hold and free breathing....90
Figure 6.1: An example Poisson-disc *k*-space sampling pattern with variable density 99
Figure 6.2: Clustered, 3D undersampled *k*-space pattern....100
Figure 6.3: CLOCK sampling trajectories 103
Figure 6.4: Example trajectories for CASPR-Tiger 106
Figure 6.5: The definition of the 2D motion states 108
Figure 6.6: Cardiac-resolved images using different regularisation parameter....112
Figure 6.7: Example motion state evaluation....114
Figure 6.8: Point-Spread-Functions and incoherence measures 116
Figure 6.9: Comparison of t Point-Spread-Functions and incoherence measures for different *k*-space trajectories with a target undersampling factor of $R = 4$ 117
Figure 6.10: Comparison of t Point-Spread-Functions and incoherence measures for different k-space trajectories with a target undersampling factor of $R = 2$ 118
Figure 6.11: Comparison of CLOCK and CASPR at end-expiration....119
Figure 6.12: Phantom measurements using different 2D CLOCK trajectories....120

Figure 6.13: Representative coronal images acquired in volunteer 1.....122
Figure 6.14: Representative coronal images acquired in volunteer 2.....122
Figure 6.15: Representative coronal images acquired in volunteer 3.....123
Figure 6.16: Transversal views of the 3D image data set acquired on volunteer 2....123
Figure 6.17: Line profiles of coronal images at end-expiration of volunteer 2.....124
Figure 6.18: Respiratory and cardiac resolved 2D cine images from volunteer 3.....125
Figure 6.19: Retrospective, respiratory re-binning of two end-inspiration bins 129
Figure 8.1: Mid-ventricular, short-axis view and temporal profiles of all breath hold cines reconstructed using the scattering coefficients 138
Figure 9.1: Example of strong inspiration/expiration events.....139
Figure 9.2: Example of two strong inhalation events.....140
Figure 9.4: Example images of a four-chamber view in volunteer 1.....141
Figure 9.3: Example images of a four-chamber view in volunteer 2.....141
Figure 9.5: Example images of a four-chamber view in volunteer 3.....141
Figure 9.6: Example images of a four-chamber view in volunteer 4.....142
Figure 9.7: Example images of a four-chamber view in volunteer 5.....142
Figure 9.8: Example images of a four-chamber view in volunteer 6.....143
Figure 9.9: Example images in sagittal view in volunteer 7.....143
Figure 10.1: Prospectively acquired 3D *k*-space sampling pattern in volunteer 1 144
Figure 10.2: Prospectively acquired 3D *k*-space sampling pattern in volunteer 2 145
Figure 10.3: Retrospectively, respiratory re-binning in volunteer 2 146
Figure 10.4: Prospectively acquired 3D *k*-space sampling pattern in volunteer 3 147
Figure 10.5: 3D *k*-space pattern acquired on volunteer 3, after retrospective re-binning in the respiratory domain 148
Figure 10.6: 2D *k*-space sampling pattern in volunteer 3.....149

LIST OF TABLES

Table 1: Summary Statistics for Gating Features 69

LIST OF ABBREVIATIONS

ADC	Analog-To-Digital Converter
CDM	Code Division Multiplexing
CLOCK	**Cl**ustered, Randomly **O**rdered **C**artesian ***K***-Space
CMR	Cardiovascular Magnetic Resonance Imaging
DAC	Digital-To-Analog Converter
Dico	Directional Coupler
ECG	Electrocardiogram
FDM	Frequency Division Multiplexing
FID	Free Induction Decay
FOV	Field Of View
GRE	Gradient-Recalled Echo
MHD	Magnetohydrodynamic
PSF	Point-spread Function
pTx	Parallel Transmit
RF	Radiofrequency
RMSE	Root Mean Squared Error
RSA	Respiratory-Induced Arrhythmia
SAR	Specific Absorption Rate
SNR	Signal-To-Noise Ratio
SPR	Side-lobe-to-Peak Ratio
TDM	Time Division Multiplexing
TR	Repetition Time
UHF	Ultra-High Field

CHAPTER 1
INTRODUCTION

Magnetic Resonance Imaging (MRI) is a non-invasive imaging modality that has become one of the most powerful diagnostic tools in modern medicine. MRI has several advantages over other imaging modalities as it does not use ionizing radiation, provides freely selectable image orientation, and has an excellent soft-tissue contrast.

In cardiology, MRI has been used to acquire high-resolution anatomy as well as functional and physiologic data of the heart. These measurements include myocardial and vessel anatomy, blood flow, cardiac function, tissue characterisation, and perfusion of the heart muscle [1]–[3]. The large number of clinical applications and the high flexibility of MRI led to a rapid extension of new and emerging MRI techniques with improvements in image acquisition speed, image quality, and image resolution [4].

1.1 Motivation

For many cardiovascular MRI applications, however, physiological motion and a reliable monitoring of such remains the major challenge for high quality imaging. Long, free-breathing image acquisitions suffer from blurring and ghosting artefacts that are induced by respiratory motion [5]. As simple breath holds limit the acquisition time (<20 s) and are often not feasible for patients, diaphragm

navigators are a common solution for respiratory gated and tracked acquisitions [6]. Diaphragm image navigators require additional, low-resolution images that will subsequently prolong the overall scan time in free-running acquisitions. Image sequence-based methods can estimate cardiac and respiratory motion from the image acquisition data but are limited to specific measurement trajectories [7] or need image sequence modifications [8]. External devices, such as respiratory bellows, can measure chest movements but will increase patient setup time and need careful adjustments for a reliable motion tracking [9], [10]. The current gold standard cardiac gating method, the electrocardiogram (ECG), has been used extensively to monitor the electrical heart activity. However, the ECG can be cumbersome to setup in some patients because of the magneto-hydrodynamic effects that overlay the electric fields from the heart and disrupt the ECG measurement [11], [12]. Successful ECG gating is possible but it frequently requires lead re-positioning [13], leading to an increased setup time. Missed or false ECG triggers can increase the scan time or significantly degrade image quality. This is particularly apparent at MRI with higher magnetic field strengths.

For the clinical use of ultrahigh-field cardiac MRI, it is critical to enable a practical gating alternative. In the recent years, a number of different methods have been developed that follow different approaches to overcome the limitations of ECG gating. However, there remains a need for a cardiac gating method that is widely applicable, is independent to the image acquisition strategy, does not require additional monitoring hardware, and does not need expert setup.

1.2 Objectives

The main objective of the work undertaken in this thesis was to acquire high quality, high-resolution images of the heart without using an electrocardiogram or any other external motion-monitoring devices, by monitoring the changes in the radiofrequency scattering of a parallel transmit coil at 7T MRI.

For this, specific objectives were:

- To identify and to explore the changes in radiofrequency scattering of a parallel transmit coil that are caused by cardiac and respiratory motion.
- To develop an accurate and robust cardiac trigger that is independent to the MR image sequence.
- To integrate scattering matrix measurements into normal MR imaging for real-time motion estimation without alternating the image sequence timing.
- To establish a free breathing imaging framework and acquisition strategy to acquire high-resolution cardiac MR.

1.3 Outline of the Thesis

The remainder of this thesis is organised as follows:

Chapter 2 describes the fundamental magnetic resonance physics and the principles of magnetic resonance imaging as well as the use of radiofrequency coils for imaging and their electromagnetic properties.

Chapter 3 gives an overview of the anatomy and physiology of the heart and the most common arrhythmias. A brief description of cardiovascular MRI is

given along with an overview of existing respiratory and cardiac motion monitoring techniques, including the electrocardiogram.

Chapter 4 establishes a method to extract a cardiac signal from the radiofrequency scattering of a parallel transmit coil using scattering matrix (S-matrix) or scattering coefficient measurements. The quality of the derived cardiac signal and the accuracy of the developed trigger algorithm is evaluated for its use for retrospective cardiac gating and is compared against the electrocardiogram.

Chapter 5 develops and evaluates three different RF pulse designs that simultaneously excite for imaging and measure the S-matrix to generate real-time motion signals without prolonging the MR image sequence. A prospective, dual cardiac-respiratory motion navigation framework is presented and is tested for free breathing cardiac MRI.

Chapter 6 proposes a flexible and highly efficient 3D Cartesian *k*-space sampling strategy for high-resolution 3D cardiac imaging during free breathing. The proposed sampling strategy is optimised for a compressed sensing image reconstruction and is compared to free-running and ungated acquisition strategies in simulations and demonstrated in vivo.

Chapter 7 summarises and reiterates the developments and findings of this thesis and gives recommendations for future work.

CHAPTER 2
MAGNETIC RESONANCE IMAGING

2.1 MR Physics

The basis of MRI is the nuclear magnetic resonance (NMR) effect [14], [15] and the quantum mechanical phenomenon of intrinsic nuclear magnetic momentums of subatomic particles. On a macroscopic scale, however, simple classic mechanical physics models can describe the magnetization and resonance phenomenon used for MR-imaging [16]. I will only consider the classical description in this chapter [17]–[19]. A more detailed description of the underlying quantum mechanical effects can be found in many textbooks [20].

2.1.1 Polarisation and Precession

The basis of the MR signal are nuclei with an odd number of protons and/or neutrons, which have an intrinsic angular magnetic momentum (spin). The most abundant nuclei in the human body is hydrogen, which consist of a single, positively charged proton and is used for most MR imaging. The majority of hydrogen is randomly orientated in the human body due to thermal motion, leading to no observable magnetization. However, in the presence of a strong, external magnetic field (denoted as B_0 in MRI), these nuclei have the tendency

to align to the magnetic field, producing a very small and measureable net magnetization. The magnitude of this net magnetization is proportional to the density of the nuclei in the tissue as well as to the applied magnetic field strength. In equilibrium, the net magnetization vector M_0 is parallel to the external field and its direction is often referred to as longitudinal axis. The plane perpendicular to it is denoted as transverse plane.

Additionally, the spins experience a precession around the external magnetic field direction. The angular precession frequency is proportional to the magnetic field strength and is defined by the Larmor equation:

$$\omega_0 = \gamma B_0 \tag{2.1}$$

Where γ is the gyromagnetic ratio, unique for the nuclei used (42.58 MHz/T for hydrogen [17]).

2.1.2 Excitation

The net magnetization can be displaced or “excited” by the application of a second, rotating magnetic field (B_1 field) in the transverse plane. A radiofrequency pulse generates the B_1 field and can be switched on and off. If the rotating B_1 field matches the Larmor frequency of the magnetization vector M_0, it is *on-resonance* and an excitation and displacement of the magnetization vector occurs. Torque forces that are perpendicular to the applied B_1 field and to the static magnetic field B_0, will cause this displacement and pull the magnetization vector into the transverse plane. The result is an oscillating magnetization component M_{xy} at the Larmor frequency. The final tipped rotation position or displacement of the net magnetization relative to the longitudinal axis

z depends on the amplitude and duration of the applied B_1 field and is described with the flip angle α and total duration T in the following equation:

$$\alpha = \gamma \int_0^T B_1(t)dt \tag{2.2}$$

Observing the excitation in a static frame of reference, the magnetization vector *M* appears to spiral out of the alignment with B_0. In a so-called *rotating frame* of reference, however, the coordinate system is rotating counter-clockwise around the z-axis with the angular frequency ω_0, such that the oscillation motion disappears. B_1 appears as a fixed magnetic field vector and the magnetization *M* slowly tips into the transverse plane (see Figure 2.1).

When a receiver coil, that is tuned to the Larmor frequency, is brought close to the precessing magnetization, the changing magnetic flux induces an electric current according to Faraday's law. The respective voltage changes are measured as complex MR signal $s(t)$.

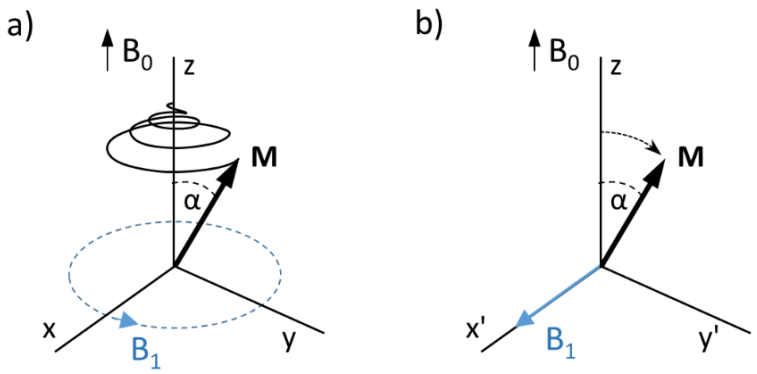


Figure 2.1: Excitation of the magnetisation vector *M* using a rotating magnetic field B_1 in the xy-plane (transverse plane), in presence of a static magnetic field B_0 along the longitudinal axis. a) Shows a laboratory frame of reference and b) shows a rotating frame reference. The flip angle *α* describes the degree of rotation of *M* into the transverse plane.

The resonance or Larmor frequency of most nuclei used in MRI and is in the radiofrequency range (i.e. 298 MHz for hydrogen at 7T). Therefore, the receive coils are often referred to as Radio Frequency (RF) coils. Sometimes the same RF coils are used for the detection of the MR signal and the transmission of the B_1 field.

2.1.3 Relaxation

Once the B_1 field is switched off, the magnetization spirals back to the equilibrium state M_0 and aligns with the static, external magnetic field. The decaying MR signal, measured by an RF coil in the transverse plane, is called Free Induction Decay (FID). The return process of the magnetization to the equilibrium state and the fast decay of the signal in the transversal plane is referred to as relaxation and consists of two main components, a longitudinal (T_1 relaxation) and transverse relaxation (T_2 relaxation). The longitudinal relaxation is the process by which all nuclei are brought back into alignment with the main magnetic field. It is characterised by a slow, exponential recovery of the longitudinal magnetization M_z to the equilibrium state M_0 described by

$M_z(t) = M_0 \left(1 - e^{-\frac{t}{T_1}}\right)$ with a time constant T_1

Transverse relaxation results from spin-spin interaction, where nuclei change their precession frequencies and dephase relative to each other. This is characterised by an exponential decay in the transverse magnetization $M_{xy}(t) = M_0\, e^{-\frac{t}{T_2}}$ with a time constant T_2. However, in a simple FID experiment, the signal decay is faster than T_2 and the time constant is known as T_2^*. A decreased T_2^* results from small, additional local B_0 field inhomogeneities that lead to locally

varying precession frequencies and hence a dephasing of the transverse magnetization. T_2^* relaxation effects are recoverable to T_2 using what is known as a spin echo experiment [21]. These time constants are important for MR image contrast as they are highly tissue dependent.

2.1.4 The Bloch Equations

The effects and interaction of the magnetization *M* with external fields *B*, as discussed above, can be described by a differential equation formulated by Felix Bloch in 1946 [14] that is now known as Bloch equation:

$$\frac{d\mathrm{M}}{dt} = \gamma(\mathrm{M} \times \mathrm{B}) - \frac{1}{T_1}(M_z - M_o) - \frac{1}{T_2} M_{xy} \tag{2.3}$$

with $M = \left[M_x \, M_y \, M_z \right]^T$ and *B,* the total external magnetic fields including the rotational B_1 field and static main magnetic field B_0.

2.2 Image Formation

The described effects of nuclear magnetic resonance are the basis for MR imaging of objects. In the previous section, an MR signal (FID signal) was generated over the whole volume of the sample and measured without spatial excitation or signal localisation.

2.2.1 Gradient Fields and Gradient Echo

In MR imaging, a spatial encoding is realised by superimposed magnetic fields on the longitudinal magnetic field B_0. Usually, MRI scanners have three additional electromagnetic coils, producing linear changing magnetic fields along the Cartesian axes in x-, y- and z-direction. Those additional magnetic fields are

denoted as gradients G_x, G_y and G_z, respectively. With a linearly changing magnetic field, each location along the specified axis experiences a different magnetic field strength. This leads to position-depending precession frequencies of the nuclei and thus to different resonance frequencies (see Larmor equation (2.1)) along the specified axis:

$$\omega(r) = \gamma\,(B_0 + G \cdot r) \tag{2.4}$$

where G is a three dimensional vector of the gradient amplitudes (typically measured in millitesla/meter (mT/m)) and r the spatial location vector.

In the rotating frame of reference, the application of gradients and the resulting change in the precession frequency leads to a phase shift in the components of the transverse magnetization. The phase shift at any time at any point is given by the following equation:

$$\varphi(r,t) = \gamma \int_0^t G(\tau) \cdot r d\tau \tag{2.5}$$

Once the gradient is switched off, the accumulated phase difference remains unchanged until the transversal magnetization disappears with the T_2 decay or another gradient is applied. The amount of phase shift depends on the gradient amplitude and the duration of the gradient, and is often referred to as gradient moment.

The transverse magnetization component M_{xy} can be manipulated by intentionally dephasing the MR-signal after the RF excitation (FID signal). A gradient with equal moment but with opposite polarity can be used to rephase

the MR signal at a specific time t_{TE}, denoted as echo time [22]. This generates a so-called Gradient-Recalled Echo (GRE) (see Figure 2.2).

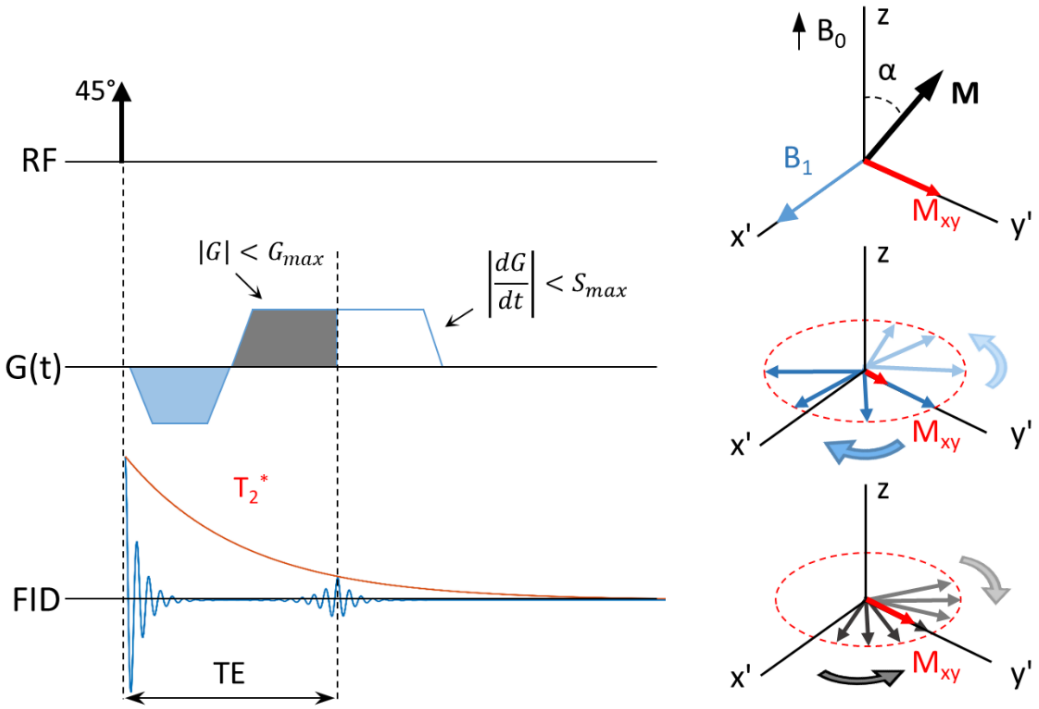


Figure 2.2: A Gradient-Recalled Echo (GRE) sequence diagram. The effect of a gradient-induced phase shift on the MR signal is shown with a simple sequence diagram on the left and the effects on the transverse magnetisation on the right. Spins along the gradient direction will experience position-dependent precession frequencies that result in a dephasing of the transverse magnetisation M_{xy} in a rotating frame of reference. A gradient with opposite polarity can be used to rephase the spins and recover the FID signal to create a gradient echo at time t_{TE}.

Gradient fields are generally small compared to the main static magnetic field B_0 (max. 80 mT/m at 7T [23]) and are switched on and off during imaging sequences. Peripheral nerve stimulation effects limit the peak gradient amplitude G_{max} and the time needed to achieve that peak amplitude (*slew rate*, S_{max}). Gradients are also used for slice-selective excitation, frequency encoding and/or phase encoding.

2.2.2 Slice Selection

Spatial selective excitation requires the simultaneous application of gradients and RF excitation with a specified frequency range (bandwidth). Slice-selective excitation is commonly done in MRI to acquire 2D images. A slice-select gradient (for example along the z-direction) varies the resonance frequency of the spins in the volume perpendicular to the intended slice. An RF excitation pulse is designed around a centre carrier frequency (f_0) that defines the middle of the slice (z_0). Only those spins with a resonance frequency that fall within the bandwidth of the RF pulse will resonate and be excited. A distinct bandwidth profile is desirable to excite the spins in a well-defined and sharp slice profile. Sinc-shaped waveforms are often used for RF pulses in MRI because of their rectangular or “top hat” function in the frequency domain (see Figure 2.3). However, an ideal Sinc-shaped RF pulse would require infinitive side lobes, which is impractical. Therefore, a compromise between the length of the RF pulse and the sharpness of ideal slice-profile is made using truncated RF pulses with apodization, which supresses the side-lobes (using digital filter like a Hamming window function) [24].

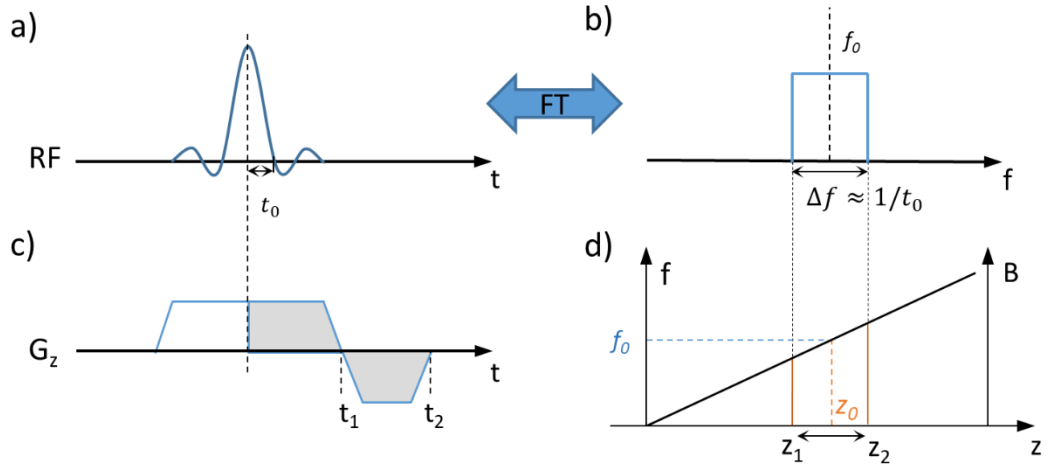


Figure 2.3: Example of a slice-selective excitation using a Sinc-shaped RF pulse and linear gradient G_z in z-direction. A) A truncated Sinc-shaped RF pulse generates a distinct frequency profile shown in B), which only excite the spins between z_1 and z_2 due to the spatially varying gradient G_z as in D). A negative rephasing gradient, with half of the slice-selection gradient area, is applied after the excitation process (t_1) to rephase the excited spins within the slice (t_2) as in C).

The thickness of the slice can be varied by changing the bandwidth of the RF pulse or the gradient field strength. The orientation of the slice is freely selectable in MRI using a combination of all three gradients.

During the slice excitation process, the spins experience a dephasing within the slice due to the slice-selection gradient (compare equation 2.5). A re-phasing gradient in the opposite direction and with half of the slice-selection gradient moment is needed to align the spins back to the centre frequency, such that all spins within the slice are in phase. A normal slice-selective excitation RF pulse is about 1-2 ms long and fast excitation RF pulses only 1 ms or less.

2.2.3 In-plane Localisation: Frequency and Phase Encoding

Frequency encoding is commonly used for spatial encoding and was first used to encode nuclear magnetic resonance signals for MRI [25]. Similar to the slice-selection gradient, the frequency-encoding gradient varies the precession frequencies of the excited spins linearly in space (e.g. in *x*-direction). The frequency-encoding gradient is often referred to as read-out gradient G_{FE} as it is usually applied during the MR signal measurements or read-out. Due to the gradient, the measured MR signal consists of a range of superimposed frequencies. A Fourier transform reveals and encodes the frequency content, which is linearly related to the spatial location of the spins along the gradient direction.

To add a second dimension of encoding, a **phase-encoding gradient** is introduced, which is often denoted as G_{PE} or G_y (when applied in y-direction in a Cartesian reference). The phase-encoding gradient is perpendicular to the frequency-encoding direction and is applied before the read-out gradient. The principle of phase encoding is the introduction of linear spatial variation of phases. As previously discussed, the application of a linear varying gradient field changes the precession frequency of nuclei, which can also be described as a phase shift in the frame of reference. The amount of phase shift is dependent on the gradient moment (duration and strength of the applied gradient) and the accumulated phase difference between nuclei remains when the gradient is switched off and the nuclei return to their original precession frequency. The measured, superimposed MR signals that originate from the nuclei at different locations vary for each of the different phase-encoding gradient moments and

enable a spatial encoding in the second dimension (see Figure 2.4). To reconstruct a whole image of spatial frequencies, several combinations of frequency- and phase-encoding steps are needed. I will further discuss this in the next section.

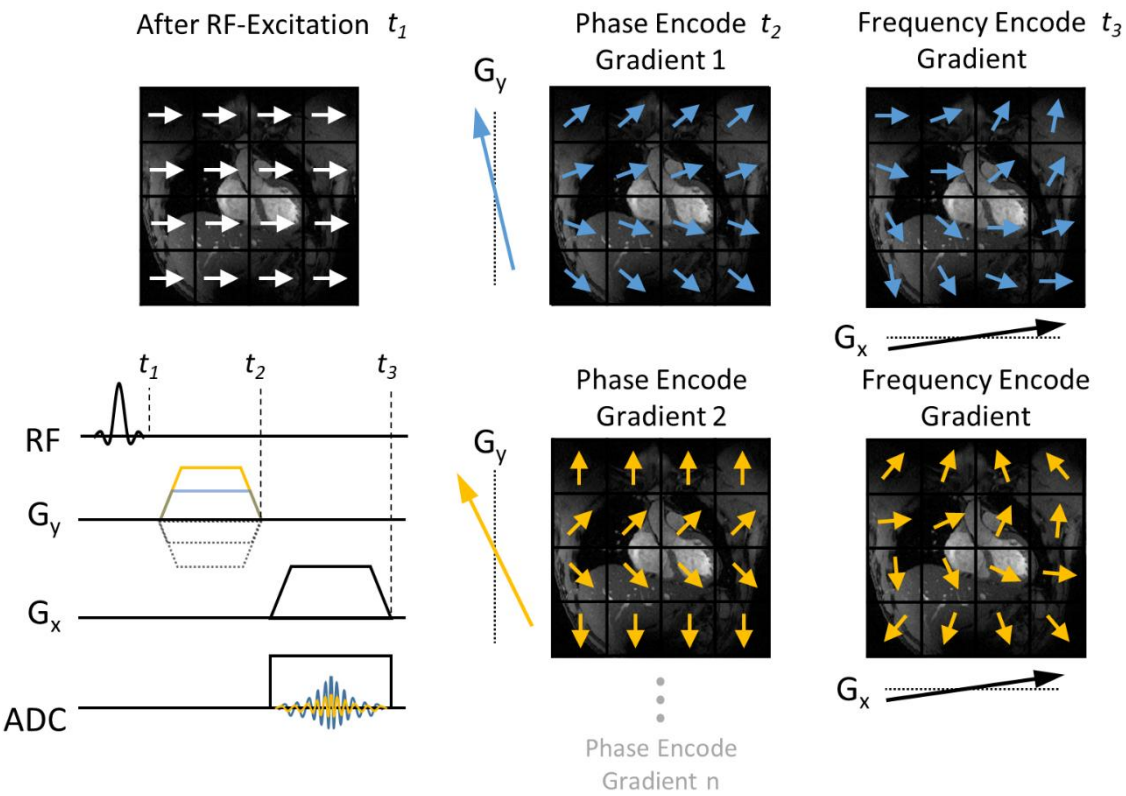


Figure 2.4: An example of in-plane spatial encoding using phase-encoding and frequency-encoding gradients for a 4×4 image matrix. The application of different phase-encoding gradients G_y introduces phase shifts along the y-axis, which result in different MR signals during the read-out gradient. In this example, four different phase-encoding gradients would be needed to fully encode the 4×4 image matrix.

2.2.4 *k*-Space

For the image acquisition, it is helpful to revisit the influence of gradient fields on location-dependent phase changes of the nuclei. The RF coil, used to measure the MR signal $s(t)$, integrates the magnetization from each position over the

whole imaging volume. In the frame of reference (demodulation of the Larmor frequency) and in presence of gradients, the received signal can be described as follows:

$$s(t) = \int M(r) e^{i\gamma \int_0^t G(\tau)\cdot r\, d\tau} dr \tag{2.6}$$

If we define $k(t) = \frac{\gamma}{2\pi} \int_0^t G(\tau)\, d\tau$

$$s(t) = \int M(r) e^{-i2\pi k(t) r} dr \tag{2.7}$$

Equation 2.7 describes a Fourier transform of the spatial magnetization with the spatial frequency parameter $k(t)$, or *k*-space. When *k*-space covers all spatial frequencies needed, an inverse, multidimensional Fourier transform would reveal the spatial magnetization $M(r)$ of the imaged object and thus the MR image.

There are rapid MR imaging techniques, which enable *k*-space measurements with a single RF excitation and which are commonly used for functional assessments in the brain [26], [27]. A fast decaying transverse magnetization, hardware as well as physiological constrains of encoding gradients (slew rate and maximum gradient amplitude) reduce the amount of *k*-space that can be measured after a single RF excitation. Therefore, most MR imaging methods sequentially acquire parts of *k*-space, using multiple RF excitations and multiple MR signal measurements. Common methods to acquire all spatial frequencies in *k*-space are shown in Figure 2.5. Linear data sampling on a Cartesian grid, where an incrementing phase encoding step (Δk_y) changes the acquired *k*-space line for each RF excitation, is commonly used due to its simple image

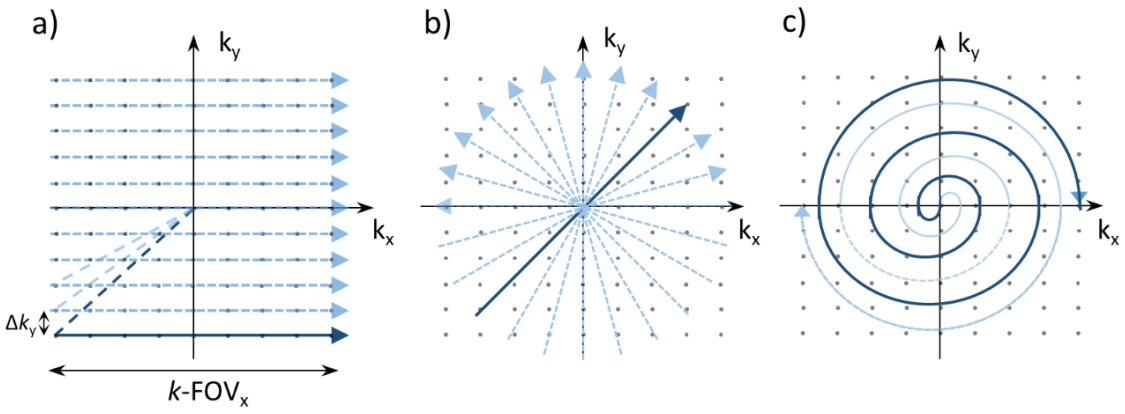


Figure 2.5: Common 2D *k*-space sampling trajectories on a Cartesian grid. a) Linear, b) radial, and c) segmented spiral sampling. Solid lines represent one read-out and the dotted lines represent all following acquisitions to fully measure *k*-space.

reconstruction with a fast Fourier transformation (FFT). Other common trajectories are radial sampling lines, which have shown to be more robust to motion [28] and can be highly under-sampled [29], [30], as well as spiral-like interleaved trajectories, which enable fast image acquisitions by making efficient use of encoding gradients and their hardware [31]. However, radial or spiral-like sampling trajectories require more computational demanding re-gridding (to the Cartesian coordinate system, [32]) or the use of filtered back-projection algorithms (radial trajectories, [25], [33]) for image reconstruction.

2.2.5 Resolution and FOV

The image resolution and the Field-Of-View (FOV) have a reciprocal arrangement in *k*-space and image space as a Fourier transform pair. High *k*-space values (outer parts of *k*-space) represent high frequencies and thus the small details in the image space. The image resolution Δx is defined by the maximum *k*-space value $\Delta x = \frac{1}{N\Delta k} = \frac{1}{FOV_k}$. Similarly, the FOV in image space is

defined with the sampling density Δk of *k*-space by $FOV_y = \frac{1}{\Delta k_y}$. A fundamental condition of sampling *k*-space is the Nyquist sampling criterion. Breaking the Nyquist sampling criterion will lead to reconstruction artefacts using classic Fourier-based image reconstruction.

2.2.6 MR-Hardware

In general, the basic components of an MRI system consist of the main magnet to generate the static magnetic field B_0, three gradient coils for spatial encoding, and radiofrequency coils that are used to generate the varying magnetic field B_1^+ and to measure the MR-signal.

Further, MR systems contain signal transmission and signal receive systems, which include RF waveform generators, Digital-to-Analog Converters (DAC), RF signal modulator, and RF power amplifier. The receive systems further include pre-amplifiers for MR-signal reception, transmit/receive switches, signal filters, and Analog-to-Digital Converters (ADC). At 7T MRI, additional safety measurement hardware includes directional couplers (DICOs), which are built into the transmission line of each transmit channel and measure the forward and reflected RF waveforms. Coupled to the transmission line, DICOs split off a portion of the RF signal, which is measured using the MR systems signal-receive systems and ADCs. DICOs monitor the power levels to calculate the energy dissipation into the subject and stop the measurements if the maximum power levels are violated or an unexpected RF waveform occurs.

For all MRI systems, an image reconstruction computer is used for image generation and a console is used as the user interface, from which the whole device is controlled and images are displayed.

2.3 Ultra-High Field MRI

MRI systems with a static magnetic field strength of $B_0 \geq 7\,\mathrm{T}$ are denoted as ultra-high field MRI.

2.3.1 Advantages and Challenges

One of the key advantages of such ultra-high field MRI systems is the higher nuclei polarisation or net magnetization *M* resulting from the high static magnetic field. This is turned into a higher Signal-to-Noise Ratio (SNR) and/or a higher Contrast-to-Noise Ratio (CNR) in the images, or to achieve a better spatial and/or temporal resolution [13], [34]–[37]. However, the increased field strength has some adverse effects. The high precession frequency at 7T ($f \approx 298\,MHz$) leads to shorter wavelengths for the B_1^+ excitation field (see equation 2.5). The high, dielectric constants of the body tissue shorten the effective wavelength further (to about 12 cm) and reduce it close to the size of the human torso, which can cause destructive resonance effects [38]. An increased RF power absorption and the reduction in the tissue penetration depth can lead to localised tissue heating and insufficient or inhomogeneous excitation fields [39]. Multi-channel, localised transmit and receive RF coils have been developed to overcome some of these limitations.

2.3.2 Parallel Transmit RF Coils

In parallel transmit (pTx) MR systems each RF transmit-channel has its own RF transmit coil driven by independent hardware enabling phase shifts, different RF amplitudes and/or individual RF waveforms.

The ability of applying individual RF waveforms enables more degrees of freedom in MR sequence design. This has been used to accelerate the RF excitation ([40]) using “Transmit SENSE”, an analogy to parallel reconstruction methods, as well as for localised, spatially-selective excitation using adapted RF waveforms [41]. Spatially and temporary varying RF pulses have been used to prevent potential destructive RF interferences and create a more homogenised B_1^+ excitation field using B_1^+ shimming [42]–[44] or tailored pulse design (k-t points [45], [46]). For B_1^+ shimming, the phase and/or amplitude of the RF pulses, which are transmitted on each different transmit element, are changed such that the overlying transmit fields result in a more homogenous excitation field over the region of interest. A subject-specific calibration scan is usually required to measure transmit sensitivity maps for each transmit element prior to the main imaging sequences.

In this thesis, the safety hardware of the pTx system is primarily used to monitor the parallel transmit RF coil elements, their electromagnetic properties and their interactions with the imaging subject. These properties and interactions are described in more detail in the following section.

2.4 Radiofrequency Coils for UHF-MRI

As previously described, RF coils are used to generate an oscillating magnetic field B_1^+ to excite spins in the body and to measure the MR signal. RF coils are grouped into transmit (Tx), receive (Rx), or transmit/receive (Tx/Rx) coils and differ in design and size; optimising the signal-to-noise ratio, power efficiency, B_1^+ excitation homogeneity, and field sensitivity or Field-of-View (FOV) of the coil. The latter has been used to distinguish between larger coils with a more homogenous and large excitation region (volume/body coils) and smaller coils with a more inhomogeneous excitation field but with a high surface sensitivity (surface coils).

2.4.1 Designs of RF Coil Elements

The most commonly used design for RF receiver surface coils is a set of loop coils in combination with a separate volume transmit coil. Various different loop sizes define the penetration depth and the sensitivity for deeper tissue regions. The combination of many small RF coils (i.e. in so-called phased arrays [47]) have enabled larger spatial coverage whilst maximising the SNR. Combined Tx/Rx surface coils are often used in UHF MRI as a result of the challenges in B_1^+-field homogeneity and the increased RF power absorption at higher frequencies, limiting the penetration depth into the tissue [39]. A common RF coil design at UHF MRI are transverse electromagnetic (TEM) coils, which have proven to provide a better efficiency in generating a B_1^+ excitation field in deeper tissue regions at high frequencies [48]. The TEM design is characterised by the transmission line element, a conductive cavity resonator, and the dielectric

substrate between them. Those transmission line elements can be made of coaxial transmission lines, strip lines or microstrip coil elements [34], [48]–[51]. Another common RF coil design are radiative, dipole antennas [52], [53]. Dipole antennas in MRI use split metallic strip line elements that are attached to dielectric substrate and are operated with a balanced signal ([54]). Compared to the TEM coil design, dipole antennas create a Poynting vector (orthogonal to the electric and magnetic field) that directs straight into the sample (see Figure 2.6). Transmit RF coil elements are usually combined to form a surface array and are placed close to the region of interest.

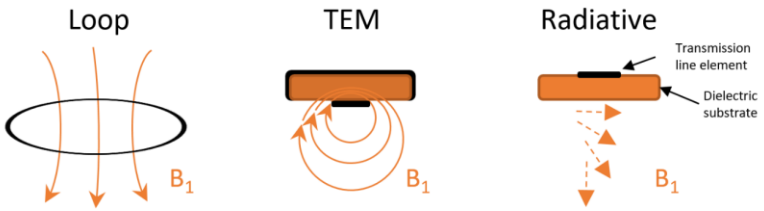


Figure 2.6: Different RF-coil element types and their B_1^+ field [54].

2.4.2 Tuning and Matching

Simplified, all MR coils can be described as a resonant electrical circuit that is tuned to the Larmor frequency and matched to the input impedance of the RF amplifier (typically 50 Ω) or receiving pre-amplifier (typically high impedance for receive-only coils), as shown in Figure 2.7. The circuit includes the conductive material/wire that forms the inductance L (e.g. wired loops), a capacitor in parallel to form an LC circuit (e.g. tuning capacitor C_T), and another adjustable capacitor in series to match the impedance to the RF amplifier or receiving pre-amplifier (e.g. matching capacitor C_M). The effective resistance R_{eff}, which is connected in series to the circuit, represents the electrical power losses in the circuit. R_{eff}

includes the resistance and power losses of the conductive material and the electric components of the coil R_C, the frequency-dependent RF coil radiation losses R_R, and the resistance that a RF coil experiences due to inductive coupling and power absorption from eddy currents generated by electrical fields in the sample R_S. These components are shown in the simple RF circuit in Figure 2.7.

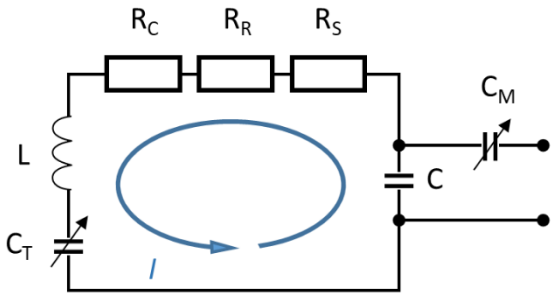


Figure 2.7: Simplified, single RLC-circuit model of a RF coil. Two tuning capacitors (C_T and C) fine tune the resonance frequency of the coil. The matching capacitor C_M transforms the impedance of the circuit to match the input impedance of the amplifier (e.g. 50 Ω). The different power losses of the RF coil at resonance frequency are represented by the resistive elements R_C, R_R, and R_S.

The tuning capacitor C_T is used to maximise the impedance of the parallel LC circuit to ensure an optimal signal transmission and reception at the Larmor frequency. The resonance of the RLC circuit is given by:

$$f_r = \frac{1}{2\,\pi}\sqrt{\frac{1}{LC_T} - \left(\frac{R_{\text{eff}}}{L}\right)^2} \tag{2.8}$$

During the RF pulse transmission, a mismatch in the impedances would disturb the optimal energy transfer on the transmission lines and result in a fraction of RF power not being transmitted into the subject but reflected back to the RF amplifier.

2.4.3 Q-Factor, Coupling and Scattering Parameter

The coil performance and efficiency can be measured by the dimensionless quality factor Q that describes the ratio of stored energy and power loss at the resonance frequency ω_r, given by the following equation:

$$Q = \frac{Maximum\ energy\ stored}{Energy\ dissipated\ per\ cycle} = \frac{\omega_r\, L}{R} \tag{2.9}$$

The Q-factor of the coil without the sample (unloaded, $R = R_c$) can be compared to the Q-factor when the sample is considered (loaded, $R = R_S + R_c$). The ratio of both Q-factors is an indicator of the sensitivity of the coil element:

$$Q_{ratio} = \frac{Q_{loaded}}{Q_{unloaded}} = \frac{R_S + R_c}{R_c} \tag{2.10}$$

Assuming that the radiative coil R_R losses are negligible, a good coil has a high Q_{ratio} with $R_S \gg R_C$, meaning it is sample resistance dominated.

As described above, RF coils are usually built into arrays to increase the field-of-view and homogenise the spatial sensitivity [47]. However, when RF coils with the same resonance frequency are close to another, mutual inductance effects occur, which affect the sensitivity at the resonance frequency and lead to signal transmission between coil elements. Careful placement of the coil elements [47], [55] and active detuning [51] can minimise the mutual inductance, which is often referred to as electromagnetic coupling.

A common way to analyse the electromagnetic properties of RF coil arrays, including their RF tuning and coupling effects, are scattering parameter (or S-parameter). S-parameter have been used to describe the electrical behaviour of linear electrical networks. In this thesis, the RF coil elements, which are placed

around the imaging sample, are seen as an *N*-port electrical network, where *N* is the number of RF coils or independent transmit channel. Kurokawa [56] defines the incident (transmitted) power wave a_i and the reflected power wave b_i at port *i* of such an N-port electrical network by:

$$a_i = \frac{V_i + Z_i I_i}{2\sqrt{|Re\ Z_i|}}\ , \qquad b_i = \frac{V_i - Z_i^* I_i}{2\sqrt{|Re\ Z_i|}} \tag{2.11}$$

With the voltage V_i and current I_i present at that port (see Figure 2.8). The current I_i directed into the network. Z_i is the impedance of the circuit connected to port *i*, and matches that of the transmission line (typically 50 ohm)

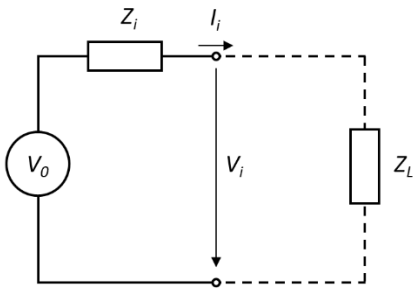


Figure 2.8: Apparent voltages, current, and impedance at port *i* of an *N*-port electrical network.

To simplify the power wave definitions, identical input impedances Z_0 at all ports (e.g. $Z_i = 50\ \Omega$) can be assumed. The ratio between a_i and b_i is described as scattering ratio s_i:

$$s = \frac{b_i}{a_i} \tag{2.12}$$

Using the definitions of a_i and b_i, and the relation of $V_i = Z_{L_i} I_i$, where Z_{L_i} is the apparent impedance of the load on coil *i*, the scattering ratio can also be expressed in terms of impedances, showing the dependency of electromagnetic coupling and RF coil loading:

$$s = \frac{Z_{L_i} - Z_0^*}{Z_{L_i} + Z_0} \tag{2.13}$$

For the perfectly matched coil ($Z_0 = Z_L$) the scattering coefficient becomes zero. For a linear, *N*-port electrical network, the relation between all incident and reflected power waves at all ports can be rewritten as a system of *N* linear equations:

$$\begin{aligned} b_1 &= S_{11}a_1 + S_{12}a_2 \\ b_2 &= S_{21}a_1 + S_{22}a_2 \end{aligned} \tag{2.14}$$

or in a matrix formulation ***S***:

$$\boldsymbol{b} = \boldsymbol{S}\,\boldsymbol{a}$$

$$\text{or} \begin{pmatrix} b_1 \\ \vdots \\ b_N \end{pmatrix} = \begin{pmatrix} S_{11} & \cdots & S_{1j} \\ \vdots & \ddots & \vdots \\ S_{i1} & \cdots & S_{ij} \end{pmatrix} \cdot \begin{pmatrix} a_1 \\ \vdots \\ a_N \end{pmatrix} \tag{2.15}$$

S is called scattering matrix or S-matrix. Individual S-parameter S_{ij} can be calculated when the individual power contribution from the incident wave a_j can be identified in the reflected power waves b_i. In a classical approach, this can be achieved by terminating all other ports using the reference impedance Z_0 for Z_L, resulting in total power dissipation for all other transmitted power waves, or by time-separated incident waves. Then, S_{ij} can simply be calculated by the ratio of the measured, reflected power wave on port i and the single incident wave a_j on port j for all $i \in \mathbb{N}, i \leq N$:

$$S_{ij} = \left.\frac{b_i}{a_j}\right|_{a_k=0\ \forall\ k\neq j} \tag{2.16}$$

The diagonal of the S-matrix represents the reflection for each RF coil, whereas the off-diagonal elements describe the mutual inductance (RF conducted from one port to another) between RF coil elements (see Figure 2.9).

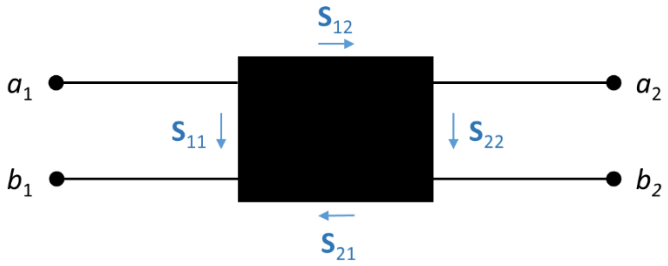


Figure 2.9: Example of a 2-port electrical network with S-matrix elements.

The S-matrix is symmetric when $S_{ij} = S_{ji}$ for all *i* and *j*. In general, most passive components in the RF circuit are bi-directional, whereas active components, such as the pre-amplifier, have directional dependencies that contribute to a quasi-symmetric S-matrix for MR coil arrays.

If it is not possible to identify or separate the fractional, reflected power b_i on port i, which originated from the incident power on port j, the measured returned power b_i on port i is the sum of all fractional, reflected power waves $b_i = \sum_{j=1}^{N} S_{ij}\, a_j$. The ratio of the measured reflection b_i and the incident wave a_i on the same channel i is herein denoted as scattering coefficient Γ_i [57]:

$$\Gamma_i = \frac{b_i}{a_i} = \frac{\sum_{j=1}^{N} S_{ij} a_j}{a_i}$$

$$\text{or} \begin{pmatrix} b_1 \\ \vdots \\ b_N \end{pmatrix} = \begin{pmatrix} \Gamma_1 & \cdots & \Gamma_N \end{pmatrix} \cdot \begin{pmatrix} a_1 \\ \vdots \\ a_N \end{pmatrix} \tag{2.17}$$

The S-matrix and the scattering coefficients are complex, frequency dependent, and non-unitary. They describe the power reflection, dissipation, and radiation of the forwarded power in the RF coil network.

2.4.4 Complex Conductivity of Tissue and the Scattering Matrix

The power dissipation of the RF coil array, described by the S-matrix, can result from either resistive coil losses (material and lumped elements) or resistive losses in the imaging sample (subject), as previously described by the resistances R_C and R_S, respectively.

The power dissipated in the imaging sample is proportional to the squared induced current density. The sample resistance R_S can be described by Ohm's Law assuming a unit current amplitude with the following volume integral [47], [58], [59]:

$$Z_{i,j} = \int_V \sigma(\vec{r}) \cdot \vec{E}_i(\vec{r}) \cdot \vec{E}_j(\vec{r})\, dV \tag{2.18}$$

where $\sigma(\vec{r})$ is the complex tissue conductivity distribution within the conductive volume of the imaging sample and $\vec{E}_i(\vec{r})$ the induced electrical field in the sample originating from a unit current amplitude in the RF coil *i* and coil *j*, respectively. The resistance for a single coil in isolation is described for $i = j$ using the complex conjugate of $\vec{E}_i$ for $\vec{E}_j$. The mutual inductance in a multi-coil array is described by $Z_{i,j}$ for all $i \neq j$. Thus, the dissipative power losses are dependent on the complex conductivity distribution and the effective volume of the imaging sample within the RF coil array.

The impendences of a multi-coil array can also be written in matrix form (Z-matrix). Assuming identical characteristic input impedance at each port, the Z-matrix relates to the S-matrix as follows [60]:

$$Z = (1_N + S)(1_N - S)^{-1} \tag{2.19}$$

where 1_N is the identity matrix.

For human MRI, various different tissue types are apparent in the field-of-view of the RF coils, each of which have a different complex conductivity, and contribute differently to the overall conductivity distributions described in equation 2.18.

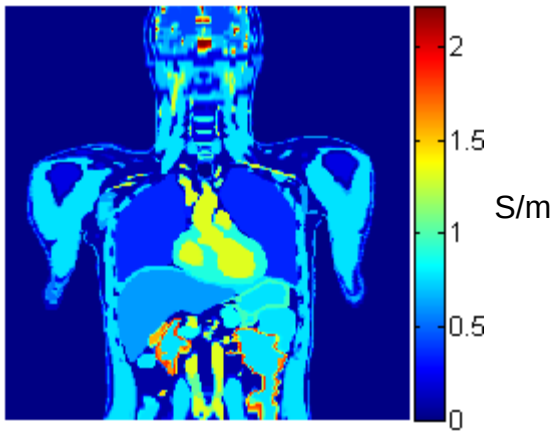


Figure 2.10: Simulated conductivity distribution in the human body for different tissue types at 7T ($f \approx 298\,MHz$). The heart muscle and the blood have a high conductivity compared to its surrounding tissue (e.g. the lungs and the liver).

CHAPTER 3
MR IMAGING OF THE HEART

3.1 Anatomy, Physiology and Pathology of the Heart

The human heart is a cone-shaped muscular pump, located in between the lungs in the middle mediastinum. Its lower surface lies on the diaphragm, the primary muscle of respiration that separates the abdomen from the chest. The average adult heart weights around 300g and beats approximately 100.000 times a day, continuously pumping blood around the circulatory system to deliver oxygen and nutrients and to assist in the removal of metabolic wastes in the human body.

3.1.1 Anatomy of the Heart

The heart consists of four chambers: the upper left atrium, the upper right atrium, the lower left ventricle, and the lower right ventricle (see Figure 3.1). The septum separates these ventricles. The heart is connected to the circulatory system via superior and inferior vena cava and the aorta. The lungs are connected to the heart through the pulmonary artery and vein.

Four heart valves separate the chambers and ensure unidirectional blood flow through the heart: two atrioventricular valves, the mitral and tricuspid valve, which are located between the atrium and the ventricles of the left and right heart,

and two semilunar valves, the pulmonary and aortic valve, which are located at the pulmonary artery and the aorta, respectively (see Figure 3.1).

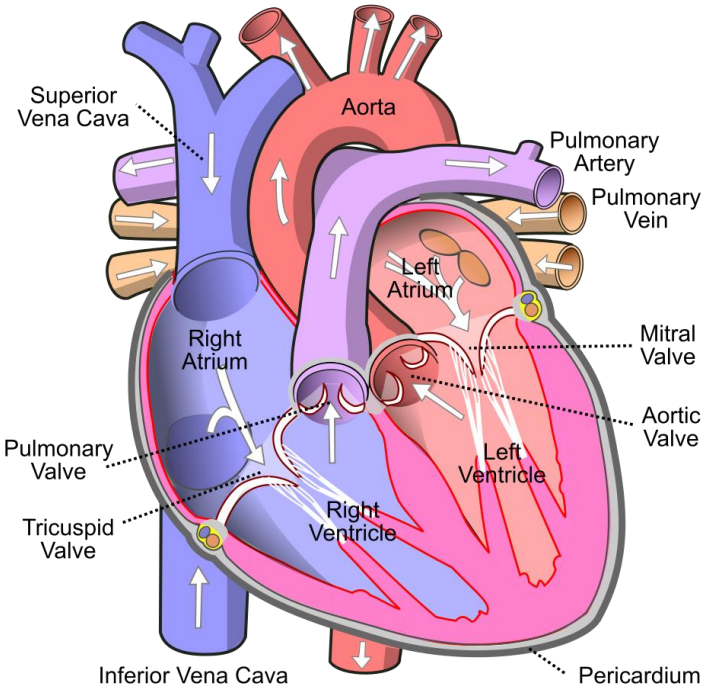


Figure 3.1: Anatomy of the heart. Frontal plane through the heart. Figure adapted from Wikimedia Commons “Diagram of the human heart” (CC-BY-3.0 license).

3.1.2 The Cardiac Cycle

The heart pumps blood through the circulatory system with periods of contraction (systole) and relaxation (diastole) of the atria and ventricles. There are three distinctive phases of the heart cycle: atrial systole, ventricular systole, and ventricular diastole. Before the cardiac cycle begins, relaxed atria and ventricles allow for a passive blood flow from the vena cava into the right atrium and from the pulmonary veins into the left atrium. Both atrioventricular valves are open so that blood flows unimpeded from the atria into the ventricles. The semilunar

valves are closed to prevent any backflow into the heart. The majority of ventricular filling happens with passive inflow during diastole (70-80%) [61].

Each cardiac cycle starts with the spontaneous generation of an action potential by the sinus node (described in more detail in Section 3.1.3). It causes a contraction of the atrial muscles (atrial systole), resulting in a so-called “atrial kick” when increased pressure loads the ventricles with the remaining 20 percent of filling [61]. The blood volume of the fully filled heart of about 110 to 120 mL is known as *end diastolic volume* (EDV) [61]. Figure 3.2 shows the different stages of the cardiac cycle with changes in the volume of the left ventricle as well as the pressure changes in the aorta, left ventricle, and in the left atrium, respectively. The atrial systole lasts about 100 ms and ends with the contraction of the ventricles (ventricular systole).

In the first, short part of the ventricular systole, the pressure in the ventricle rises above the pressure in the atria, resulting in the atrioventricular valves closing (the first heart sound). For another 30 to 50 ms, the pressure rises but no blood is ejected and the volume stays constant (isovolumetric contraction) [62]. The second part of the ventricular systole starts when the pressure in the ventricles reaches a level above the blood pressure in the aorta and pulmonary arteria (~80 mmHg and ~8 mmHg, respectively) and pushes the semilunar valves (pulmonary and aortic valve) open. A rapid ejection phase pumps about 70% of the blood into the circulatory system (ventricular fast ejection phase), followed by a period of slow ejection during the last two thirds of the ejection phase. The complete ventricular systole is about 270 ms long, with slight variation on the heart rate

[63]. The remaining blood volume in the ventricle, about 40 to 50 mL, at the end of the extraction phase is known as *End Systolic Volume* (ESV).

The ventricular diastole starts when the cardiac muscle begins to relax and the blood pressure in the ventricles drops below the pressure in the pulmonary arteria and aorta and the semilunar valves close (second heart sound). The pressure continues to fall but the volume stays constant as no further blood is ejected (isovolumetric relaxation) [64].

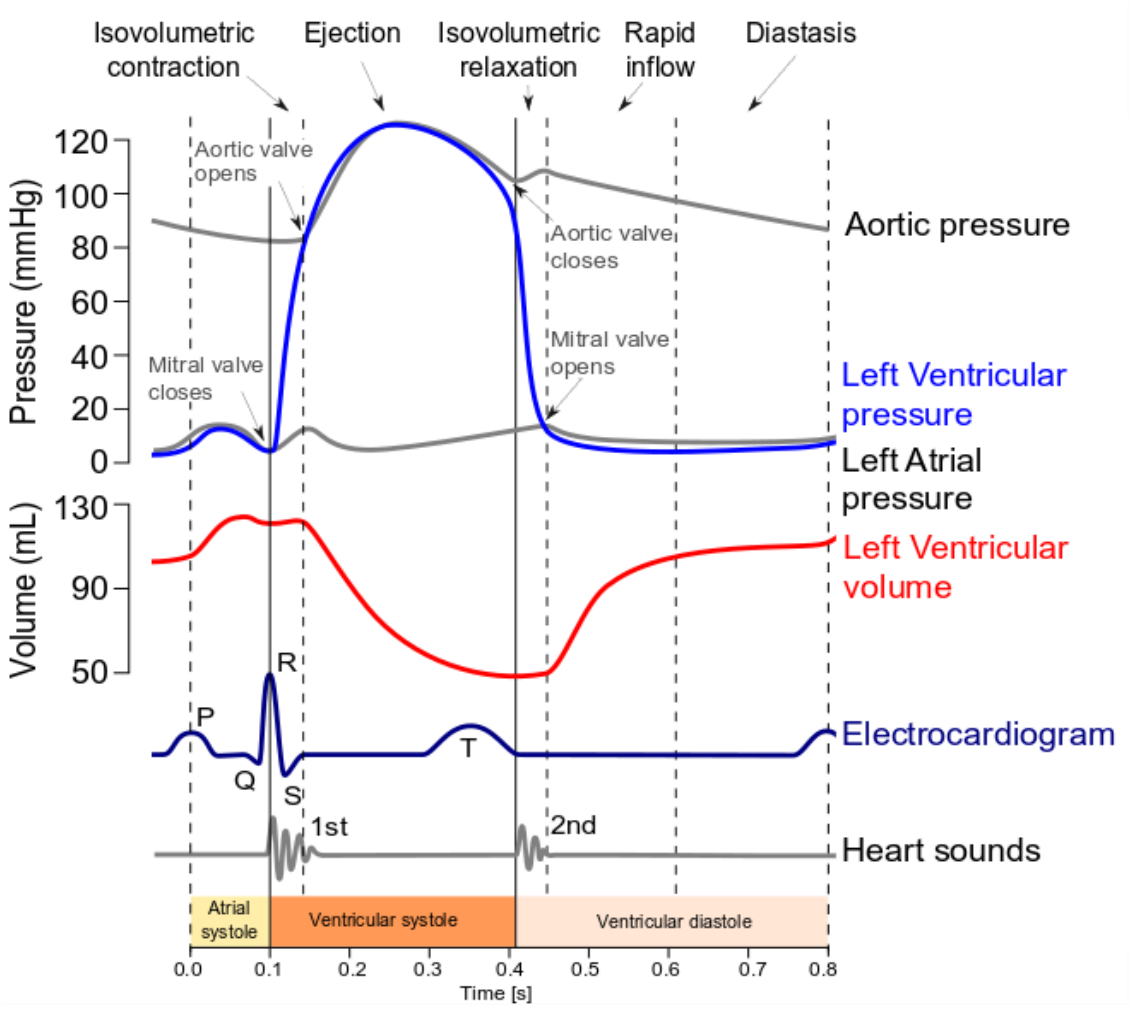


Figure 3.2: The Wiggers diagram shows the aortic pressure, the ventricular and the atrial pressure of the left heart, and the left ventricular volume compared to the electrocardiogram, heart sounds and different contraction states of the atrium and ventricle during one heart cycle. Figure adapted from Wikimedia Commons (CC-BY-3.0 license) and changed following Klabunde [67].

Once the pressure drops below the atrial pressure, the atrioventricular valves rapidly open and the passive refilling of the ventricles starts again. Most of the ventricular filling happens in this early phase (rapid inflow). During the second part of diastole, the blood inflow significantly slows down (diastasis), resulting in an almost constant volumetric and pressure equilibrium. The complete ventricular diastole lasts approximately 470 ms in a healthy heart at rest, but varies strongly in length depending on the heart rate [65].

3.1.3 Electrical Activity of the Heart and the Electrocardiogram

The electrical activity of the heart, the action potential in the neurons and the contraction of the cardiac muscle, is considerably different to those of neurons and skeleton muscle cells in other parts of the body. Whilst all heart cells can initiate spontaneous depolarisation, a network of specific cardiac pacemaker and conductive cells is spread around the heart to enable a well-defined and rhythmical muscle contraction. Gap junctions between cardiac contractile cells enable electrical coupling so that cell depolarisation can propagate along the heart muscle on a cell-by-cell basis. However, the atria are separated from the ventricle by fibrous tissue that permits direct conduction via cardiac muscle cells. Further, cardiac contractile cells have a slow influx of Ca^{2+} ions right after depolarisation. This inflow prolongs the repolarisation process and creates a plateau phase of the membrane potential, resulting in a refractory period during which another depolarisation is disabled. This effective refractory period is about 250 ms long and ensures a full and proper contraction of the heart muscle before another contraction can be triggered [66].

The electrical activity of the cardiac cells is measurable as an electrical potential on the body surface. An electrocardiogram (ECG) measures the summation of the electrical potentials from different angles using 3, 5 or 12 so-called leads, which measure the electrical potential difference between two electrodes. In cardiac MRI, an ECG configuration of three or four electrodes is most commonly used and is placed on the chest (left arm, left leg, right leg).

The normal electrical pattern of the heart is denoted as sinus rhythm, when a dense area of cardiac conductive cells, the Sino-Atrial (SA) node, initiates the heart contraction and functions as the pacemaker of the heart. The SA node is located in the superior and posterior wall of the right atrium. From the SA node, the first wave of electric potentials spreads into the left atria by the Bachman's bundle and through the right atria via the internodal paths to the atrioventricular (AV) node. The AV node is another dense area of cardiac conductive cells located next to the tricuspid valve within the interatrial septum (see Figure 3.3). The depolarisation of the atria is recorded as p-wave in the ECG and is usually 80 ms to 100 ms long [67]. Before the depolarisation propagates into the ventricles, the AV node induces a critical pause of about 100 ms to allow the atrium to contract completely. The AV node also bridges the isolated parts of the atria and the ventricle. It sends the electrical impulse via the bundle of His into the left and right bundles of the septum, through the Purkinje fibres, into the entire ventricle. The rapid depolarisation of the ventricles is known as QRS complex in the ECG, which normally lasts only about 60 to 100 ms [67]. The high R-peak in the ECG is often used to identify the heart rate and calculate the beat-to-beat interval (RR-interval). The following repolarisation of the ventricles is prominent

as T-wave in the ECG. The whole interval of ventricle depolarisation and repolarisation (QT interval) has a duration of 350 to 430 ms [67], depending on the heart rate (cQT, corrected QT-interval [63]). No further electrical activity is apparent during ventricular diastole and the refilling of the ventricles.

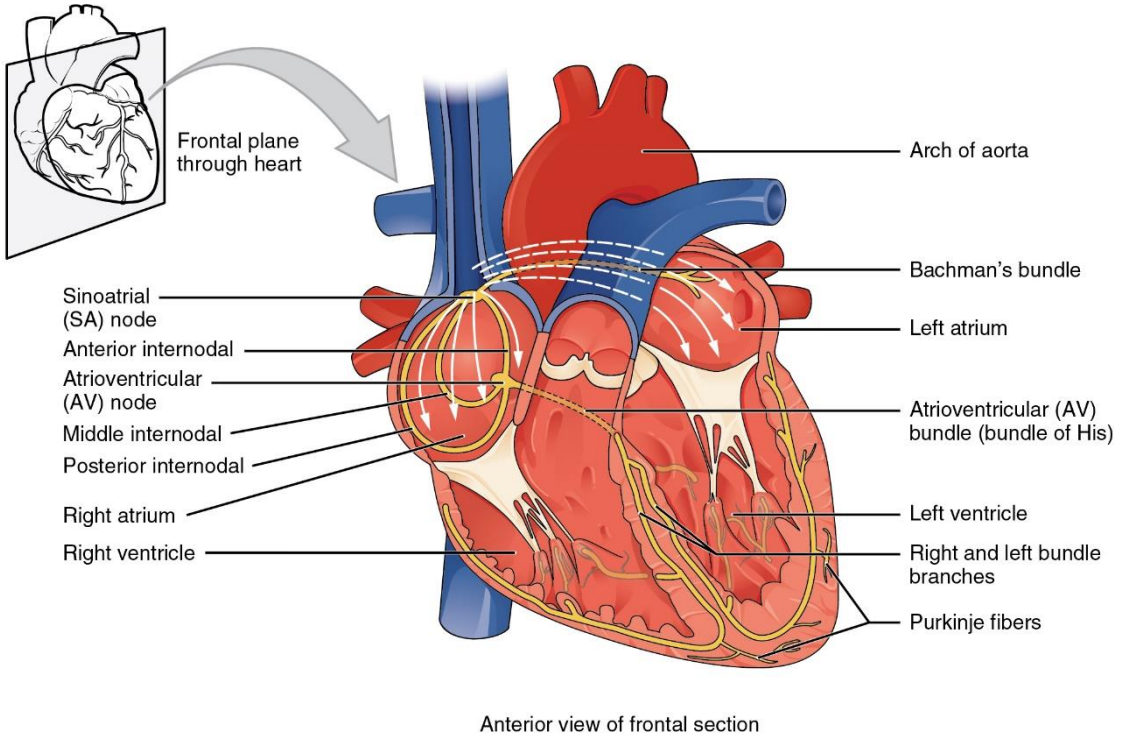


Figure 3.3: The electrical network of the human heart. Figure adapted from Betts et al. [192] using the CC-BY-4.0 license.

3.1.4 Arrhythmias of the Heart

Diseases of the heart and the circulatory system, so-called cardiovascular diseases, are the most common cause of death in the world. They account for 31.4% of total deaths in 2016 according to the World Health Organisation [68]. Several causes and risk factors lead to the development of cardiovascular diseases. The most prominent ones are: high blood pressure, smoking, high blood cholesterol levels, diabetes, physical inactivity, overweight and obesity, stress, family history, alcohol and drug abuse, and a poor diet [69].

Acknowledging that these risk factors lead to a wide range of different cardiovascular diseases, I focus on the most common conditions of irregular heartbeats (arrhythmia) in this thesis. Those conditions directly affect the motion and rhythm of the heart and consequently have the biggest influence on the timing and motion estimation in cardiac MR imaging. A full overview of cardiovascular disease can be found in the textbook by Mann et al. [70].

Cardiac arrhythmias can arise from disturbances in the electrical impulse formation, initiation (rate), or from an impeded electrical impulse conduction across the heart muscle. Different forms of structural heart diseases (cardiomyopathy) [71] or insufficient blood supply (ischemia) can cause abnormal structures in the heart muscles that lead to arrhythmias. A simple categorisation of different arrhythmia can be made by their place origin i.e. from the sinus node, the atria (supraventricular), the ventricles, or from the conduction between them (junctional). In the following paragraphs, a short overview and description of the most common arrhythmias is given.

Sinus Arrhythmia

Sinus arrhythmia is physiological and refers to the heart rate variation induced by respiration (respiratory induced sinus arrhythmia, RSA). It functions to promote a more effective gas-exchange [72]. The heart rate slows down during expiration and it increases during inspiration. The heart rate only varies around 5% during shallow breathing, but this variance can increase up to 30% during deeper breathing patterns [61].

Sinus Bradycardia and Tachycardia

Sinus bradycardia is a condition with regular electrical sinus activity but with a slow rate of fewer than 60 beats per minute (bpm) [61]. Sinus bradycardia does not always have negative effects as it often occurs in endurance athletes, who have a higher stroke volume per heartbeat, which typically results in a lower resting heart rate.

A regular but elevated heart rate above 100 bpm in adults is called sinus tachycardia.

Premature or ectopic heartbeats

Premature contractions, also known as extra systoles, can occur within the atria (premature atrial contraction) or within the ventricles (premature ventricular contraction). It originates from cardiac cells that spontaneously depolarise before the SA node can initiate a normal sinus beat. These ectopic beats interrupt the normal heart rhythm and result in an insufficient blood ejection. The following RR-interval is prolonged because the normal SA node excitation hits the myocardium in its refractory period (compensatory pause) [71].

Occasional ectopic heartbeats are benign and common with a prevalence of >6% of middle-aged adults [73].

Supraventricular Arrhythmia or Atrial Tachycardia

Supraventricular arrhythmia is a condition with in an abnormal fast heart rhythm, originating in the atria from re-entry or increased spontaneous depolarisation. In **atrial flutter,** a rhythmic and circular re-entry depolarisation in the right atrium increases the atrial contraction rate up to 200-350 bpm [61]. The refractory period of the AV node is too long to pass on such a high rate and it usually reduces the

ventricular contraction rate with a 2:1 or 3:1 ratio [61]. This results in a consistent but elevated heart rate.

An **atrial fibrillation (AF)** is characterised by an irregular re-entry depolarisation from many sides in the atria, leading to an uncoordinated, inconsistent and ineffective atrial contraction. Although the AV node limits the transmission, the ventricle contracts at a faster and more irregular rate, resulting in varying heart beat intervals from 0.35 s to 0.95 s and an average heart rate of 120-150 bpm [61]. AF is the most common pathological arrhythmia and associated with increased risk for stroke and heart failure [74]. Its unpredictable heart rate and length of RR-intervals is challenging for an effective cardiac MR imaging.

Ventricular Arrhythmia

A **ventricular (paroxysmal) tachycardia** originates from a single re-entry circular excitation within the ventricles, which leads to an abnormal but regular ventricular contraction at an elevated rate without synchronisation to the atria. **Ventricular paroxysmal tachycardia** can be brief and disappear suddenly, lasting for a few seconds, minutes, or even a few hours [61]. It is a serious condition as it can initiate **ventricular fibrillation.**

The mechanisms in **ventricular fibrillation** are similar to those in atrial fibrillation, where a single re-entry circular excitation evolves into multiple wavelets and re-entry points that cause uncoordinated contraction with no effective cardiac output.

Ventricular fibrillation leads to the loss of consciousness within a few seconds and death within minutes [1]. An electrical shock is sometimes used to treat

ventricular fibrillation by simultaneously setting all muscle cells into the refractory state.

3.2 Cardiovascular MRI

Cardiovascular magnetic resonance imaging (CMR) is a routinely used clinical tool for non-invasive diagnostic in cardiology. Freely selectable image orientation and good soft tissue contrast allows CMR to assess both myocardial and vessel anatomy, to measure blood flow, to evaluate cardiac function, to perform tissue characterisation, and to measure perfusion and wall motion. A complete overview of the general cardiovascular applications of MRI can be found in the textbooks [2], [3], with recent advances described in the review from Salerno et al. [4]. CMR at 7T has the potential to improve the spatial resolution and enable the visualisation of subtle structures in the heart utilising an increased SNR [13], [37], [75].

3.2.1 Image Positioning and Slice Orientations

CMR has developed standard image views of the heart that are oriented along the long and short axes of the heart. Figure 3.4 shows some of the most common image orientations that are used in this thesis. These include the 4-chamber view, the mid-ventricular short axis view, and the coronal view. The 4-chamber view is a horizontal plane, orientated along the long axis of the heart, which is tilted approximately 40° from the true coronal and horizontal (axial) plane [3]. It cuts the heart open from the apex through the mitral valve. The short axis view is perpendicular to both the 4-chamber view and the interventricular septum, and cuts through the ventricular base of the heart. Short axis views are often used

for cardiac ventricular function measurements, wall motion assessments and tissue perfusion evaluations.

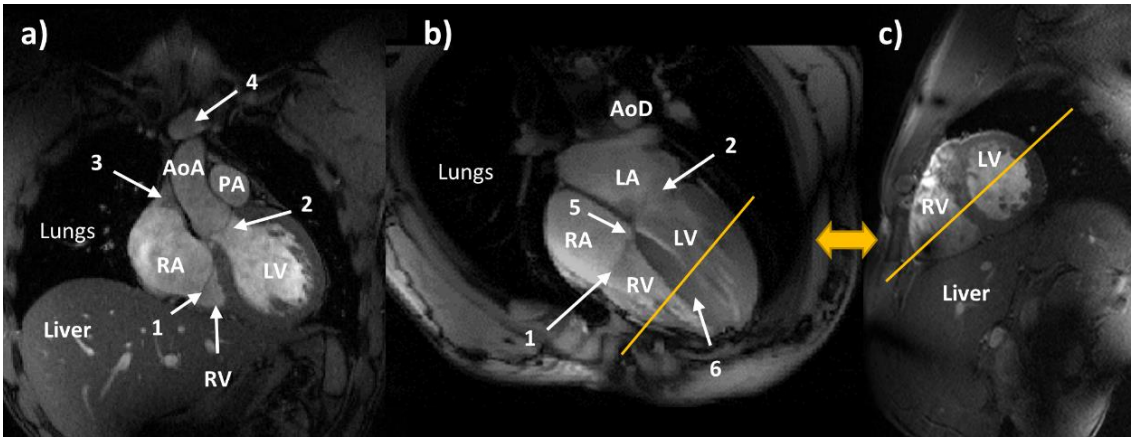


Figure 3.4: Gradient Recalled Echo (GRE) images from different views of the heart at 7T MRI. Images are obtained from different healthy subjects. A) Shows the coronal view of the heart. B) The 4-chamber view and C) the mid-ventricular short-axis view. The Left Ventricle (LV) and Right Ventricle (RV) are visible in all views. The Ascending Aorta (AoA) is separated from the left ventricle by the mitral valve (2) seen in the sagittal view (a) next to the pulmonary artery (PA) and left innominate vein (4). A good view on the right atrium (RA) and left atrium (LA) as well as the mitral valve (2) and tricuspid valve (1) is achieved in the four-chamber view (B), allowing for a good assessment of the ventricular (6) and atrioventricular septum (5).

3.2.2 Respiratory and Cardiac Motion in CMR

CMR imaging is strongly influenced by physiological motion. Normal respiration requires movements of the chest and the diaphragm, both of which are directly linked to the heart [76]. The displacement of the heart due to respiration is dominated by the movement of the diaphragm in the superior-inferior direction and is approximately linear [5], [77] with a translation factor of about 0.47 [78] to the apex movement, considering only rigid-motion. Subject specific variance was observed in the translation factor as well as an hysteresis effects during inspiration and expiration [79], with a non-linear translation during expiration. The

heart itself has a complex motion that includes a longitudinal shortening, a radial contraction, and a counter clockwise rotation of the apex [80].

3.3 MR Synchronisation

Currently, CMR is not a real-time imaging technique and too slow to capture a fast-moving organ like the heart. Without any acceleration, the respiratory-induced movements of the heart and the contractile motion during the cardiac cycle would cause strong blurring and image artefacts. Therefore, CMR examinations are often performed during breath holds to eliminate respiratory motion. An end-expiration position is used as it is more reproducible over consecutive measurements and the blood flow in the heart is less affected by the breath hold itself [81], [82]. Healthy volunteers are comfortable to hold their breath for about 20-30 seconds, whereas many patients and children are only capable of less.

Synchronisation with the heart cycle is often accomplished with ECG gating or other cardiac motion estimation techniques, acquiring *k*-space data either during specific phases (e.g. mid-diastole, when the heart is at rest) or continuously, where data is resorted according to the motion state of the heart to reconstruct short movies of a synthesised single heart beat (cine).

3.3.1 Cine Imaging

Cine imaging allows for an evaluation and visualisation of the contractile function of the heart by reconstructing images of different phases of the cardiac cycle that are combined to movies of the beating heart. It is has been used extensively in combination with segmented *k*-space data acquisitions to acquire all data

needed within a single breath hold [83]–[85]. Therefore, the required *k*-space is divided into segments, each of which is acquired during one heart interval (RR-interval for ECG based cine), and contains a group of *k*-space lines that are measured. Usually, about 7-13 *k*-space lines are measured within one segment, which defines the effective temporal resolution of the cine and the duration of one cardiac phase. The total number of resolved cardiac phases or “frames” depends on the temporal resolution and the heart rate, i.e. length of the RR-interval. Typically, 20-35 cardiac phases can be reconstructed with a temporal resolution of 30-50 ms per cine frame using a fast gradient-recalled echo sequence with relatively short TR [2].

When all *k*-space segments are measured, the data from different heart intervals are reordered and combined to fill the *k*-space for each cardiac phase and to reconstruct a synthesised video of a single, averaged cardiac cycle (see Figure 3.5). Assuming identical heartbeats during the measurements, a regular and consistent rate and motion of the heart is necessary for high-quality cine images. The temporal resolution of the cine is a trade-off between the spatial resolution of the images and the total acquisition time. For a given number of phase encoding lines (N_{PE}), a higher temporal resolution would require more segments, and thus more consecutive heartbeats that would prolong the overall acquisition time. The minimum temporal resolution is equal to the repetition time (TR) but would require N_{PE} consecutive heartbeats to acquire the entire data set. Commonly, the patients’ capabilities to hold their breath and their heart rate

restrict the length of the data measurements and thus the temporal and spatial resolution of the cine.

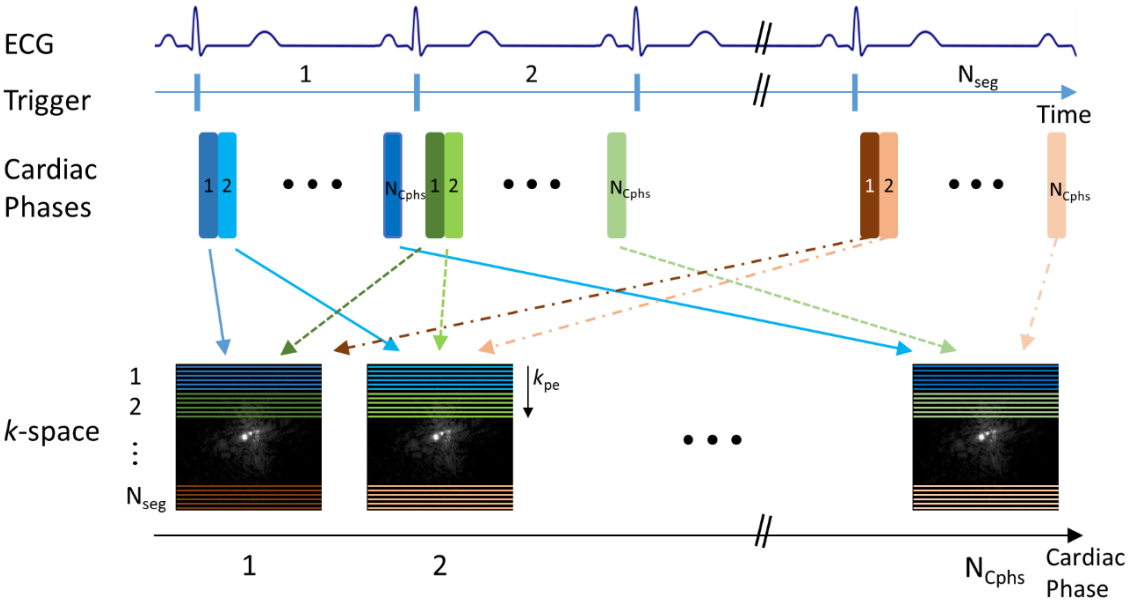


Figure 3.5: Cardiac cine imaging with segmented *k*-space data acquisition and ECG triggering. Each heartbeat interval is divided into multiple phases. During each cardiac phase, multiple *k*-space lines are acquired, defining one segment of *k*-space. The entire *k*-space for each cardiac phase is filled with measurements/segments from consecutive heartbeats, resulting in one image frame for the cine of the heart cycle.

3.3.2 Prospective Triggering and Retrospective Gating

The synchronisation of the MR data acquisition to the heart and to respiratory-induced motion can be completed prospectively (triggering or gating) or retrospectively (gating).

Data measurements with **prospective triggering or gating** start at a pre-defined time (operator-selected delay) after a physiological, chosen trigger event, positioning the data acquisition into a pre-defined acquisition window that covers certain cardiac phases (i.e. mid-diastole for static imaging) or a certain state of inspiration.

For cardiac gating, this window is usually shorter than the average cardiac cycle to allow for normal variations in the cardiac cycle length. It covers about 85-90% of the average cardiac cycle length, leaving 10-15% for a trigger window, during which the MRI is waiting for the next cardiac trigger event (see Figure 3.6).

Prospective, respiratory-gated acquisitions often use a simple accept/reject algorithm, starting the image acquisition once a certain respiratory motion state is reached (e.g. end-expiration).

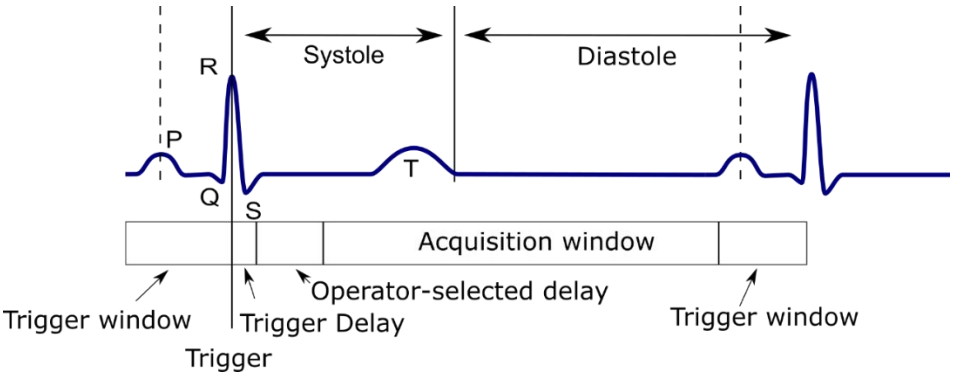


Figure 3.6: Prospective cardiac triggering/gating using a pre-defined delay and acquisition window.

Retrospective gating, however**,** continuously acquires data and runs independently to the monitoring signal. After the measurements are completed, *k*-space data is retrospectively reordered, grouped, excluded or shared using information form the monitoring signals for image reconstruction.

One of the main advantages of retrospective gating is the full coverage of the cardiac and respiratory cycle, whereas prospective gating can miss out parts of end-diastole and atrial systole (when ECG is used for cardiac gating/triggering) due to variations in the length of the heart cycle. Measuring the correct end-diastolic state is crucial for a correct estimation of the filling rate, stroke volumes and the ejection fraction of the heart. Further, prospective cardiac gating is more

sensitive to irregular heartbeats or arrhythmias. Cardiac events that do not occur within the pre-defined trigger window will be disregarded and re-acquired in the next cardiac interval, prolonging the image acquisition.

3.3.3 Electrocardiogram Trigger: The Magneto-Hydrodynamic Effect

As MR data is acquired over multiple consecutive heartbeats, the variability and stability of the cardiac gating device is important for the performance of the MR scan and the resulting image quality. In clinical practice, the R-wave in an electrocardiogram is most commonly used to trigger CMR acquisitions [86]. Modern QRS detection algorithms are based on vectorcardiograms, 3D representations of the cardiac electrical activity that can be derived from a normal ECG. These have improved the reliability and robustness of the ECG gating signals [12], [87], [88]. However, several different factors can corrupt and decrease the quality of the ECG signal and can lead to insufficient cardiac gating/triggering. These include poor skin electrical contact of the electrode, bad placement of the surface electrodes, interference with electromagnetic fields, and the **magneto-hydrodynamic (MHD)** effect [11], [89], [90].

The magneto-hydrodynamic effect originates from the motion of electrically conductive fluids (e.g. blood) within the external, static magnetic field of the MRI scanner. The induced force (Lorenz Force) on the charged particles is proportional to the magnitude and orientation of the blood flow to the static magnetic field:

$$\vec{F} \propto (\vec{v} \times \vec{B}_0) \tag{3.1}$$

The resulting movement of charges produces an electrical potential within the vessels that leads to an electrical surface potential in the body. The corrupting MHD effects mainly originate from the aortic arch, where the blood flow is perpendicular to the static magnetic field and the blood flow velocity is the highest [91]. Consequently, the T-wave in the ECG gets distorted and the measured electrical potentials can be higher than those arising from the QRS complex [92]. The MHD effect is proportional to the field strength and present for all MRI field strengths. It has been reported that it strongly interferes with the electrical potentials measured by the ECG in higher magnetic fields (≥3T) [13], [89], [93] (see Figure 3.7).

Sometimes R-wave detection algorithms falsely interpret the MDH effect as a new cardiac cycle, making ECG gating less reliable [94]. A re-adjustment of the electrodes may become necessary until a sufficient ECG signal can be measured, which increases patient setup time. Missed or false trigger during the examination can increase scan time or significantly degrade image quality in CMR.

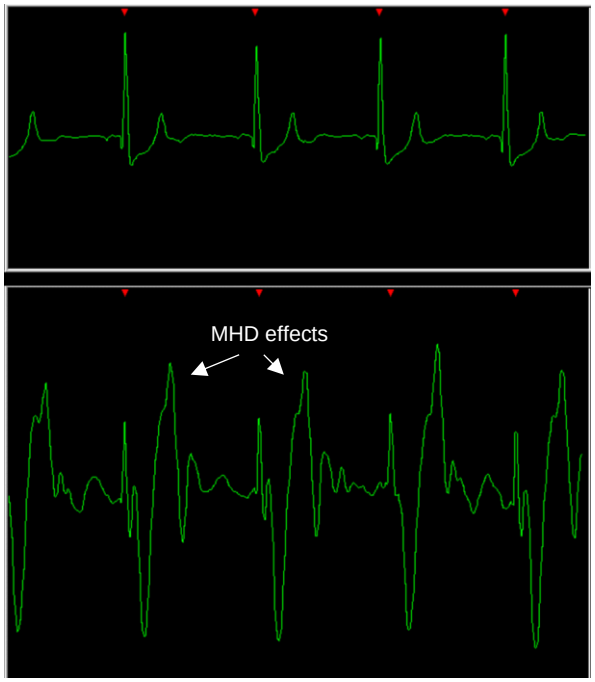


Figure 3.7: The magneto-hydrodynamic (MHD) effects on the ECG signal are shown for a healthy volunteer with a mean heart rate of 54bpm A) outside and B) inside the 7T MR scanner. Red triangles indicate the R-wave.

3.4 Dealing with Motion: Existing Techniques

The limitations of ECG-based cardiac gating in UHF MRI and the time restriction of breath holds have led to the development of several strategies for a more reliable motion estimation and an improved cardiac gating. Some of these methods simultaneously estimate respiratory motion and cardiac motion, allowing for free-breathing CMR acquisition. In general, the existing motion estimation methods for CMR can be categorised into four different approaches;

1) Extraction of motion information from raw MR-data (*k*-space and FID signal)

2) Rapid image registration and tracking,

3) External devices,

4) Coil-based or electrical properties-based motion estimation.

3.4.1 Raw MR-Data based Motion Estimation

The principles of raw MR-data motion estimation are based on the Fourier-pair relationship between image and frequency domain, where a displacement or rotation in image space results in a phase shift and magnitude change in the frequency domain (*k*-space). Therefore, repeated measurements of specific *k*-space regions enable the extraction of motion information from the imaged object to generate cardiac and/or respiratory surrogate signals. Most of the information needed for a good motion estimation is stored in the centre region of *k*-space.

The measured, raw MR-data signals are often used to generate 1-D image projections (1-D Fourier transform), which include the entire image information and are then compared to a reference by least squares fitting [95], [96], (cross- or auto-) correlation of the complex data [97], or with simple image edge detection [98]. These so called “wire-less” gating techniques measure the raw-MR data with a monitoring echo readout that is interleaved with the image data acquisition [8], [97]–[99]. Only minimal or no phase encoding is applied, measuring the centre of *k*-space.

More recently developed methods measure a refocused, Free Induction Decay (FID) signal, which is measured either during the gradient re-winders in balanced SSFP-sequences [100] or immediately after slice refocusing [96], [101], [102]. Refocused FID signals do not need a separate monitoring RF pulse excitation and thus reduce the temporal burden of those techniques and enable a faster motion monitoring. The robustness and the sensitivity to motion of the FID signal readouts can be further increased by modified phase-encoding gradients [96], [103]. These small adaptions allow for the sampling of the centre of *k*-space for

every excitation in a Cartesian *k*-space sampling trajectory with only minor time penalties of about 0.5-2 ms for each TR.

Monitoring echoes can also be generated any time during the sequence using additional small, interleaved navigator RF pulses [104]. Localised, 2D RF excitations and navigator echoes (NAV, pencil beam navigator) have been used extensively to specifically target motion in certain body regions, e.g. the diaphragm-lung interface for respiratory motion estimation [6], [95], [98], [105]–[107]. However, these monitoring echoes can lead to saturation artefacts in region of interest.

Non-Cartesian *k*-space sampling trajectories can measure the *k*-space centre in each read-out and are often denoted as “self-gating”, e.g. radial [7], [108]–[111] or spiral and spiral-like *k*-space trajectories [112]–[114]. An extension to multi-coil data allows for more localised and more accurate motion estimation and motion deformation models [115]–[117].

While raw MR-data-based motion estimation techniques have been studied extensively, all those methods are inherently linked to the *k*-space trajectory and read-out or require modifications to the original sequence. This limits their general applicability.

3.4.2 Image-based Motion Methods

Image-based motion estimation methods usually acquire an additional low-resolution navigator image (iNAV) [118]–[121] or compute virtual navigator images (vNAV) [122], where a subset of the data, which has already been acquired, is used for preliminary image reconstruction. Motion is estimated using image registration [122]–[124], correlation coefficients [125], [126], or template

matching [121] on a selected region-of-interest in the respective images. Image-based motion estimation methods enable direct and multidimensional motion estimation derived directly from the heart, rather than from surrogate signals or diaphragm positions. Image-based motion estimations are limited to a lower temporal and spatial resolution of the motion signals and can prolong continuous image acquisitions.

3.4.3 External Devices and Sensors

External devices that are independent to the electrical activity of the heart are used to measure the heart cycle and create ECG-like surrogate signals. Some are based on peripheral triggering, including pulse oximetry [127], finger plethysmography [128] or Doppler ultrasound [129], measuring the blood volume changes in the finger, arm or neck with each heartbeat. The resulting signals have a strong latency compared to the ECG, placing a smooth peak at the start of the diastole from which it is more difficult to trigger accurately. The latency of the signal complicates the timing for systolic contraction and does not allow triggering the beginning of the cardiac cycle.

Other external devices are based on the measurement of heart tones (phonocardiograms) [130] during the isovolumetric contraction of the heart. The derived trigger signals have a short latency and small trigger timing variation compared to the ECG but require specialised hardware and an expert setup.

Respiratory motion estimation with external devices is usually carried out using respiratory bellows [9], [10]. A simple strap is placed around the chest to measure the movement during inspiration and expiration. Careful, patient-specific adjustments are necessary for chest and diaphragmatic dominated respiratory

motion. Correct time synchronisation to the image sequence is crucial for all external devices and requires additional setup.

3.4.4 RF Coil and Electromagnetic Properties-based Motion Estimation

A different approach to assess motion in CMR is based on RF coils properties. The load impedance of the RF coils is a function of the coil profile and the conductivity of the tissue (compare section 2.4.4). Changes in the tissue distribution due to respiratory motion, heart motion and blood flow result in changes of the load and the inductively coupled resistance of the coil. This effect has been observed in receive coil arrays and has been used to estimate respiratory motion by monitoring the receive coil noise characteristics [58], [131]. The attenuation of a reference RF transmitter signal (called a “pilot tone navigator”) that is picked up by local receive coils, has been used for respiratory motion tracking and cardiac motion estimation [132]–[135].

For a transmit RF coil, this effect was used to show respiratory and cardiac influence early on by Buikman et al. [136]. For transmit arrays or parallel transmit (pTx), pickup coils that measure the currents in the coil elements can be used to monitor respiratory motion [137], [138].

These methods are limited by measuring only relative motion changes with no clear directivity but have the advantage of being independent to the MR excitation process, the MRI data or its *k*-space sampling trajectory. They are synchronised to the image sequence by the use of MR-systems hardware [58], [131], [136]–[138].

CHAPTER 4

CARDIAC MOTION ESTIMATION USING RF SCATTERING OF A PTX COIL

As discussed in chapter 3, the current gold-standard cardiac gating method, the electrocardiogram (ECG), is strongly affected by magnetic fields through magnetohydrodynamic (MHD) effects [139]. While ECG gating is still possible, ECG electrode re-positioning is frequently required at 7T MRI [13] and increases subject setup time. Decreased accuracy can cause missed or false trigger results that can increase scan time or significantly degrade image quality.

In this chapter, I introduce a new method to estimate a cardiac motion signal based on the RF scattering properties of an 8-channel parallel transmit (pTx) RF coil array. The quality of the estimated cardiac signal is compared using the scattering matrix or scattering coefficients and the influence of B_1^+ shim is evaluated on the latter. Different potential gating features are presented and the cardiac gating accuracy and sensitivity is compared to the R-peak detection of the ECG.

The work of this chapter has been published in the journal “Magnetic Resonance in Medicine” in 2018 [140].

4.1 Introduction

The electrocardiogram is the current gold-standard method for cardiac gating but is strongly affected by magnetohydrodynamic effects [91]–[93]. Many different gating methods, which are independent to the electrical activity of the heart, have been developed to improve cardiac gating at high field ($B_0 \geq 3$ T) MRI. These methods derive cardiac signals directly from *k*-space, use low-resolution images, external monitoring devices and/or sensors, or utilize the electromagnetic properties of the RF coils (see in more detail in section 3.4). However, there remains a need for a cardiac gating method that is widely applicable, is independent to the *k*-space trajectory, does not require additional monitoring hardware, and no expert setup.

Buikman et al. [136] have showed that the RF coil itself can be used to monitor motion as the quality factor of the coil, and therefore the fractional reflected power, changes as a response to motion.

The work in this chapter follows this approach and evaluates the sensitivity of the scattering matrix and the scattering coefficients of an 8-channel pTx coil for cardiac motion. The scattering matrix is measured using a dedicated monitoring pulse sequence and the directional couplers of the pTx safety system are utilised to measure the transmitted and reflected RF waveforms.

4.2 Theory

The theoretical basis of this technique was outlined in more detail in chapter 2. In brief, the pTx coil, which is electrically loaded by the human body, can be described as an *N*-port electrical network, where *N* is the number of transmit channels of the pTx array. In the absence of measurement error, the N×N scattering matrix $\mathbf{S}$ defines the fractional, returned voltage $V_{i,j,\mathrm{ret}}$ on channel *i*, which originates from the forward voltage ($V_{j,\mathrm{fwd}}$) on channel *j*:

$$V_{i,j,\mathrm{ret}} = S_{i,j}\, V_{j,\mathrm{fwd}} \tag{4.1}$$

The returned voltage arises because of the mutual inductance between RF coil elements and the impedance mismatch between the characteristic impedance of the amplifier and the apparent impedance at the input ports. These, in turn, are sensitive to the complex conductivity of the tissue within the field-of-view of each coil element (see equation 2.18). In the case of cardiac motion, the changing distribution of tissue and volume of highly conductive blood in the heart in different phases of the cardiac cycle leads to a change in the apparent impedance. The time-dependent scattering matrix $\boldsymbol{S}(t)$ is therefore modelled with two terms (here neglecting respiratory motion): $\mathbf{S_0}$ represents the temporally invariant coil properties and static tissue, and $\Delta\mathbf{S}_{\mathrm{cardiac}}(\boldsymbol{t})$ represents the change resulting from cardiac motion:

$$\boldsymbol{S}(t) = \boldsymbol{S_0} + \Delta\boldsymbol{S}_{\mathrm{cardiac}}(t) \tag{4.2}$$

4.3 Materials and Methods

4.3.1 In-vivo Experiments

All experiments were carried out using a 7T MRI Scanner (VB17, Step 2.3, Siemens 7.0 T Magnetom, Erlangen, Germany) and an 8 channel pTx system with a custom build transverse electromagnetic (TEM), cardiac transmit/receive array [141] with four elements placed anterior and four elements placed posterior on the chest. Eight healthy volunteers (male, age= 24-39 years) participated in this study. Directional couplers (DICOs) are built into each of the RF transmission lines as part of the pTx safety system to monitor the specific absorption rate (SAR). These DICOs split off a small proportion of the complex RF signal and were used to quantify the forward ($\vec{V}_{\mathrm{fwd}}(t)$) and return ($\vec{V}_{\mathrm{ret}}(t)$) RF waveforms. These measurements are digitised using the standard MR receiver at a sampling rate of 1 MHz after demodulation of the system frequency. ECG trigger times were recorded from the MR scanner using a 3-lead commercial vector ECG module (Siemens, Erlangen, Germany).

4.3.2 Scattering Matrix Measurements $\boldsymbol{S}$

Frequency-multiplexed pTx Gaussian profile RF pulses (frequency range 0 to 14 kHz in steps of 2 kHz per channel, amplitude 11.1 V, pulse duration 5 ms, TR 10 ms) were used to obtain distinct waveforms of $\vec{V}_{\mathrm{fwd}}(t)$ for each transmit channel [57]. Multiple data sets (2 to 4 per participant) of the forward voltages $\vec{V}_{\mathrm{fwd}}(t)$ and returned voltages $\vec{V}_{\mathrm{ret}}(t)$ were recorded. Each subject was instructed to hold his or her breath for 15 seconds and then breath freely for a remaining 25 seconds.

A fast Fourier transformation (FFT) was used to identify each $V_{j,\mathrm{fwd}}(t)$ and $V_{i,j,\mathrm{ret}}(t)$ and thus to calculate $\boldsymbol{S}(t)$ as in equation 4.1. An example measurement of the S-matrix $\boldsymbol{S}(t)$ is shown in Figure 4.1.

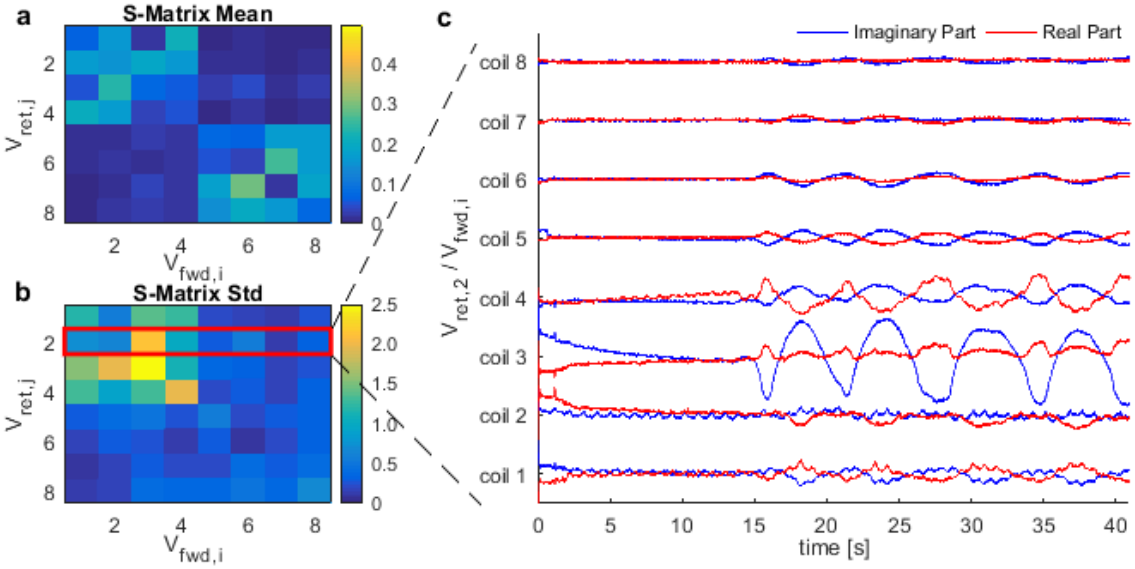


Figure 4.1: Example measurement of the S-matrix. The mean and standard deviation of scattering matrix $\mathbf{S}(\mathrm{t})$ are shown in a) and b) respectively. High scattering can be observed between adjoining coils 1-4 and 5-8. The highest standard deviation is observed in coils 1-4, which were placed anterior on the subject's chest and those sensitivity profiles have the biggest coverage of respiratory and cardiac induced tissue changes. c) Real and imaginary parts of the complex S-matrix measurements $\mathbf{S}(\mathrm{t})$ on coil 2 are shown. Respiratory-induced S-matrix variations can be observed for the period of free breathing t>15s.

4.3.3 Scattering Coefficients $\vec{\boldsymbol{\Gamma}}$

Typical MRI cine acquisitions at a field strength of 7 T use a static B_1^+ shim with all channels transmitting the same RF pulse simultaneously. $\boldsymbol{S}(t)$ cannot be determined during this kind of pulse sequence, as the source of the returned voltages cannot be identified without changing the RF pulse or the sequence. However, $\vec{V}_{\mathrm{ret}}(t)$ remains a function of $\Delta\boldsymbol{S}_{\mathrm{cardiac}}(t)$ and the DICOs measure the

forward voltages $\vec{V}_{\mathrm{fwd}}(t)$, which are a function of the transmit voltage ($\vec{V}_{\mathrm{tx}}(t)$) and any noise or drift in the amplifiers ($\vec{e}(t)$), as follows:

$$\vec{V}_{\mathrm{ret}}(t) = \left(S_0 + \Delta S_{\mathrm{cardiac}}(t)\right)\left[\vec{V}_{\mathrm{tx}}(t) + \vec{e}(t)\right] \tag{4.3}$$

where $\vec{V}_{\mathrm{fwd}}(t) = \vec{V}_{\mathrm{tx}}(t) + \vec{e}(t)$. The static scattering (S_0) can be determined before the scan by either a direct measurement of S_0, using the method in the previous section, or by averaging the time series of $S(t)$. Then, S_0 can be used to normalise $\vec{V}_{\mathrm{ret}}(t)$ and correct amplifier drifts with an element wise vector division to form a vector of normalised scattering coefficients $\vec{\Gamma}(t)$ that are sensitive to motion [57]:

$$\vec{\Gamma}(t) = \frac{\vec{V}_{\mathrm{ret}}(t)}{S_0\vec{V}_{\mathrm{fwd}}(t)} = 1 + \frac{\Delta S_{\mathrm{cardiac}}(t)\vec{V}_{\mathrm{fwd}}(t)}{S_0\vec{V}_{\mathrm{fwd}}(t)} \tag{4.4}$$

4.3.4 B_1^+ Shim and Scattering Coefficients $\vec{\boldsymbol{\Gamma}}^{\boldsymbol{A}}$

To facilitate a direct comparison between the cardiac signal derived from $\boldsymbol{S}(t)$ and that from $\vec{\Gamma}(t)$, normalised scattering coefficients $\vec{\Gamma}^A(t)$ were simulated from the above measurements of $\boldsymbol{S}(t)$ during breath hold, which additionally enabled evaluation of the effects of B_1^+ shimming. To evaluate the effects of B_1^+ shimming, 1000 vectors ($\vec{A}$) with components of unit magnitude and random uniformly distributed phases were created for each data set $\boldsymbol{S}(t)$. These vectors ($\vec{A}$) were retrospectively applied to each of the frequency de-multiplexed $\vec{V}_{fwd}(t)$ (those that have been used to determine $\boldsymbol{S}(t)$) with an element wise multiplication to give B_1^+ shim dependent forwarded voltages $\vec{V}_{fwd}^{A}(t)$. The corresponding

returned voltages were calculated as $\vec{V}^A_{ret}(t) = \boldsymbol{S}(t)\,\vec{V}^A_{fwd}(t)$. For each B_1^+ shim and $\boldsymbol{S}(t)$ data set the scattering coefficients $\vec{\Gamma}^A(t)$ were determined using equation 4.4, where $\boldsymbol{S}_0$ was taken as the average of $\boldsymbol{S}(t)$.

4.3.5 Scattering Coefficients $\vec{\boldsymbol{\Gamma}}$ Measurement in Retrospective Cine

A 2D, retrospectively gated, cine Gradient Recalled Echo (GRE) sequence was acquired in five of the participants. The parameters were; voxel size= 1.3×1.3×6 mm, TR/TE= 2.9/2 ms, flip angle≈ 10°, generalized auto-calibrating partially parallel acquisitions (GRAPPA) factor of two with 24 reference lines, a total scan time of approximately 18 s. $\vec{\Gamma}(t)$ was calculated for each RF pulse during the acquisition without the use of any additional monitoring pulses or pulse sequence modifications. $\boldsymbol{S}_0$ was acquired prior to the imaging scan by averaging the time series $\boldsymbol{S}(t)$, which was measured as described above. The cardiac signal was calculated from $\vec{\Gamma}(t)$ and peak detection was carried out as described below. The *k*-space data was binned by either using the scattering or the R-peak detection of the ECG. All images were reconstructed in MatLab (MathWorks, Natick, MA, USA), with the PULSAR MatLab toolbox V1.1 [142].

4.3.6 Cardiac Signal Extraction Algorithm

All signal analysis was conducted retrospectively in MatLab (MathWorks). To extract the cardiac signal, the data was separated into real and imaginary components, giving 128 ($8 \times 8 \times 2$, $\boldsymbol{S}(t)$) or 16 (8×2, $\vec{\Gamma}(t)$) data points for each measurement forming a measurement vector $\vec{x}(t)$. The measurements were analysed automatically according to the following steps:

1. Demeaning and de-trending to remove any drifts using quadratic polynomials fitted and subtracted from the measurements.
2. Low pass filtering using a digital Butterworth filter object [143] to eliminate spikes and noise (infinite impulse response design with an order of 17, passband frequency 7.5 Hz, stopband frequency 15 Hz). The filter was applied in a forward and backward fashion to avoid time shifts in the filtered signal.
3. Principal component analysis and independent component analysis (ICA) using Hyvärinen's fixed-point algorithm [144] built into the FastICA (Version 2.5, [145]) software package for MatLab (MathWorks). The dimensionality reduction was based on the eigenvalues of the covariance matrix and values greater than an absolute threshold of $\varepsilon = 0.75\times10^{-7}$ (default $\varepsilon = 1\times10^{-7}$) were kept and the dimension was reduced to the number of kept eigenvalues.
4. A Welch power spectral density estimation was used to identify the correct cardiac component automatically by finding the maximum power within the cardiac frequency range of 0.6 Hz to 2.4 Hz of all estimated components. This information was used to determine the cardiac de-mixing vector and to extract the cardiac signal $c(t)$ from the measurements $\vec{x}(t)$.
5. The polarity of the cardiac signal was standardised to enable automated signal analysis. This was determined using a peak detection on the absolute signal, followed by a k-means clustering with the corresponding peak height.

4.3.7 Gating Features from Cardiac Signal

The cardiac signal $c(t)$ was used to establish four further traces to facilitate peak detection and to assess different gating features. Two traces were derived from a multilevel, discrete wavelet transform with a maximal overlap [146] and a symlet wavelet of order 5. For the first trace, which is denoted as $c_{w6}(t)$, only the wavelet coefficients that correspond to the expected frequency range of the heart rate were kept and an inverse wavelet transform was performed (level=6), which ensured a single peak per cardiac cycle. The second trace, $c_{w4}(t)$ was established with an inverse wavelet transform with a higher frequency window (level=4) which resulted in two peaks per cardiac cycle.

The third and fourth traces were created by applying a Savitzky-Golay filter [147] on the cardiac signal $c(t)$, followed by a calculation of the first and second order discrete temporal derivatives and were denoted as $c'(t)$ and $c''(t)$, respectively. For all traces, the local maxima were identified using MatLab and the resulting peaks were separated, when necessary, by using k-means clustering on the cardiac signal and the corresponding traces, resulting in five different gating features.

In addition to the main peak identification of the first trace, which occurs near to the end-systole of the cardiac cycle, the other four gating features correlate with different phases and events in the cardiac cycle (see Figure 4.2 and Figure 4.3). Those are:

- Atrial contraction, identified as a second, minor peak in $c_{w4}(t)$
- Atrial contraction, identified as the small, negative peak in $c'^{(t)}$

- Early systole, close to the ECG R-wave and start of ventricular contraction, identified as the peak in $c''(t)$ and
- Start of the diastasis: when the heart is almost at rest and where least heart motion occurs, identified as peak in $c''^{(t)}$ and minima of $c'^{(t)}$.

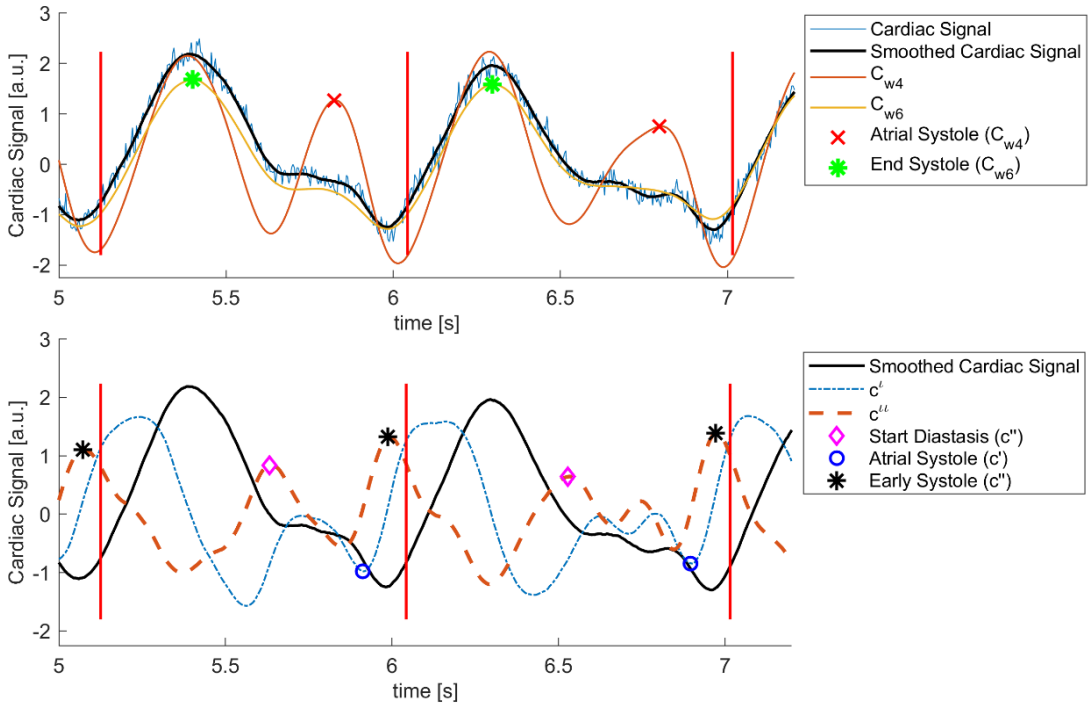


Figure 4.2: Different gating features and underlying traces. A) The cardiac signal with the two traces obtained using a multilevel, discrete wavelet transform. B) The third and fourth trace derived from the first and second order discrete temporal derivatives. ECG trigger are shown with vertical, red lines.

These different gating features were assessed in a retrospective signal analysis when using $\boldsymbol{S}(t)$. In the cardiac signal, based on measurements of $\vec{\Gamma}(t)$, only the main peak of the first trace was apparent and was the only gating feature evaluated.

The noise in the cardiac signal of each data set was calculated by subtracting the filtered (Savitzky-Golay filter [147]) cardiac signal from the unfiltered cardiac signal and taking this standard deviation (SD) as the magnitude of noise. The

mean peak amplitude of the cardiac signal, divided by this noise, is the signal-to-noise-ratio (SNR) of the cardiac signal.

4.3.8 Evaluation of Gating Accuracy

Statistical evaluation was carried out for breath hold and free breathing separately. Cardiac cycles with ectopic beats or missed ECG triggers were manually excluded. The delays between the ECG trigger (R_n) and the detection time of the respective feature (F_n), detected in cardiac cycle *n*, were averaged to determine a mean trigger delay (*MTD*):

$$MTD = \frac{1}{N}\sum_{n=1}^{N}(F_n - R_n) \tag{4.5}$$

where N is the total number of cardiac cycles. Herein, a negative *MTD* corresponds to a peak detection before the ECG trigger event. The standard deviation s of the time difference was also calculated:

$$s = \sqrt{\frac{1}{N-1}\sum_{n=1}^{N}(\,(F_{\mathrm{n}} - R_n) - MTD)^2} \tag{4.6}$$

The peak detection performance was evaluated using the sensitivity (*Se*) and the positive predictive value (*PPV*), which were calculated with equation 4.7 and equation 4.8, respectively. Each of the gating features was assumed to occur exactly one time during a normal heart cycle and were manually assessed by overlaying the ECG trigger events and the extracted cardiac signal and counting the number of detected features. Whereas true positives (*TP*) were correctly identified events, false negatives (*FN*) were missed events and additional peaks (including in the ECG) were counted as a false positive (*FP*).

$$Se = \frac{TP}{TP + FN} \tag{4.7}$$

$$PPV = \frac{TP}{TP + FP} \tag{4.8}$$

4.4 Results

The identification of the cardiac component failed on one data set, which has been excluded and replaced with data from a second scan on the same subject, where it succeeded. This failure was due to a broken RF coil element.

The cardiac signal was identified automatically in all remaining data sets when using $\boldsymbol{S}(t)$ and $\vec{\Gamma}(t)$. Figure 4.3 shows an example cardiac signal extracted using $\boldsymbol{S}(t)$ and $\vec{\Gamma}^{A}(t)$ as simulated with an appropriate B_1^+ shim from the same data set, with one large peak per heart cycle that occurs close to the time of end-systole. The SNR of the cardiac signal had a mean value of 33.1 (ranging from 11.4 to 45.7) using $\boldsymbol{S}(t)$ and a mean value of 5.7 (ranging from 2.4 to 10.2) using $\vec{\Gamma}(t)$, as measured during cine acquisition.

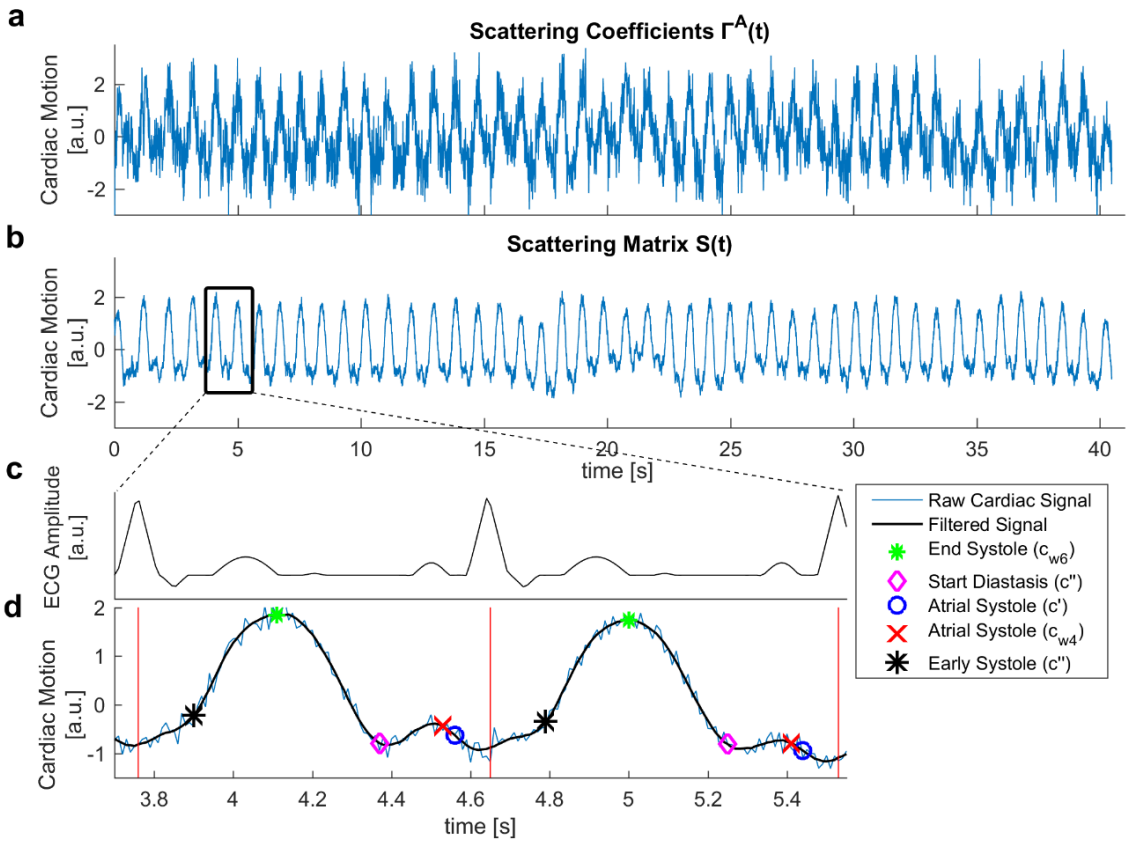


Figure 4.3: The extracted cardiac signal is shown using A) the scattering coefficients $\vec{\Gamma}(t)$ and B) the scattering matrix $\boldsymbol{S}(t)$. (C-D) Two selected cardiac cycles are shown and compared with an artificial ECG trace. The different features are displayed on the cardiac signal extracted using $\boldsymbol{S}(t)$. The end-systole is targeted with the main peak (green star) of c_{w6} .The feature that coincides with the start of the diastasis is indicated by a magenta diamond (c''), the ones for atrial contraction with blue circles and red crosses (targeted by using c' and c_{w4} respectively) and the feature for the early systole (c'') is indicated by black stars. Vertical red lines are ECG-trigger time points (R-peak).

Figure 4.4 shows the effect of changing B_1^+ shim on the accuracy of the detection of end-systole in the simulated scattering coefficients $\vec{\Gamma}^A(t)$, using a histogram of the standard deviation (relative to ECG). Assuming that a standard deviation of greater than 40 ms limits the suitability as a cardiac trigger for cardiac MRI, the figure shows that 71% of random B_1^+ shim combinations were successful and showed sufficient cardiac information available in $\vec{\Gamma}^A(t)$. For these

successful combinations, the end-systolic peak was detected with a sensitivity of 98.9%, a positive predictive value of 98.5%, and a mean trigger delay of 391 ms after the ECG R-wave with a mean standard deviation of 18.1 ms relative to ECG. Using the cardiac signal from the scattering matrix $\boldsymbol{S}(t)$, the detection of the end-systole was the most reliable (Se and PPV = 100%) and least variable during breath hold, with a mean trigger delay of 311 ms after the ECG R-wave and a mean standard deviation of 13.4 ms relative to ECG.

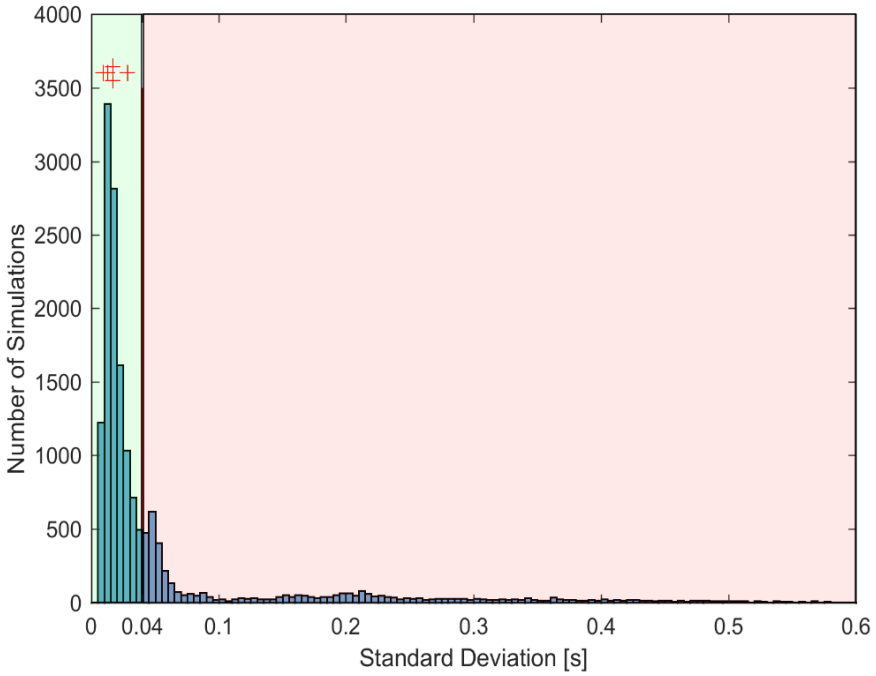


Figure 4.4: Histogram of the standard deviation of the difference in trigger time between the ECG (R-wave) and the main peak detection (end-systole), derived from the cardiac signal using all synthesised scattering coefficients $\vec{\Gamma}^{A}(t)$ (n=16000) during breath hold. The quality of the end-systole detection varies with the B_1^+ shim. The majority of shim sets has a low standard deviation compared to ECG (<40ms). Red crosses indicate the results from the cardiac signal derived from CINEs using the scattering coefficients $\vec{\Gamma}(t)$ (n=5), measured retrospectively from the imaging data.

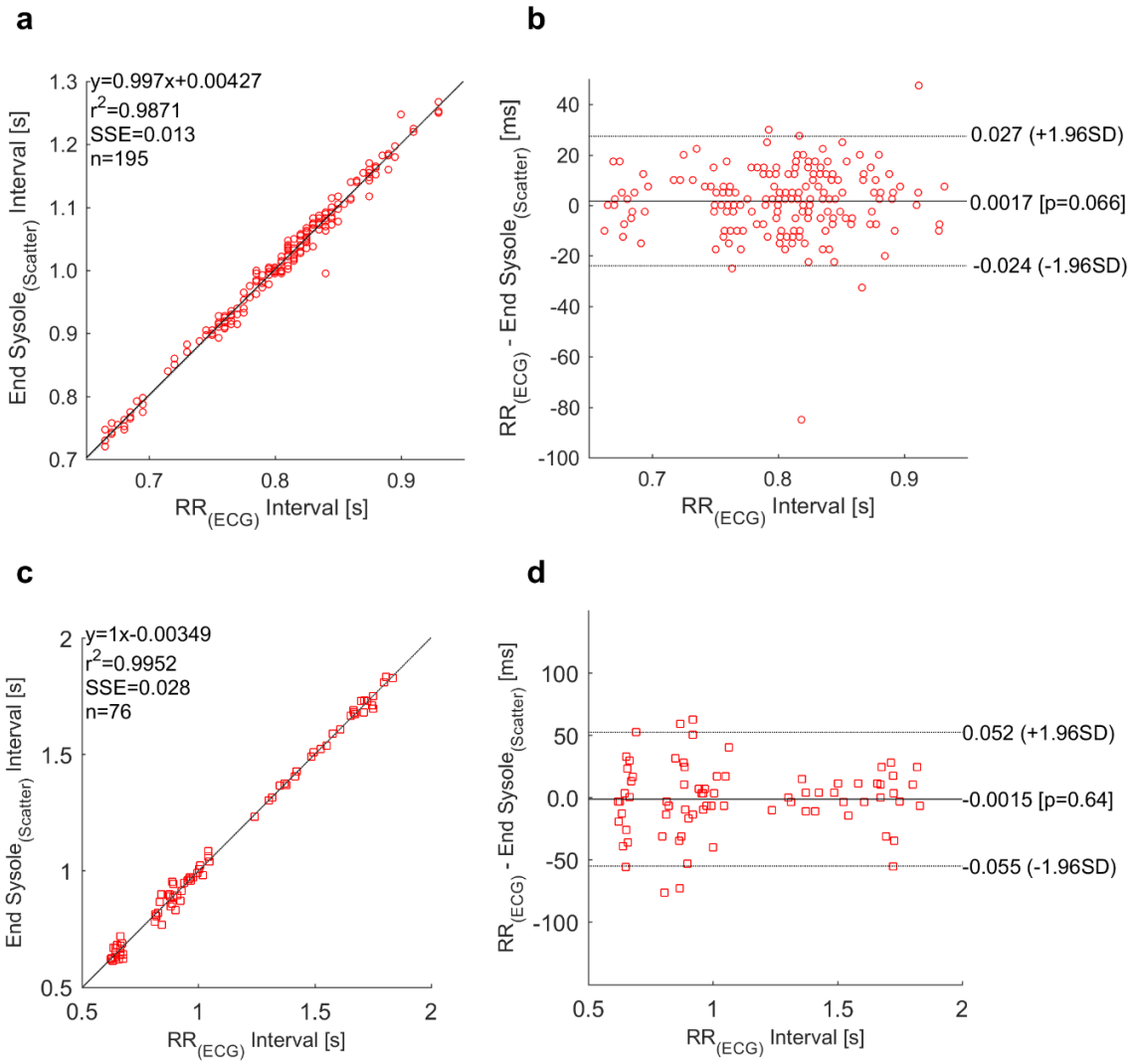


Figure 4.5: Scatter plot of the RR-interval (ECG) and the peak-to-peak feature interval (end-systole) A) derived from the cardiac signal using the scattering matrix $\boldsymbol{S}(t)$ and C) from the cardiac signal using the scattering coefficients $\vec{\Gamma}(t)$. In B) and D) the Bland-Altman plots reveal that the end systole detection occurs within a range of +24/-27 ms using the scattering matrix (B) and within a range of +52/-55 ms using the scattering coefficients $\vec{\Gamma}(t)$ (D) compared to ECG intervals. Data from all subjects during breath hold is shown.

A Bland-Altman analysis was carried out to compare the peak-to-peak interval of the end-systole feature with the peak-to-peak (RR) interval of the ECG (see Figure 4.5). The underlying cardiac signal was derived from either the S-matrix $\boldsymbol{S}(t)$ or from the normalised scattering coefficients $\vec{\Gamma}(t)$ based on cine imaging

data. The Bland-Altman plots show that the length of the peak-to-peak interval varies within -27/+24 ms and within -50/+52 ms of that calculated with ECG on a 96% confidence interval for $\boldsymbol{S}(t)$ and $\vec{\Gamma}(t)$ respectively.

Figure 4.6 plots the mean trigger delay (MTD) and standard deviation (SD) of the difference to ECG (R-peak) for each of the five gating features detected on the cardiac signal using $\boldsymbol{S}(t)$. The variability relative to ECG increased in all features during free breathing. The sensitivity and positive predictive values for all gating features are listed in table 1.

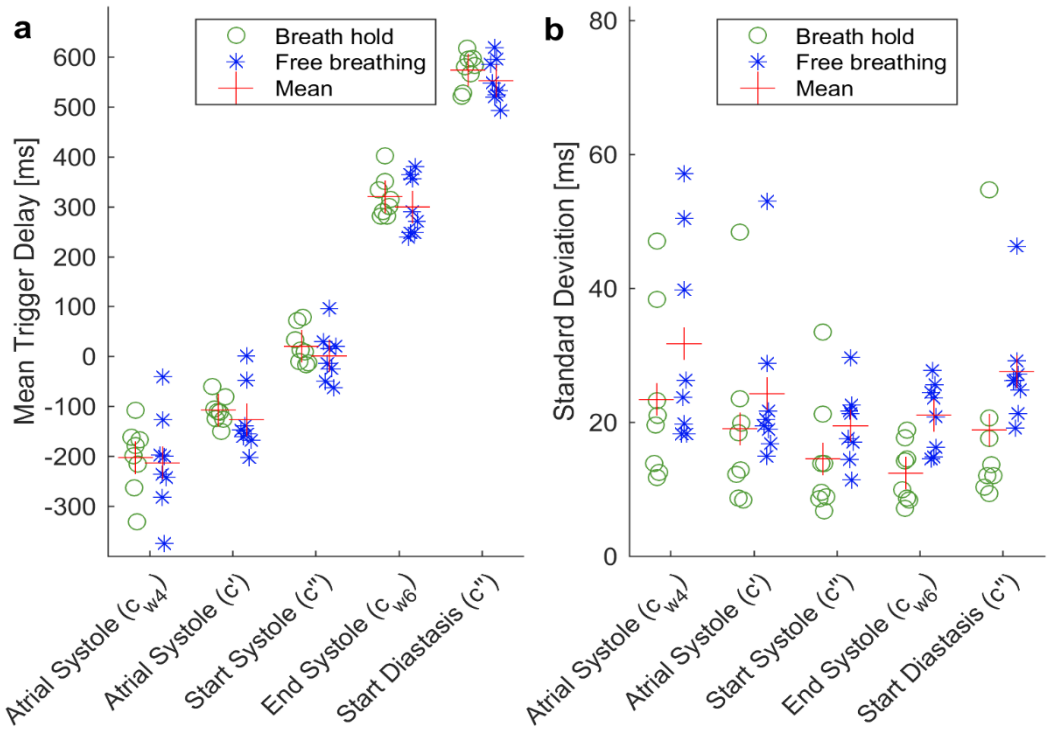


Figure 4.6: A) Intra-dataset mean trigger delay (MTD) and (B) standard deviation of the difference between the gating features and ECG trigger identified on the cardiac signal using the scattering matrix $\boldsymbol{S}(t)$. The data is grouped by different features and breath hold/free breathing. The lowest mean standard deviation is shown by the main peak detection (c_{w6}) with 13.4 ms during breath hold whereas the gating feature, which occur closes to the atrial systole, show the highest mean standard deviation.

Table 1: Summary Statistics for Gating Features

Feature ID	Breath Hold / Free Breathing	SE [%]	PPE [%]	MTD [ms]	Mean SD of the difference to ECG [ms]
Atrial Systole $\boldsymbol{c_{w4}(t)}$	Breath hold	97.7	98.0	-215	26.3
	Free breathing	93.5	97.6	-227	33.8
Atrial Systole $\boldsymbol{c'^{(t)}}$	Breath hold	96.0	96.8	-114	22.5
	Free breathing	92.4	95.7	-137	27.5
Start Systole $\boldsymbol{c''(t)}$	Breath hold	100.0	100.0	22	16.7
	Free breathing	99.6	100.0	-0.5	21.1
End Systole $\boldsymbol{c_{w6}(t)}$	Breath hold	100.0	100.0	311	13.4
	Free breathing	100.0	100.0	288	21.9
Start Diastasis $\boldsymbol{c''^{(t)}}$	Breath hold	97.4	100.0	570	22.9
	Free breathing	96.1	98.3	541	30.2
End Systole ($\boldsymbol{c_{w6}(t)}$) (scattering coeff. $\boldsymbol{\vec{\Gamma}(t)}$)	Breath hold	99.8	100.0	391	18.1

Retrospective cardiac gating, using $\vec{\Gamma}(t)$, was tested successfully in cines on five subjects with minimal differences compared to those reconstructed from ECG. The standard deviation of the difference in main peak detection time compared to ECG are plotted as the red markers in the histogram of Figure 4.4. Figure 4.7 compares the images that were reconstructed using ECG and $\vec{\Gamma}(t)$ for one subject while all five cine data sets are shown in the Appendix A in Figure 8.1.

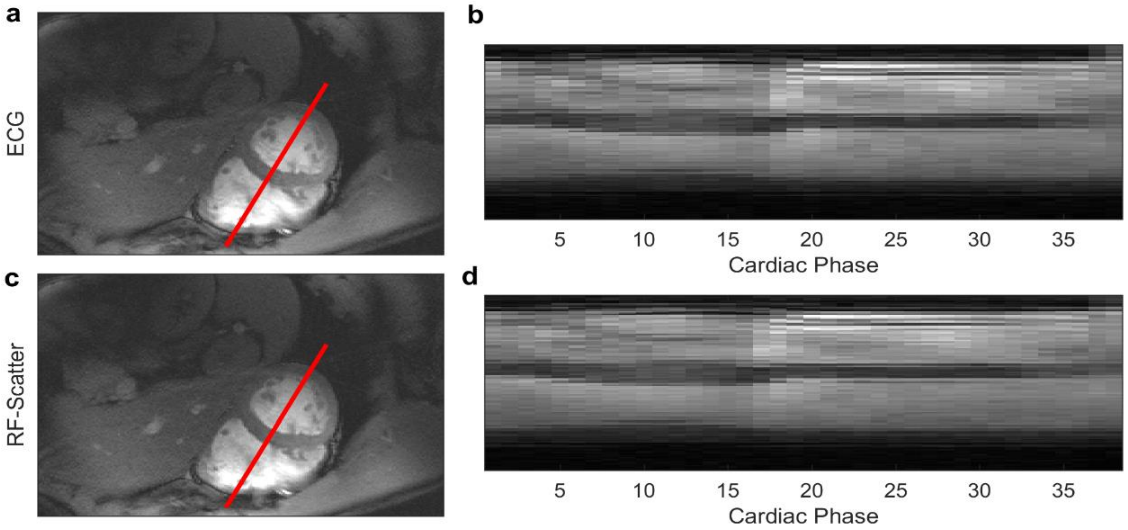


Figure 4.7: Short-axis, mid-ventricular slice and temporal profiles of a retrospectively reconstructed cine GRE sequence using A) and B) the ECG trigger signals or C) and D) the main peak detection (end-systole) derived from scattering coefficients. All images were acquired during breath hold with a temporal resolution of 29 ms, 37 cardiac phases and a total scan time of 18 s. For comparison reasons, the trigger delay of the RF-scatter triggering was aligned to ECG trigger times, prior to image reconstruction.

4.5 Discussion and Conclusion

This work has demonstrated that a cardiac surrogate signal can be extracted from the scattering of a pTx RF coil at 7T MRI by measuring either the scattering matrix $\boldsymbol{S}(t)$, using customized Gaussian RF pulses, or the scattering coefficients $\vec{\Gamma}(t)$.

The cardiac signal extracted using $\boldsymbol{S}(t)$, shows a greater SNR compared to the cardiac signal extracted using $\vec{\Gamma}(t)$. For $\boldsymbol{S}(t)$, the end-systolic peak was detected with 100% sensitivity and 100% positive predictive value. The higher SNR, when using $\boldsymbol{S}(t)$, enables identification of multiple gating features in the cardiac cycle. These other gating features aligned with early systole, start of diastasis and the

atrial contraction. The start of the diastasis shows a good overall performance and can provide additional information about the heart state compared to ECG. In subjects with high mean heart rates (>80bpm) the diastasis feature has a lower sensitivity (mean Se= 88%), which may result from a reduced duration of the resting time after passive refilling. The detection of the atrial contraction (corresponding P-wave in the ECG) has the lowest sensitivity and highest standard deviation compared to ECG gating, whereas the use of wavelets leads to a more robust but less accurate identification than using first order derivatives. The feature that aligns with the early systole has a high sensitivity and a good positive predictive value with a short trigger delay and was only outperformed by the main peak at end-systole. However, compared to end-systole, it aims to detect a rather small, subject-specific change in the cardiac signal and thus is more difficult to detect.

All gating features show a higher variance during free breathing than in breath hold (see TABLE 1). Comparing the cardiac signal during inspiration and expiration, small changes can be observed that affect the feature detection. These subtle changes may arise from genuine physiological differences in cardiac function during respiration such as a prolonged right-sided ejection time and increased venous return during inspiration [148].

The gating accuracy, when using the simulated scattering coefficients $\vec{\Gamma}^{A}(t)$, was dependent on the choice of B_1^+ shim with a large subset of B_1^+ shims providing a gating signal suitable for cine imaging. This dependency may be due to a phase cancellation effect of the resulting scattering. Nonetheless, retrospectively gated cines were successfully reconstructed using $\vec{\Gamma}(t)$, which

were measured during image acquisition, with no care in choice of B_1^+ shim other than a good B_1^+ field distribution over the heart [149]. These reconstructed cines demonstrate that using $\vec{\Gamma}(t)$ is sufficient for gating purposes and is elegant to use as no sequence or hardware modification is required. However, the cardiac signal from the scattering matrix remains superior as it outperformed that from the scattering coefficient and the peak-to-peak interval was more closely aligned to that from ECG. These improvements in gating using $\boldsymbol{S}(t)$ compared to $\vec{\Gamma}(t)$ are likely a result of the greater SNR of the cardiac signal derived from $\boldsymbol{S}(t)$.

4.6 Summary

In this chapter, I have presented a novel retrospective cardiac gating method at 7T MRI that uses RF scattering of the pTx array. The S-matrix of the pTx coil was measured using dedicated monitoring RF pulses and an algorithm was developed to extract the cardiac signal using an independent component analysis. Multiple gating features were defined in the cardiac signal and were evaluated in a small study in healthy volunteers. The pre-scan calibration and scattering gating can remove the requirement for cumbersome ECG setup for cine imaging at 7T, as it is independent of the electrical activity of the heart and therefore not affected by magneto-hydrodynamic effects. No additional hardware is necessary other than the commercially available pTx MR coil/system and the in-built safety measurement system to measure the returned and forwarded RF waveforms.

CHAPTER 5

S-MATRIX IMAGING PULSE DESIGN FOR REAL-TIME RESPIRATION AND CARDIAC MOTION MONITORING

The S-matrix of a parallel transmit (pTx) coil is sensitive to physiological motion but requires additional monitoring RF pulses to be measured. In this chapter, methods to monitor the S-matrix simultaneously with the image excitation are developed and assessed to maintain the high SNR derived from S-matrix measurements and bridge the gap between previously separated monitoring and imaging RF pulses. The goal is an RF pulse that excites an image slice and monitors the transmit S-matrix in order to generate real-time motion signals during imaging whilst not degrading image quality and minimising the RF heating.

This is particularly useful as it will not prolong the image sequence, could be used with any *k*-space sampling trajectory and is synchronised with the data acquisition. Three different RF pulse designs are evaluated. The quality of respiratory and cardiac motion signals, derived from these S-matrix measurements are compared to the use of scattering coefficients. Finally, a prospective dual gating system is evaluated in healthy volunteers at 7T.

The work of this chapter has been published in journal “Magnetic Resonance in Medicine” in 2019 [150].

5.1 Introduction

Breath-hold cine acquisitions are the gold standard for cardiac function assessments, enabling good temporal-spatial resolution but require a consistent breath hold position with good cooperation between scanner operator and patient. However, simple breath holds limit the acquisition time (<20 s) and are often not feasible for patients with limited breath hold capabilities. In paediatric patients, a consistent voluntarily suspension of breathing might also be difficult to achieve. Free breathing image acquisitions can overcome the limitations of breath holds but require accurate respiratory motion monitoring. Diaphragm navigators are a common solution for respiratory gated and tracked acquisitions [6]. Those navigators require either additional, low-resolution images that will subsequently prolong the overall scan time in continuous acquisitions or require image sequence modifications. External devices, such as respiratory bellows, can measure chest movements but will increase patient setup time and need careful adjustments for a reliable motion tracking [9], [10]. Alternative methods, as described in more detail in chapter 3, estimate cardiac and respiratory motion from surrogate signals that are derived from the continuous acquisition of the *k*-space centre [7], [102], [108], [113], [115]–[117], [122], [151], from a region-of-interest in the image domain [123], [152], or from navigators [103], [106], [153], [154] that are added to the imaging sequence.

The work in this chapter presents and evaluates pTx RF pulse designs that simultaneously excite for imaging and measure the S-matrix to generate real-time motion signals with high SNR without prolonging the image sequence.

5.2 Pulse Design for S-Matrix Measurements

To measure the S-matrix during image acquisition an S-matrix measurement RF pulse is combined with a slice selective excitation RF pulse. Three methods for simultaneous S-matrix measurement were identified from RF communications engineering [155] and include; (1) frequency division multiplexing (FDM), (2) time division multiplexing (TDM), and (3) code division multiplexing (CDM). Herein, the image excitation RF pulse function (e.g. truncated sinc) is denoted as $f(t)$ and the monitoring RF pulse function as $g(t)$. $F(f)$ and $G(f)$ are the respective Fourier transforms:

$$a\,f(t) + b\,g(t) \circ\!\!-\!\!\bullet\; a\,F(\omega) + b\,G(\omega) \tag{5.1}$$

with different scaling factors a and b.

Several conditions apply for the S-matrix monitoring schemes. The RF pulses should be orthogonal to each other on each channel, should not introduce image artefacts, should not increase the noise in the image, and should not increase the duration of the excitation pulse or alter the sequence timing. A minimal SAR burden is preferable. The following implementations are considered for these conditions.

5.2.1 Frequency Division Multiplexing

Frequency division multiplexing (FDM) allocates different frequency bands b_k for each transmit channel k, where *N* is the total number of channels. A frequency spacing Δf separates each channel. For harmonic sinusoids, the minimum Δf is

defined by the pulse length (T) as 1/T, in this work 10/T was used (10 kHz for a 1 ms RF pulse).

$$\begin{aligned} s(t) = f(t) + b\sum_{k=0}^{N-1} g(t)\, e^{-j\,2\pi(f_0+f_{off}+k\Delta f)} \;\; \circ\!\!-\!\!\bullet \;\; S(f) \\ = F(f) + b\sum_{k=0}^{N-1} G(f_0 + f_{off} + k\Delta f) \end{aligned} \tag{5.2}$$

A monitoring-frequency offset f_{off} relative to the slice-centre carrier frequency f_{slc} of the imaging RF pulse is used to avoid interference with the main imaging RF pulse and to avoid excitation of the object. For a given slice-select gradient, f_{off} is chosen so that any off-resonance excitation would be outside of the field-of-view of the coil elements. The total bandwidth B of the monitoring RF pulse is $B_{total} = f_{slc} + f_{off} + N \cdot (\Delta f + B_k)$ and is limited by the hardware specifications of the MRI system.

In this work, fermi-shaped monitoring pulses *g(t)* with the same length as the excitation RF pulse were used with a monitoring offset frequency of 100 kHz and frequency spacing of 10 kHz for each transmit channel.

5.2.2 Time Division Multiplexing

$$\begin{aligned} s(t) = af(t) + b\sum_{k=0}^{N-1} g\left(t + k\,T_g\right) \;\; \circ\!\!-\!\!\bullet \;\; S(f) \\ = aF(f) + b\,G(f)\sum_{k=0}^{N-1} e^{j2\pi f\, k\,(\frac{1}{T_g})} \end{aligned} \tag{5.3}$$

Time division multiplexing (TDM) allocates different timeslots for each channel and transmits a monitoring pulse on one channel at a time. In this work, short Gaussian-shaped monitoring pulses (T_g=35 µs) were applied at the beginning

and end of the truncated sinc-shaped excitation RF pulse $f(t)$. Therefore, the monitoring pulses do not limit the peak RF amplitude and the interference with the imaging RF pulse is decreased. The additional monitoring RF energy is spread in the frequency domain (Figure 5.1b).

5.2.3 Code Division Multiplexing

$$\begin{aligned} s(t) &= af(t) + b\sum_{k=0}^{N-1} g(t)\cdot c_k(t) \;\; \circ\!\!-\!\!\bullet \;\; S(f) \\ &= aF(f) + b\sum_{k=0}^{N-1} G(f) * C_k(f) \\ &\quad where\ c_k \perp c_{k+1} \end{aligned} \tag{5.4}$$

Where TDM and FDM enable orthogonality to the imaging RF pulse and encoding by a clear separation in time and frequency domain respectively, code division multiplexing (CDM) uses the full RF pulse length and the full transmit/receive bandwidth for all channels. Unique encoding patterns c_k enable channel identification.

In this work, I have used pseudo-random noise (PRN) encoding. Ultra-short (td=4 µs), complex, rectangular RF sub pulses were alternated in a pseudo-random fashion in the real and imaginary domain ([Real, Imaginary] = [1,0],[0,1],[0,-1],[-1,0]) to excite a broad bandwidth and to create pseudo-random noise in the frequency domain (Figure 5.1c). Each transmit channel *k* was given a distinct, pseudo-random code pattern c_k.

To avoid image artefacts, each RF sub-pulse was followed by its negative to suppress the energy at the central frequency. The randomness of the encoding pattern was restricted so that all four states occur within 8 consecutive RF sub-pulses. Remaining out-of-slice magnetization is expected to appear as noise (figure 5.1c).

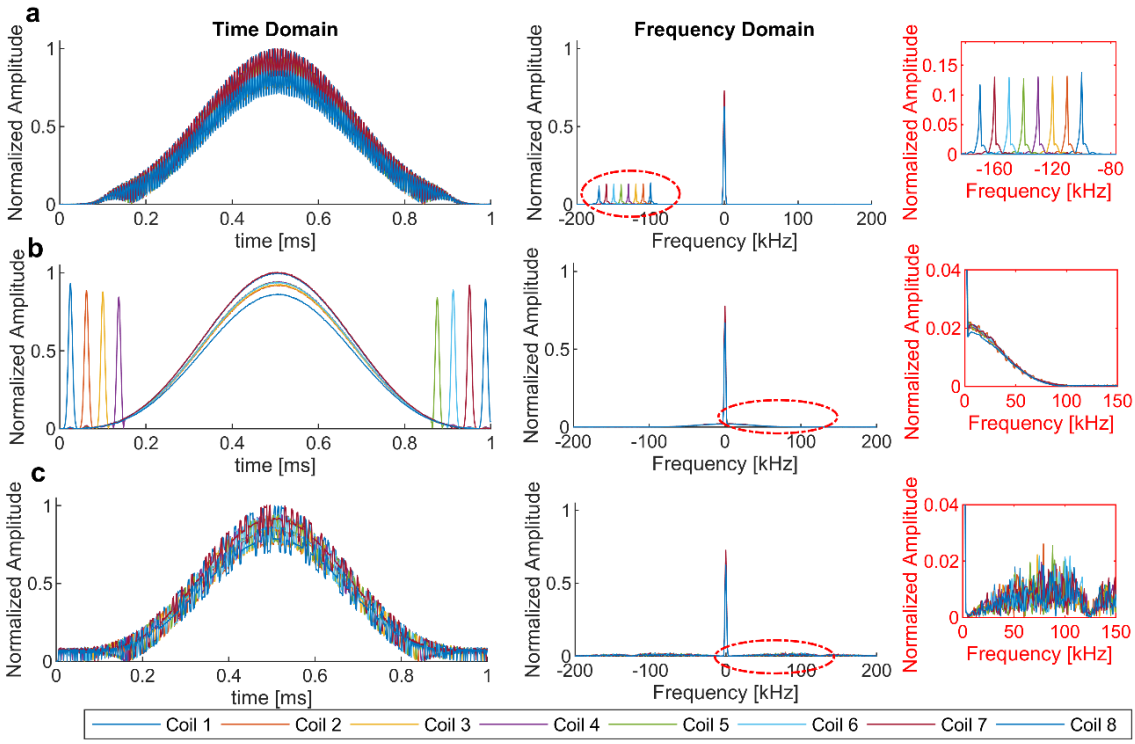


Figure 5.1: Example of overlaid imaging and S-matrix RF pulses using (A) FDM, (B) TDM, and (C) CDM. The normalised magnitudes of the complex RF waveforms, as measured by the DICOs of the MR scanner, are shown in the left column with the respective Fourier-transforms in the right column.

5.3 Cardiac and Respiratory Motion Estimation

5.3.1 Cardiac Motion Estimation

A sagittal image was acquired continually over the right diaphragm using the FDM S-matrix monitoring scheme during a training period of 72 seconds ($0.9\times5\times5$ mm^3, TR/TE = 4/1.51 ms, temporal resolution 240 ms). Motion calibration was carried out offline in MatLab (The MathWorks, Natick, MA). An independent component analysis (ICA) was used to extract the cardiac signal from the S-matrix and the scattering coefficient measurements, as in chapter 4. The polarity of the cardiac signal was determined on the dominant peak in the signal to be positive.

5.3.2 Respiratory Motion Estimation

For respiratory motion calibration, a canny edge detection algorithm, using a Sobel operator, defined the position of the diaphragm in the sagittal images (Figure 5.2a – b). The measured diaphragm positions were up-sampled in the time domain to the RF pulse sampling rate using a smoothing, cubic b-spline interpolation (see Figure 5.2c). A linear regression model was trained on the diaphragm position using the S-matrix and using scattering coefficients, similar to as described in Hess et al. [57]. In this work, a $\ell2$-norm and $\ell1$-norm penalty of the regression coefficients was added to the regression model to reduce the variance of the linear regression coefficients and to increase the robustness of the diaphragm position estimation.

Both, the coefficients of the linear regression model and the estimated cardiac de-mixing vector, were saved to a file to be used to calculate real-time motion signals on the image calculation environment (ICE) of the MR scanner for prospective gating.

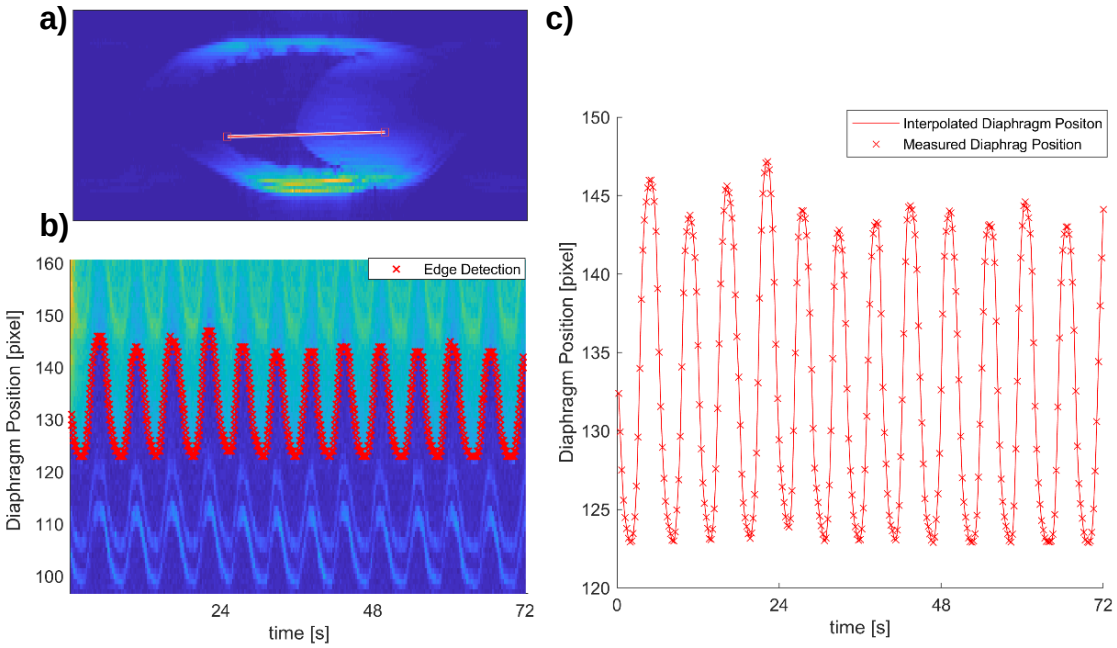


Figure 5.2: Diaphragm position extraction using a Sobel edge detection and smoothing b-spline interpolation. A) Position of the line profile image and B) the detected edges. C) The interpolated diaphragm position signal.

5.3.3 Prospective, Dual Respiratory-Cardiac Gating

Prospective cardiac gating was implemented using a Kalman filter [156], with a constant velocity model to estimate the magnitude of the cardiac vector and its rate of change (with a covariance of the observation of R=0.2 and a covariance of the process of Q=0.001). A filter model with a low covariance of the observation was chosen to minimise the filter-induced signal delay. A cardiac trigger is defined as the rate of change of the cardiac signal increasing above four (found empirically). A refractory period (close to that of the human heart) of

250 ms was used to avoid false positive trigger and to increase the robustness of the cardiac trigger algorithm.

Respiratory gating was implemented using a similar Kalman filter model to estimate the diaphragm positon with a constant velocity model (with a covariance of the observation of R=1.0 and a covariance of the process of Q=0.001). An additional feedback delay of 50 ms was used to synchronise the pTx system and the image calculation environment (ICE).

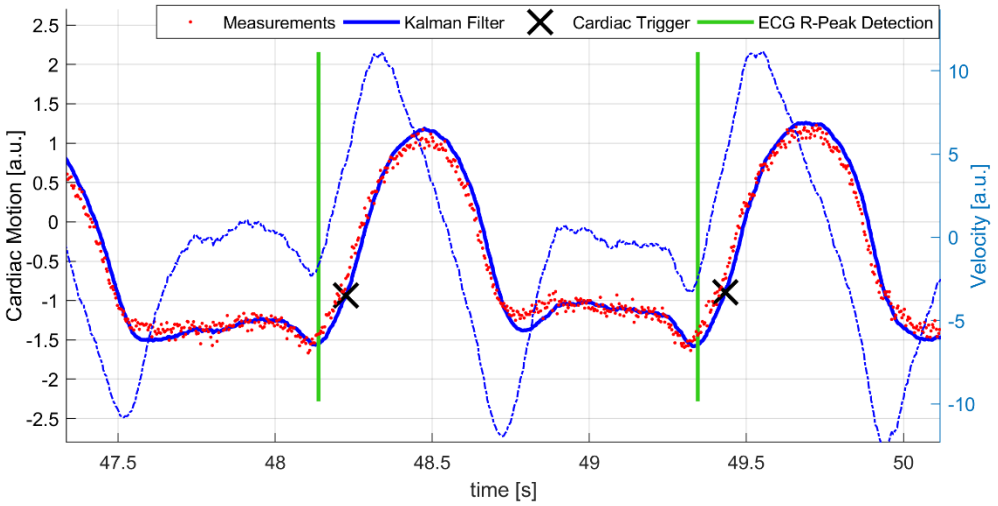


Figure 5.3: Example of two selected cardiac cycles and the prospectively measured cardiac motion. Cardiac motion signal measurements are shown with the filtered cardiac signal and the estimated velocity using a Kalman filter with a constant velocity model. ECG R-peak detection and S-matrix based trigger are shown with green lines and back crosses, respectively.

5.4 In vivo Experiments and Data Acquisition

Measurements were made on a 7T MRI Scanner (VB17, Step 2.3, Siemens, Erlangen, Germany) with an 8-channel, dipole cardiac parallel transmit/receive coil (MR Coils Zaltbommel, Netherlands). Seven healthy volunteers were recruited according to our institution's ethical practices (3 female, 4 male, age range 24-38 years, Body Mass Index = 21.5 ± 1.2) for prospective cardiac gated

MRI. Additional respiratory motion and monitoring power evaluation was carried out for 5 of these participants.

The forwarded and returned waveforms were measured using the systems directional couplers (DICOs) that are built into the transmission line of each channel and that split off a small portion of the signal. The DICOs are part of the internal safety monitoring of the scanner and can be used to measure the specific absorption rate (SAR).

5.4.1 RF Pulse Design Evaluation

Different power levels of S-matrix monitoring pulses were assessed for imaging with a breath hold cine image acquisition using a 2D gradient recalled echo (GRE) sequence ($1.4 \times 1.4 \times 5$ mm^3, TR/TE = 4.57/1.51 ms, a generalized auto-calibrating partial parallel acquisition factor of 2). The S-matrix was measured with three different monitoring schemes using modified RF pulses, as described above. Artefact images were created with the main imaging RF pulse switched off. For the power level evaluation, these images were retrospectively cardiac-gated using the extracted cardiac signal form the S-matrix measurements and the main peak detection as in chapter 4. Power levels were calculated on the measured forwarded waveforms as pulse energy per TR assuming a 50 Ω input impedance for each channel.

The quality of the extracted cardiac signal was estimated using the signal-to-noise ratio (SNR), defined as the mean peak amplitude of the cardiac signal divided by the noise. The noise in the cardiac signal was calculated as the standard deviation of the difference of a filtered (Savitzky-Golay filter [147])

cardiac signal from the unfiltered cardiac signal. For comparison purposes, an additional cardiac signal was calculated using the scattering coefficient method, as in chapter 4, that is based on the reflections from the imaging pulse alone, and its SNR was determined.

The effect on SAR of the added RF power of the three S-matrix monitoring methods was evaluated in terms of the worst-case power limit, defined as the maximum 6-min average power that is allowed on each channel. This way, for any parallel transmit configuration, the first level controlled SAR limit of 20 W/kg will not be exceeded. This mode approves the use of the dipole RF coil with a power limit of 3.8 W on each channel with the safety procedures of our institution.

5.4.2 Prospective Image Acquisition

2D cine GRE images ($1.4 \times 1.4 \times 5$ mm^3, TR/TE = 3.4/1.51 ms, and a generalized auto-calibrating partial parallel acquisition factor of two) were acquired during breath hold and free-breathing using the new prospective, dual respiratory-cardiac gating method based on simultaneous S-matrix measurements with FDM S-matrix monitoring with an amplitude of 15-20% of that of the image excitation RF pulse. A linear *k*-space encoding was used and respiratory motion states were evaluated only after each cardiac trigger to synchronise the *k*-space segments. Free-breathing images were acquired during end-expiration with an acceptance window of 5 mm.

Additional calibration data sets were acquired to calculate the root mean squared error (RMSE) between the measured diaphragm position and the offset-corrected, predicted diaphragm position using both the S-matrix and scattering

coefficients measurements. To test the stability and robustness of the dual motion estimation with respect to unexpected patient movements and exceptional respiratory pattern, three additional calibration scans were acquired with sagittal image orientation in one healthy volunteer. The volunteer was instructed to perform strong inhalation and/or strong expiration manoeuvres, as well as to move his left leg, left arm, right arm, and right leg for about 5-10 seconds each.

For all measurements, ECG triggers were recorded for comparison of the accuracy of the proposed, prospective cardiac gating algorithm. Trigger events were assumed to occur only one time during a normal heart cycle. Missed (false negatives) or additional triggers (false positives) were manually assessed by overlaying the ECG and the extracted cardiac signal.

A generalized linear mixed model was used with SPSS (Version 25.0. NY: IBM Corp) to test the differences of the three different S-matrix monitoring methods and the influence of the power level on the cardiac SNR. A multiple linear regression analysis evaluated the impact of the body-mass index of the participants on the cardiac SNR.

5.5 Results

5.5.1 Scattering Matrix Measurements: Monitoring Power and Image Artefacts

The S-matrix was calculated for all tested monitoring RF pulses. All 3 different monitoring schemes enabled retrospective cardiac gated image reconstruction using the cardiac signal derived from the calculated S-matrices. CDM and TDM monitoring show some artefacts around the anterior and posterior chest walls. FDM had no visible artefacts. Typical example images are shown in Figure 5.4 for one subject.

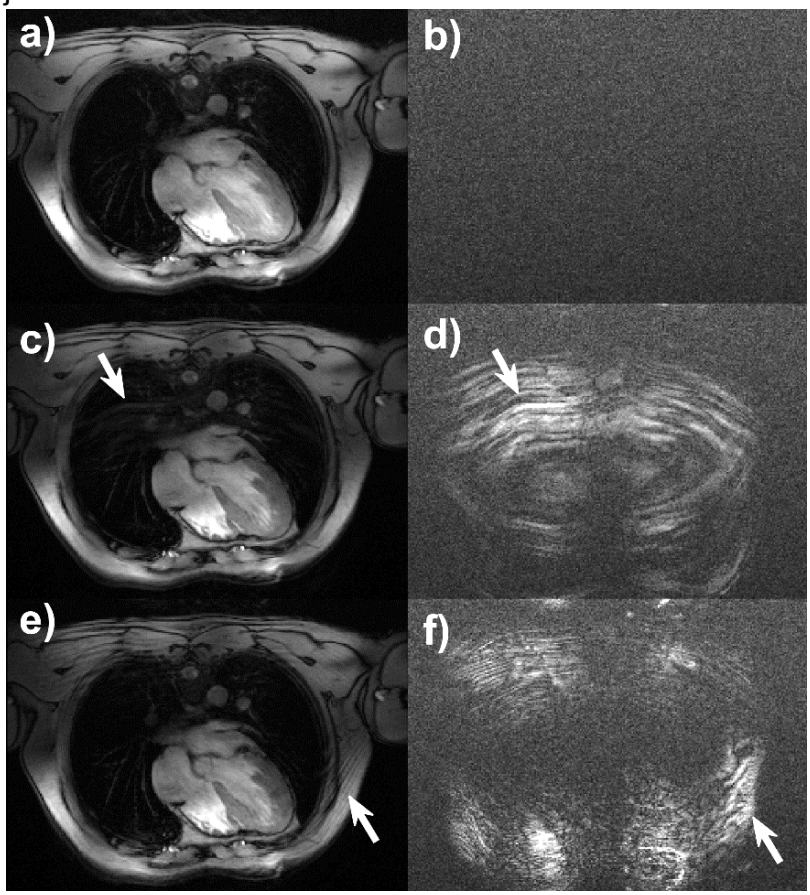


Figure 5.4: S-Matrix gated images using (A) FDM, (C) CDM, and (E) TDM during breath hold using the highest monitoring power level. In (B), (D), and (F), images with only monitoring RF pulses and the imaging RF pulse switched off are shown. Artefact introduction for CDM and TDM monitoring schemes can be observed in (C) - (D) and (E) - (F), respectively. Image intensities are increased by a factor of 10 to show the artefacts in (B), (D), and (F).

The estimated cardiac signals had a signal-to-noise ratio (SNR) of 1.1 to 31.8 for the different power levels that had RF amplitudes from 1.7% up to 20% of that of the imaging RF pulse (Figure 5.5). Using only the reflection of the normal imaging RF pulse without an additional monitoring (scattering coefficients), an average cardiac SNR of 3.6±1.2 can be achieved. No statistically significant differences related to the different S-matrix monitoring methods and cardiac SNR were observed ($F(3,44) = 2.7$, $P= 0.08$). Inter-subject variance in cardiac SNR was unrelated to the assessed, small range of body mass indices in this study ($p=0.833$).

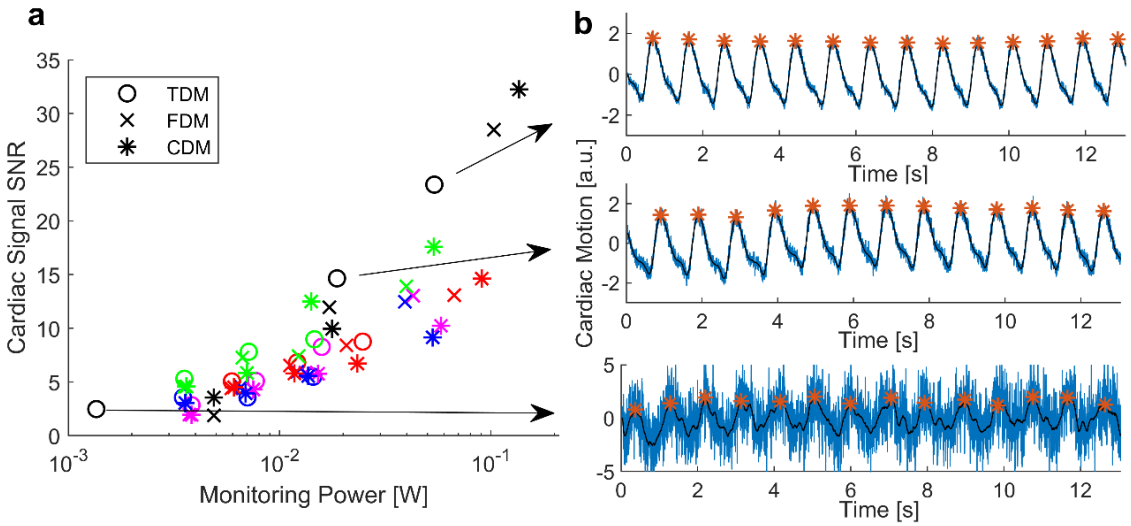


Figure 5.5: SNR for different monitoring energy levels using S-matrix monitoring with FDM, TDM, and CDM in 5 healthy subjects show with coloured markers in (A). An example of the cardiac signals derived from different S-matrix monitoring power level are shown in (B) using TDM

The maximum monitoring power level for FDM, CDM, and TDM, added 0.09 W, 0.12 W, and 0.05 W on each channel respectively. Compared to our conservative 6-min average power limit (3.8 W), the monitoring power contributed only 2.5%, 3.3% and 1.4% for FDM, CDM and TDM respectively.

5.5.2 Physiological Motion Estimation and Prospective Image Acquisition

The diaphragm position was estimated with a root mean squared error of 1.3±0.9 mm using the S-matrix measurements (FDM monitoring) and 2.3±2.3 mm using scattering coefficients. The accuracy of diaphragm position estimation is slightly reduced for larger diaphragm amplitudes and when the time between training and prediction data sets increases. Strong inhalation and expiration manoeuvres caused strongly and rapidly changing monitoring signals, during which the prospective cardiac gating algorithm as well as the ECG could not identify cardiac trigger events. The additional data sets with instructed breath holds at extreme inspiration and/or expiration positions had a larger estimation error (Figure 9.1-9.2 in the Appendix B). The diaphragm position and prospective cardiac trigger were estimated with no impact of subtle movements of extremities (arm and legs). Movements of the right arm, however, had an influence of the diaphragm position estimation and the cardiac gating signal with a following offset error in the diaphragm position estimation for the rest of the scan (see Figure 5.6).

The large majority (>99%) of cardiac cycles were correctly identified using the S-matrix FDM method in an online prospective data analysis. Two free-breathing acquisitions had false positive trigger (7 out of 148 and 3 out of 196 heart beats). The ECG had 2 missed triggers in one data set. These false positives were excluded for further data analysis. The prospective cardiac trigger had a mean temporal delay of 158±63 ms compared to ECG R-wave detection during breath hold and a mean temporal delay of 146±56 ms during free breathing. The

standard deviation with respect to ECG in cardiac trigger time was 15±16 ms for breath hold and 24±17 ms during free breathing.

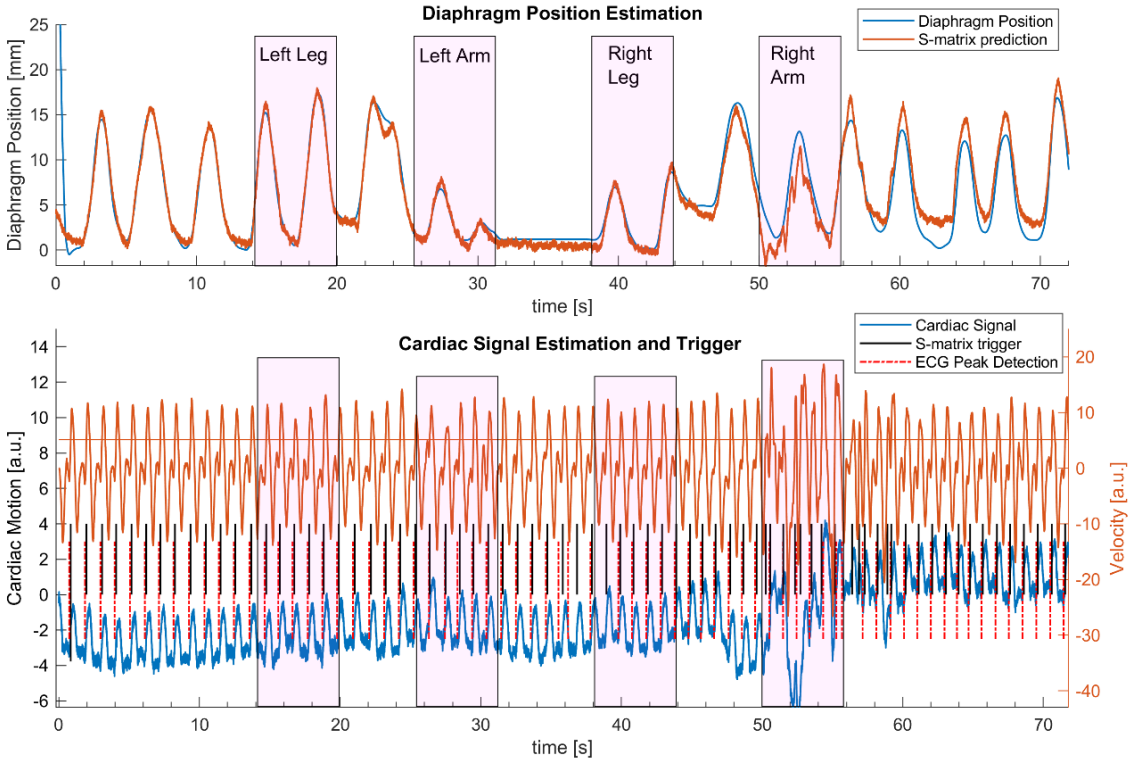


Figure 5.6: Influence on the diaphragm position estimation, cardiac signal estimation, and triggering algorithm for movements of body extremities (left arm, left leg, right arm and right leg). Periods of instructed movements are indicated with boxes. No observable influence on the estimated cardiac signal and velocity can be seen but for right arm movements. Accurate diaphragm position estimation is achieved until the initiation of right arm movements.

Free breathing CINEs, gated to end-expiration, using the dual respiratory and cardiac prospective S-matrix monitoring, were reconstructed online and demonstrated no observable respiratory artefacts in 3 out of 6 CINEs. Data from volunteer 2 had a *k*-space measurement error during the free breathing acquisition. Some blurring and residual motion artefacts around the chest-wall at end-diastole appeared for the other data sets. An example of prospective gated

cine during breath hold and free breathing is shown in Figure 5.7 with all other subjects shown in the Appendix B.

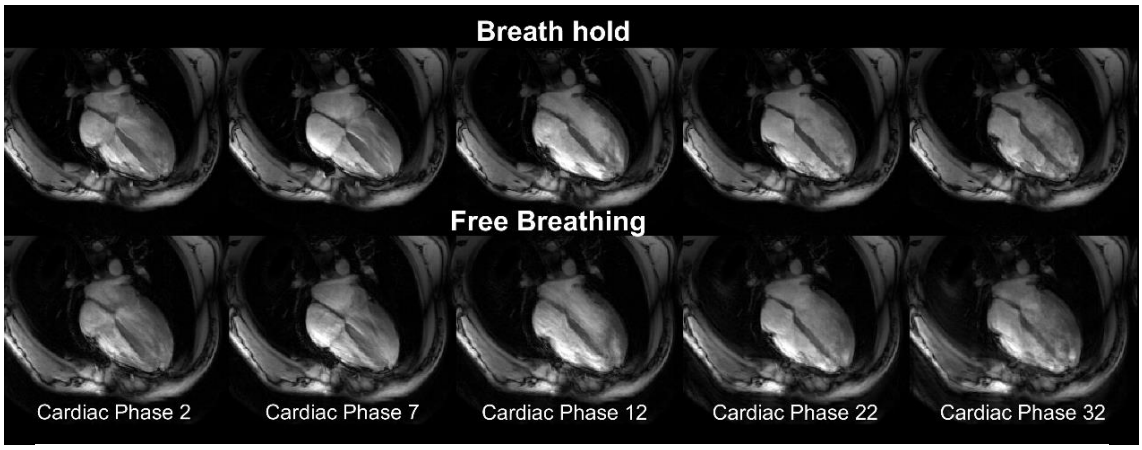


Figure 5.7: Four-chamber view of a prospectively, cardiac gated 2D cine GRE sequence using the proposed method during breath hold and free breathing. Five cardiac phases are shown, each capturing a time window of 33 ms of the cardiac cycle. From left to right, the images show early ventricular systole to end-diastole of the cardiac cycle

5.6 Discussion and Conclusion

This work demonstrated that three methods could be used to measure the S-matrix of a pTx coil at the same time as image excitation and as such do not increase or alternate the sequence duration. CDM and TDM introduced small image artefacts and FDM presented no measurable artefacts. The cardiac signals can be estimated for all tested monitoring amplitudes and methods with the SNR of the cardiac signal being proportional to the power of the monitoring pulse with all three methods demonstrating equivalent SNR for a given RF power level. This indicates that the bandwidth and/or frequency or amplitude of the monitoring scheme have no distinguishable effect on the quality of the measured motion signals.

For CDM, the RF sub-pulses should be as short as possible to spread out the energy in the frequency spectrum and away from the field-of-view of the object. In this work, a minimum of 4 µs enabled the RF amplifier to reach the requested RF amplitudes, giving a white noise bandwidth of 250 kHz. The artefacts from the CDM scheme would be reduced for shorter RF sub-pulses or a larger slice thickness. The use of a wider monitoring bandwidth does not seem to have improved the S-matrix calculation. In this work, changing the code for every RF pulse was not evaluated, it is conceivable that such a scheme would produce incoherent signal from shot to shot and would mitigate the observed artefacts.

The TDM scheme has been applied during the imaging RF pulse but each monitoring pulse could be applied at any time during the image sequence. Although TDM has shown good results for varying power levels, unwanted excitation has introduced small artefacts. Alternatively, TDM could be applied during crusher gradients to avoid image interference but would reduce its general applicability.

FDM does not introduce measurable artefacts by setting the monitoring frequency outside the range of the imaging object for a given slice-select gradient. Compared to CDM and TDM, the monitoring bandwidth is clearly separated from the imaging RF pulse bandwidth and any possible spin excitation appears outside the field-of-view of the RF coils. However, the overall monitoring bandwidth needs to be within the range of the MR system specifications and therefore limits the maximum monitoring frequency separation and offset.

The RF power for additional S-matrix monitoring is very small compared to the MR systems worst-case SAR power limit of 3.8 W per channel. The impact on

local SAR is again minimal, with highest increase found in CDM monitoring being 0.9% of the 6 min SAR limit in first level controlled mode of 20 W/kg.

Free-breathing image acquisitions were possible and the cardiac gating accuracy is comparable to retrospective gating as described in chapter 4. The diaphragm position estimation was more accurate using an S-matrix based, regularised linear regression model than an unregularised linear regression model based on scattering coefficients. No residual cardiac motion can be observed in the estimated diaphragm signal.

Small movements of extremities had no influence on the cardiac trigger detection algorithm and diaphragm position estimation. The observed influence of right arm movement and the following respiratory offset was most likely due to an unintended movement of the coil elements, which was caused by the volunteer when initiating the right arm movements. The error in diaphragm position estimation for very strong breathing manoeuvres is probably the result of a changing breathing pattern from diaphragm dominated respiratory motion to chest dominated breathing motion.

The current prospective 2D image data acquisition used a linear *k*-space encoding, where the respiratory state was updated once at the end of every heart cycle to ensure continuous and small *k*-space increments during the scan. This may have caused some of the artefacts observed at end-diastole when the respiratory state changed early within the heart cycle (see Figure 9.4-Figure 9.9 in Appendix B).

The presented monitoring approach is MRI sequence independent as it can be overlaid with any RF excitation pulse and is therefore also suitable for all *k*-space

trajectories. In comparison to navigator echoes and image-based motion estimation, it does not alter the sequence timing or prolongs the image acquisition. Further, it has the potential to reduce the patient preparation time as no additional monitoring hardware, such as ECG or respiratory bellows, is needed. In contrast to pilot-tones monitoring [132]–[135], this method requires RF pulse modification but no additional hardware.

5.7 Summary

The work of this chapter developed and evaluated three different RF pulse designs to monitor the S-matrix of a pTx coil during MR imaging with only a low, extra SAR burden and without prolonging or alternating the image sequence timing. FDM was identified as the method that does not introduce artefact with all methods providing similar signal quality for a given monitoring energy. A prospective dual gating framework was developed and implemented with FDM encoding to calculate accurate and robust cardiac trigger and respiratory motion signals on the image calculation environment (ICE) of the MR scanner in real time. The robustness of the prospective, dual-gating framework has been tested and was used to acquire 2D cine GRE images during free breathing in a small study of healthy volunteers.

CHAPTER 6

PROSPECTIVE *K*-SPACE SAMPLING STRATEGY FOR COMPRESSED SENSING 3D CARDIAC CINE DURING FREE BREATHING

The presented prospective image acquisition framework in chapter 5 uses respiratory gating and a simple linear 2D *k*-space encoding, assuming little respiratory motion and variation within one cardiac cycle. While free-breathing image acquisitions were possible and motion gating is comparable to retrospective gating, some artefacts occurred when the respiratory state changed early within the heart cycle and the respiratory state was not updated. In this chapter, I will present and evaluate a 3D Cartesian *k*-space sampling trajectory with restricted random sampling for high-resolution 3D cardiac cine images. The aim is to have a *k*-space sampling strategy that is prospectively efficient, allows retrospective motion adaptation, and presents minimal eddy-current artefacts.

6.1 Overview of Fast, 3D Imaging Strategies

Free-breathing imaging techniques allow for 3D image acquisitions with respiratory motion monitoring and/or reconstruction, which can prevent misregistration or complications of 2D multi-slice alignments and provide higher SNR. However, 3D image acquisitions require fast imaging and *k*-space acceleration techniques to achieve a high spatial and good temporal resolution in a feasible scan time.

Many acceleration techniques, which sample below the Nyquist criterion, have been developed that use temporal redundancies by sharing parts of the *k*-space in the cardiac dimension (BRISK [157], CURE [158], TRICKS [159], TWIST [160], RIGR [161], Keyhole [162], VIPR [163]). These methods assume that the dynamic and quasi-periodic changes of the heart are represented primarily by the low frequencies or centre in *k*-space, which allows for less frequently sampled outer regions of *k*-space. Existing parallel imaging techniques have been extended with the use of temporal filtering or an incorporation of different time frames (T-SENSE [164], T-GRAPPA [165]) to improve image quality of those accelerated image acquisitions. Joint spatial-temporal correlations have been utilised to increase the acceleration by undersampling in the time domain (*k*-t BLAST/*k*-t SENSE [166] , *k*-t GRAPPA [167], *k*-t PCA [168]).

Most of these methods make use of the redundancy of data to eliminate undersampling artefacts in spatial and/or time domain arising from Cartesian (fold-over artefacts) or radial (streaks) undersampling pattern.

A different approach that originated from signal processing theory, compressed sensing (CS) [169], is based on the fact that most images are sparse or highly

compressible in a suitable image transfer domain and that the entire image can be reconstructed from a small subset of the *k*-space data. A non-linear, iterative reconstruction enforces the sparsity and the consistency with the measured data. Irregular, random undersampling in *k*-space results in diffuse and incoherent artefacts, which occur like additive noise and can be removed in such an iterative optimisation process. The compressed sensing approach has been proven to enable higher acceleration factors with better image quality, when compared to other *k*-space undersampling and acceleration strategies. Consequently, most current method developments for fast cardiac imaging focus on incoherent *k*-space undersampling patterns and trajectories as well as on optimised compressed sensing image reconstruction algorithms.

These *k*-space acquisition methods include self-gated, radial stack-of-stars (iGRASP [110]) and radial spheres [170], which are commonly used for 3D cardiac imaging at 3T MRI. Cartesian trajectories have been realised as radial-like (VD-Rad [171], GOCART [172]), circular-like (CIRCUS [173]), or spiral-like *k*-space trajectories (G-CASPR [112], CASPR-Tiger [113], VD-CASPR [174], ROCK [117]). Full-Cartesian sampling trajectories have been used for 2D cardiac cine images (k-t SPARSE [175], k-t SPARSE-SENSE [176]) or for dynamic imaging with view sharing (DISCO, [177]) for abdominal imaging.

Whilst Cartesian *k*-space trajectories are more efficient to reconstruct and are less susceptible to eddy-currents and system imperfections, radial and radial-like trajectories provide a high reconstruction flexibility when using golden-angle view ordering. Each consecutive acquisition line is interleaved by the golden angle and data can be freely re-ordered and re-assigned retrospectively [178]–[181].

On the other hand, in a gridded and discrete *k*-space, overlapping of *k*-space sampling points can still occur in radial and radial-like trajectories and a continuous (re-)sampling of the centre region of *k*-space reduces the overall sampling efficiency of those methods.

6.2 *K*-space Undersampling Pattern and Trajectory

In general, long scan times for 3D high-resolution image acquisitions of ~15 minutes are more sensitive to patient motion and physiological variations, such as respiratory drifts and varying breathing patterns. The ideal *k*-space sampling trajectory needs to be flexible enough to cope with unintended variations, with physiological variations in cardiac cycle length (e.g. respiratory-induced sinus arrhythmia), and from non-uniform respiratory cycles without losing an incoherent and homogenous *k*-space sampling pattern that is needed for a good compressed sensing reconstruction for cardiac and respiratory resolved reconstruction.

In summary, a 3D Cartesian *k*-space trajectory needs to meet the following requirements:

a) An incoherent sampling pattern to enable high acceleration factors and good compressed sensing image reconstruction
b) Efficient *k*-space sampling to minimise scan time
c) Flexibility to cope with physiological and unintended patient motion
d) Reduced *k*-space traverse distances to minimise eddy current effects

The *k*-space sampling pattern and the respective sampling trajectory, which are proposed in the following sections, are compared on those terms to a spiral-like

Cartesian *k*-space trajectory with golden-angle view ordering (G-CASPR, [112]) and to an adaption for prospective cardiac gating and diaphragm navigation.

6.2.1 *K*-Space Sampling Pattern

The major requirement for high performance compressed sensing reconstruction is the appearance of incoherent artefacts created by random *k*-space undersampling pattern. “Purely” random sampling patterns, however, may lead to gaps or grouped samples, both of which are disadvantageous for parallel imaging reconstruction techniques in MRI. Random sampling with a defined distance between each *k*-space sample is preferable and realised using Poisson-disc distributions [182], which provide an incoherent but uniformly distributed *k*-space sampling pattern. In this work, undersampling factors of R = 2 to 4 are applied in the phase encoding direction in k_y for 2D image acquisitions and in k_y and k_z for 3D imaging. The read-out direction (k_x) is fully sampled. The centre region of *k*-space is fully encoded and is referred to as the calibration region (see Figure 6.1).

A variable-density distribution is used for the Poisson-disc undersampling pattern with an increased sampling rate of the centre region of *k*-space. A dense sampling of the low-frequency region of *k*-space has shown to improve the image reconstruction performance as the low-frequency Fourier basis functions correlate with most common sparsifying transformations that are used in the compressed sensing framework (e.g. wavelet transform or finite differences) [183]. Different variable-density functions are used in this work (quadratic, or biquadratic).

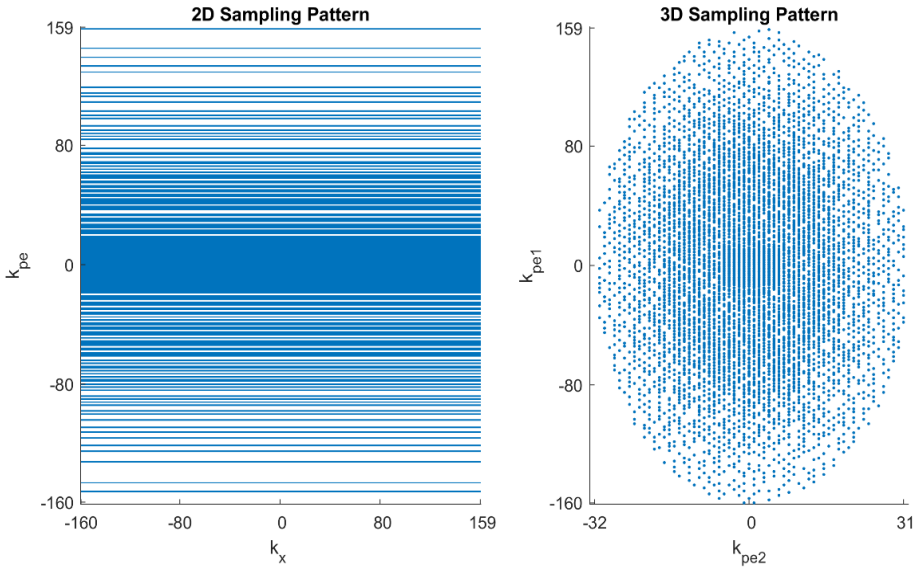


Figure 6.1: An example Poisson-disc *k*-space sampling pattern with a variable density (quadratic) for 2D and 3D imaging. A sampling matrix of 320×320 for 2D and a matrix of 320×320×64 for 3D imaging is shown with elliptic sampling (corner cut). Points in the 3D sampling pattern represent full read-out lines in k_x-direction.

6.2.2 ***C***lustered, Randomly **O**rdered **C**artesian ***K***-Space (CLOCK) Sampling Trajectory

Eddy currents arise from switching gradients and generate small, additional magnetic fields. The eddy currents degrade image quality by affecting the imaging system in two terms; 1) reducing the applied gradient field, and 2) with a constant hub or shift of the main magnetic field [184]. Although prevention and compensation mechanisms exist, residual induced magnetic fields are still present. In a linearly ordered *k*-space acquisition, neighbouring *k*-space lines experience small gradient encoding differences and the changes due to eddy currents vary smoothly over *k*-space. However, when *k*-space lines are randomly ordered, the eddy currents vary considerably for each line and therefore strong image artefacts occur.

To reduce this effect, the proposed *k*-space sampling pattern is segmented to restrict the distances in *k*-space between consecutive phase encoding lines. The *k*-space segments are herein referred to as clusters. An equal number of *k*-space phase encoding lines (typically 400-550 lines) were grouped into each cluster, which then defined the overall number of clusters. For a 3D undersampling pattern, these clusters were arranged on concentric rings around a centre cluster, which covered the middle of *k*-space. Each cluster had a pie-like shape and an equal central angle. A maximum of six clusters per ring was used and multiple rings were created to accommodate a larger number of clusters. Examples of clustered *k*-space pattern are shown in Figure 6.2.

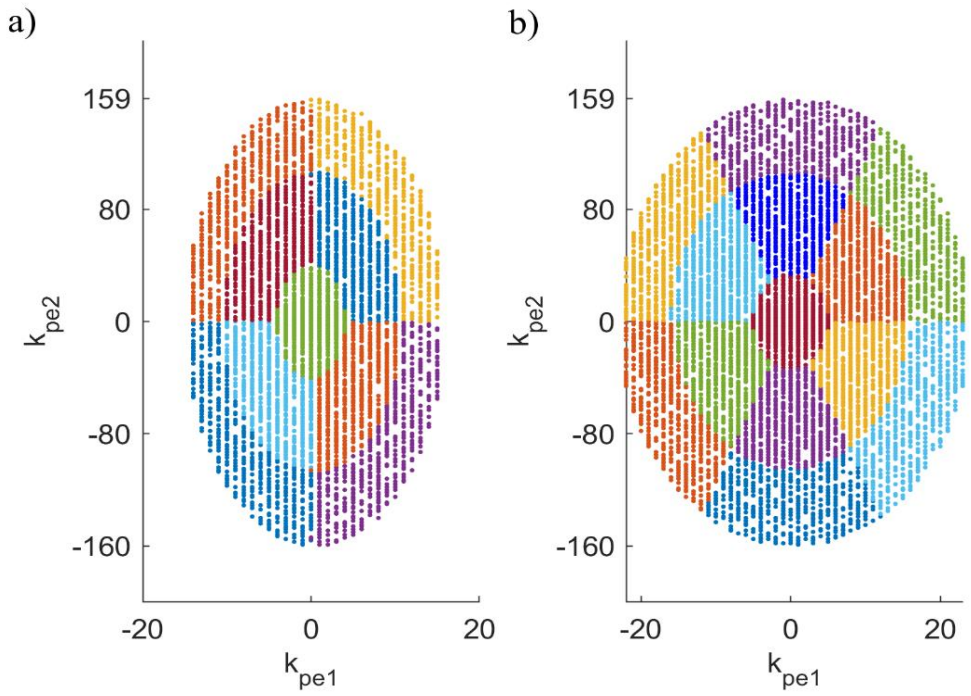


Figure 6.2: Clustered (segmented), 3D undersampled *k*-space pattern with a targeted undersampling factor of R = 2 for two different 3D *k*-space matrices are shown. Different clusters are marked with different colours. Dots represent fully acquired *k*-space lines in the read-out direction. A) A 3D CLOCK sampling pattern (320×32) with a total of 9 clusters, each of which contains 420 phase encoding lines. B) A 3D CLOCK sampling pattern (320×48) with two rings and 13 clusters, each of which contains 440 phase encoding lines.

The *k*-space sampling trajectory is created by randomly drawing data samples, i.e. desired phase encoding lines, from each cluster of the clustered sampling pattern. The clusters themselves are allocated in an elliptic centric or linear view order for 3D and 2D sampling trajectories, respectively (see Figure 6.3). The centre of *k*-space is placed in the most robust part of the acquisition, which is assumed to be after the first quarter of the scan. Further, the sampling trajectory of the central cluster is divided such that the *k*-space calibration region (most inner *k*-space lines) is acquired first. The amount of separation, i.e. the ratio of prioritised sampling to the overall number of *k*-space lines within the cluster, is chosen with respect to the expected undersampling rate of *k*-space due to physiological motion variations. For a cardiac-respiratory resolved image acquisition, the least sampled cardiac-respiratory motion state defines the motion-induced undersampling rate. If the sampling probability of the motion states is equal or lower than the ratio of prioritised sampling r_{cluster} (e.g. *k*-space calibration region), no random sampling is present in the centre cluster and the *k*-space calibration region remains incomplete. Therefore, the ratio of prioritised sampling (r_{cluster}) is chosen with respect to the mean sampling probabilities *P* of the motion states as follows:

$$r_{\text{cluster}} = \frac{N_{\text{cluster}}}{N_{\text{calib}}} \geq \frac{P(Expiration)}{P(Inspiration)} \tag{6.1}$$

with N_{cluster}, the total number of a *k*-space lines for each cluster and N_{calib}, the number of *k*-space calibration lines. The mean sampling probabilities *P* for end-expiration and end-inspiration define the minimum ratio r_{cluster}. Variations of the sampling probability of different cardiac phases within any one respiratory motion

state is expected to be small compared to the variations in the sampling probability due to respiratory motion.

Each cardiac-respiratory motion state has its own, predefined undersampling *k*-space pattern that introduces an additional random phase encoding in the cardiac and respiratory domain and enables incoherent sampling of the spatial-temporal dynamics of the cardiac and/or respiratory cycle (see Figure 6.3a). This in return will improve the compressed sensing reconstruction and provides additional flexibility for retrospective re-binning of the data in the temporal dimensions [158], [175].

Once all data is acquired for one cluster of any of the motion states, all motion states will move on to acquire the phase encoding lines of the next cluster.

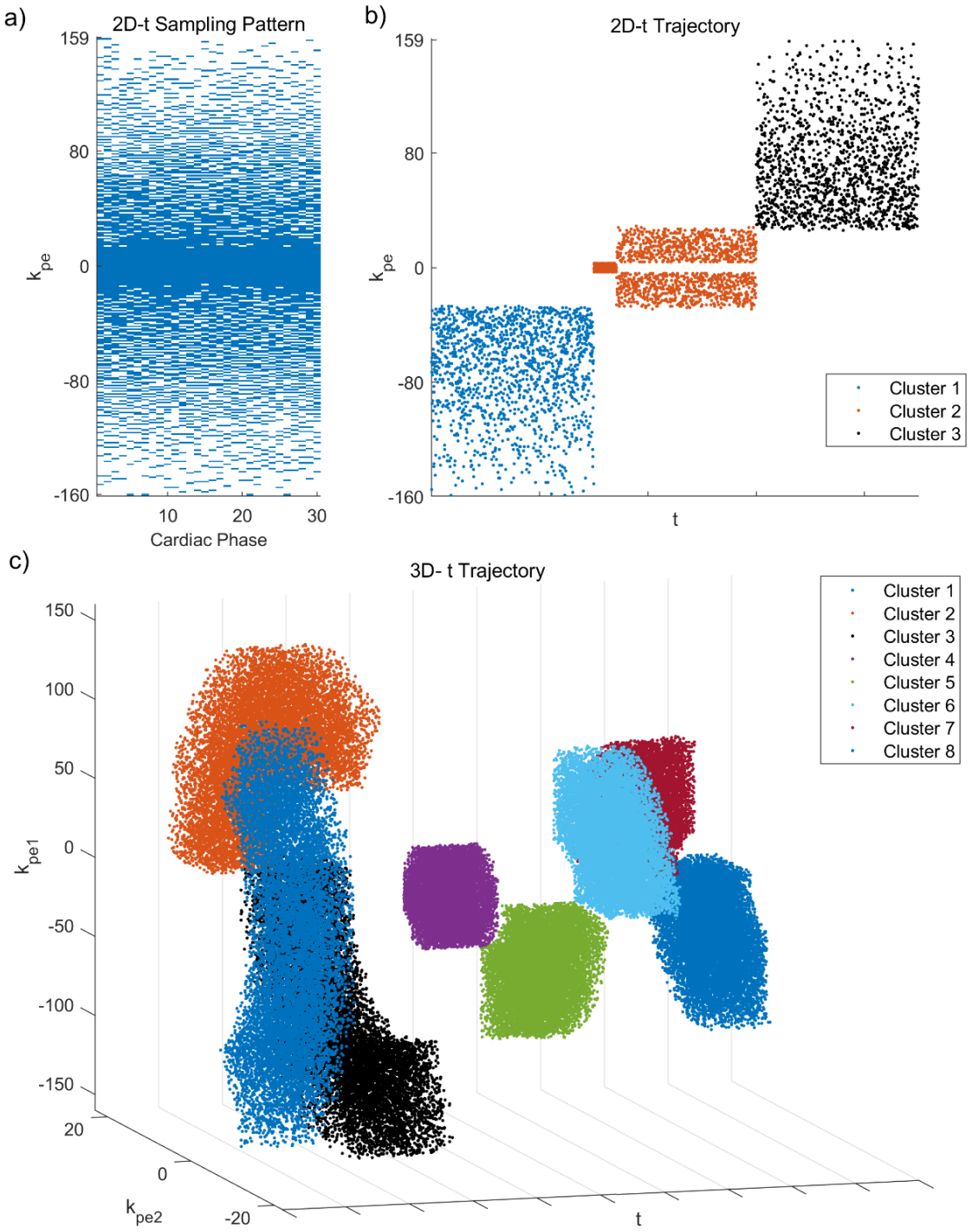


Figure 6.3: CLOCK sampling trajectories. A) Example of a 2D-CLOCK sampling pattern in the temporal dimensions of cardiac phases and B) the corresponding, simulated *k*-space acquisition trajectory for 30 cardiac phases. C) A 3D-CLOCK trajectory with 8 clusters and an elliptical mask. The clusters are acquired in an elliptic-centric order with the centre of *k*-space placed in the first part of the scan after the first ring was acquired. Single points in phase-encode directions represent fully acquired *k*-space lines in read-out direction.

6.2.3 Simulation Of Motion And Influence On *K*-Space Sampling Pattern

The acquisition time spent in each motion state varies for individual physiological motion patterns due to respiratory induced variation in the cardiac cycle and non-uniform breathing patterns. For this reason, real physiological data from 5 different healthy subjects (data from participants in chapter 5) were used to perform simulations of the prospective *k*-space sampling strategy. The aim of these simulations was to evaluate the uniformity and incoherence of the resultant *k*-space sampling in the presence of physiological motion variance and its potential effect on the image reconstruction. To quantify these variances, the coefficient of variation of cardiac phases during end-expiration as well as the ratio between the mean probability of end-expiration and the mean probability of end-inspiration was calculated.

The simulations were carried out in MatLab (The MathWorks, Natick, MA) using a 3D *k*-space sampling pattern with 320×48 phase encoding lines, a 22×8 centre calibration region, acceleration factors R = 2 and R = 4, a cubic variable density weighting function, and with a centre-cluster split-ratio of $r_{\mathrm{cluster}} = 8$. The physiological motion signals were prolonged (repeated) to meet the time requirements of the simulated 3D *k*-space acquisitions.

The *k*-space sampling efficiency, the preservation of the calibration region, and the incoherencies of the *k*-space sampling pattern for each motion state were evaluated. 3D-CLOCK trajectories with 5, 6, 7, 9, 11, 13/14, and 16 clusters were used. For comparison, simulations were run of a tiny golden-step Cartesian acquisition with spiral profile order (G-CASPR) method, first proposed by Prieto

et al. [112]. The adaptation by Usman et al. [113] (CASPR-Tiger) was used in this work. A CASPR-Tiger trajectory was implemented with N = 10 elliptic rings and N=10 angular segments, which is equivalent to the 10 *k*-space lines per cardiac phase used in the CLOCK acquisitions. For comparison, the simulated scan times for the CASPR-Tiger acquisitions were set to the average scan time of the simulated CLOCK trajectories for each motion data set. The tiny golden angle step ($\psi_7 = 23.628°$ per spiral interleaf) was kept independent of the respiratory and cardiac motion signals as proposed by Usman et al. [113]. For additional comparison, the CASPR trajectory was adapted for prospectively cardiac gated and respiratory navigated image acquisition by using pre-defined Poisson-disc undersampling pattern with variable-density (as in VD-RAD [171]) and individual patterns for each motion state. Instead of sorting according to an increasing golden angle, as in G-CASPR, CASPR-tiger, or VD-RAD, a random ordering of the phase encoding lines within each cluster in each elliptic ring was carried out to increase the incoherence of the sampling pattern. An equivalent of a tiny golden angle step of $\psi_5 = 32.039°$ was used to switch clusters for each consecutive spiral. The adapted, prospectively gated tiny golden angle Cartesian acquisition with spiral profile order, Poisson-disc ordered *k*-space points, and variable-density *k*-space pattern is herein referred to as *prospective CASPR* or *CASPR-pro*.

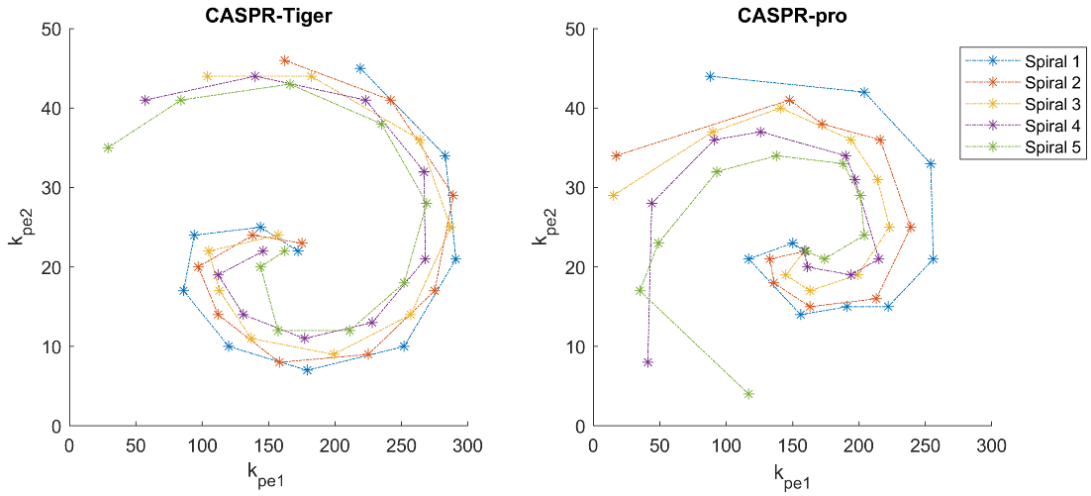


Figure 6.4: Example trajectories for the first N=5 spiral-like interleafs for CASPR-Tiger, using a tiny golden angle of $\psi_7 = 23.628°$, and CASPR-pro using a variable density undersampling mask and a tiny golden angle of $\psi_5 = 32.039°$ per spiral interleaf.

Normalised Point Spread Function (PSF) were used to measure and quantify the incoherencies as suggested by Lustig et al. [169], where the maximum of the side-lobe-to-peak ratio (SPR) was calculated.

$$SPR = \max_{i \neq j} \left| \frac{PSF(i,j)}{PSF(i,i)} \right| \tag{6.2}$$

Further, the ratio of the standard deviation of the side-lobes to the main-lobe of the PSF was used as an additional incoherence measure as suggested by Feng et al. [110], herein denoted as incoherence ratio. For simplicity, the transformation of the image into a different transfer domain (e.g. wavelet domain) was not carried out, as the image-based PSF is considered sufficient for the evaluation of different *k*-space sampling trajectories and motion-induced variances in *k*-space sampling patterns.

6.3 High-Resolution Cardiac Cine Framework

6.3.1 Compressed Sensing Reconstruction

The compressed sensing optimisation enforces sparsity in an image transfer domain and maintains the consistency of the measured multi-coil MR data set [179], [180]:

$$m = \arg\min_{m} \frac{1}{2} \|Am - y\|_2^2 + \lambda_x R_x(m) + \lambda_c R_c(m) + \lambda_r R_r(m) \qquad (6.3)$$

The matrix $\boldsymbol{A}$ transforms the multi-dimensional image set m (*x-y-z-cardiac-respiratory)* for comparison to the measured *k*-space data y (*x-y-z-cardiac-respiratory-coil*). The matrix $\boldsymbol{A}$ represents coil-receiver sensitivity maps, Fourier transformation in all spatial dimensions, and the subsampling mask.

For all image reconstruction performed in this work, the sparsity penalty functions R_x, R_c and R_r transform the image set into a sparse image representation using Daubechies D4 wavelet transform (R_x), and finite differences (temporal variation) for consecutive frames in the cardiac (R_c) and/or respiratory (R_c) dimension, respectively. The regularisation parameters λ_x, λ_c, and λ_r weight the penalty of non-sparse solutions and are empirically defined for each data set.

6.3.2 Motion Estimation and Navigation

Cardiac and respiratory motion signals were extracted using S-Matrix measurements with frequency division multiplexing (FDM) as described in chapter 5. The previously described, prospective dual cardiac-respiratory motion estimation algorithm was used for cardiac gating and diaphragm position

navigation, defining a two-dimensional space of respiratory bins and cardiac phases with cardiac-respiratory motion states (see Figure 6.5). A maximum of 310 motion states was acquired, each of which had an individual *k*-space sampling pattern.

The cardiac trigger thresholds were set for each participant after the training period and kept for the duration of the entire session. The respiratory phases were defined on the diaphragm position, spanning from end-expiration to end-inspiration with a pre-defined bin size of 3 mm. The respiratory state was updated after each cardiac phase.

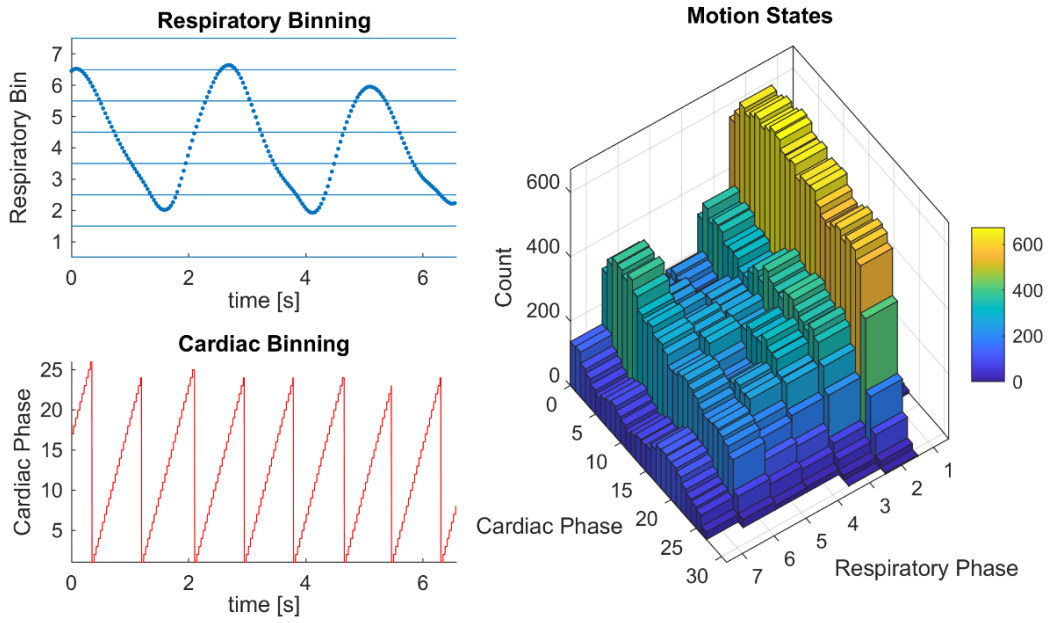


Figure 6.5: An example of respiratory (bin size=3 mm) and cardiac binning (10 k-space lines) and the definition of the 2D motion states derived from a 156s long measurement (TR= 3.4 ms).

6.3.3 Data Acquisition

All measurements were made on a 7T MRI Scanner (VB17, Step 2.3, Siemens, Erlangen, Germany) with an 8-channel, dipole cardiac parallel transmit/receive coil (MR Coils Zaltbommel, Netherlands).

6.3.3.1 Eddy Current Artefact Evaluation:

The effect of different cluster sizes, used in the CLOCK trajectory, on eddy current induced image artefacts was evaluated in a cylindrical water phantom. Different *k*-space trajectories were evaluated with a 2D GRE sequence (1 × 1 × 5 mm^3, TR/TE= 3.4/1.5 ms, FOV= 320×320, flip angle=10°). A linear ordered segmented 2D-Cartesian trajectory was compared to purely random sampling (one cluster), as well as to 2D CLOCK trajectories with 3, 5, 7 and 9 *k*-space cluster, respectively. A simulated cardiac signal was used to acquire 20 artificial cardiac phases with 10 phase encoding lines per phase. The root mean square error (RMSE) of all phantom images was calculated to quantify image artefacts. Linear phase encoded images were used as reference.

6.3.3.2 In-vivo 3D Imaging Experiments

Preliminary measurements were made with three healthy volunteers (1 female, 2 male). An S-matrix diaphragm position and cardiac signal calibration was performed as in chapter 5. Modified RF pulses, enabling S-matrix monitoring with a monitoring amplitude of 15–20% of that of the image excitation RF pulse, were used for all experiments. Real-time motion signals were calculated on the image calculation environment (ICE) of the MR scanner with a feedback delay of 50 ms. For all measurements, ECG trigger were recorded for comparison. All images were acquired during free breathing. *K*-space phase encoding lines were acquired according to the prospectively defined motion states.

High Resolution Cardiac Imaging With 2D-Clock

A high resolution, 2D cine GRE sequences (1.0 × 1.0 × 3.0 mm^3; TR/TE = 3.4/1.4 ms, α=8, acceleration factors of 2) was used with a FOV of 350 × 320 mm^2 in a

coronal image orientation with a temporal, cardiac resolution of 34 ms in volunteer 3.

High Resolution, 3D Thin-Slab Cardiac Imaging Using 3D-Clock

A high resolution, 3D thin-slab cine GRE sequences (1.0 × 1.0 × 1.0 mm^3; TR/TE = 4/1.57 ms) was used with an FOV of 416 × 320 × 24 mm^3 for volunteer 1 and with an FOV of 320 × 320 × 48 mm^3 for volunteer 2. Both images were acquired in a coronal image orientation during free-breathing with an acceleration factor of 2 and cardiac phases with a temporal resolution of 40 ms. An acceleration factor of R = 4 was used in volunteer 3 with an FOV of 428 × 368 × 44 mm^3.

At the beginning of each scan, 400 dummy RF pulses were used for a transition into the steady state. Acquisition times were 16.9 minutes, 24.6 minutes, and 18.6 minutes for volunteer 1-3, respectively.

6.3.4 Image Reconstruction using Compressed Sensing

Image reconstruction was carried out in MatLab using the BART reconstruction toolbox [185]. Sensitivity maps were estimated using the ESPIRiT [186] algorithm on the temporal averaged *k*-space data. Two sets of eigenvectors maps were used in the combined compressed sensing and parallel imaging reconstruction.

The *k*-space data of end-inspiration respiratory bins, which led to undersampling factor *R* of greater than 8, were joined retrospectively to improve image reconstruction. Retrospective, intra respiratory-bin translational (rigid) motion correction was performed in the read-out direction (superior-inferior direction) prior to the image reconstruction to improve the image quality of each respiratory bin using a simple phase modulation. The median diaphragm position for each

respiratory bin was calculated and used as reference position. All *k*-space lines acquired within one respiratory bin were corrected to the respective median respiratory bin position with a diaphragm-to-heart motion translation factor of 0.6, as suggested by Wang et al. [5]. All image reconstructions were carried out on a high-performance computer equipped with a 32-core CPU and 128 GB RAM. Image quality was compared using line diagrams through the myocardium and the right atrium.

6.3.4.1 Cardiac Resolved Image reconstruction

Image reconstruction with an additional cardiac dimension was performed at end-expiration. The end-expiration bin was identified as the bin with the maximum number of samples. In cases of drifts in the respiratory signal (linearly varying end-expiration, diaphragm position), the edges of the end-expiration bin were redefined retrospectively and *k*-space data was reordered accordingly.

The spatial regularisation parameter λ_x for a wavelet transformation in all spatial dimensions was found empirically for each data set. The optimal parameter λ_x reduced the undersampling artefacts without introducing streaking artefacts or over-smoothing (see Figure 6.6). The temporal variation (finite differences) was used in the cardiac dimension with a regularisation parameter λ_c, which was empirically defined after the spatial regularisation parameter was set. The optimal parameter λ_c reduced image artefacts in the temporal (cardiac) domain without introducing blurring in the images.

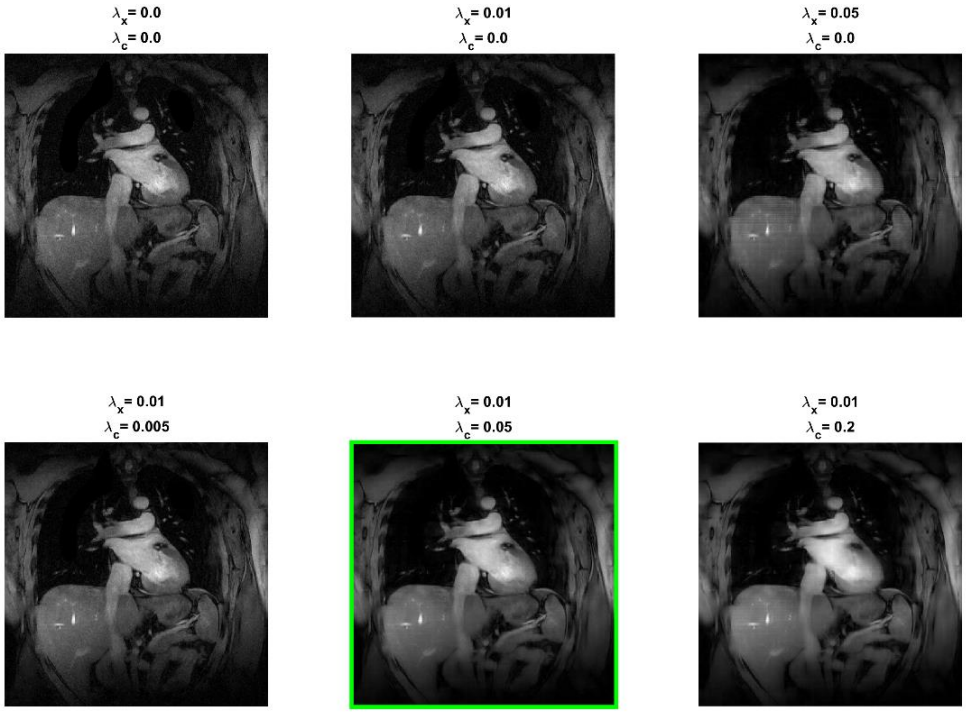


Figure 6.6: Representative reconstruction examples for cardiac-resolved images using different regularisation parameter combinations on a healthy volunteer with an undersampling factor of *R* = 2. The spatial regularisation parameter λ_x promotes sparsity in the wavelet transform domain (upper row). Large parameter lead to over-smoothed images and the introduction of streaks in the image. Additional regularisation the cardiac domain reduced most undersampling artefacts. Large parameter λ_c lead to strong blurring.

A spatial regularisation parameter of $\lambda_x = 0.05$ and cardiac regularisation parameters of $\lambda_c = 0.05$ and $\lambda_c = 0.06$ were used for the 3D data sets acquired on volunteer 1 and volunteer 2, respectively. The parameters $\lambda_x = 0.005$ and $\lambda_c = 0.06$ were used for the data sets that were acquired on volunteer 3, which had a target undersampling factor of R = 4.

6.3.4.2 Cardiac-Respiratory Resolved Image Reconstruction

In volunteer 3, the 2D images used for cardiac resolved image reconstruction were also used to reconstruct 2D cine images in an additional respiratory dimension. Total variation (TV) regularisation was performed in the respiratory

dimension as well as in the cardiac dimension. Regularisation parameters in the cardiac dimension of $\lambda_c = 0.06$ and in respiratory dimension of $\lambda_r = 0.005$ were used with a spatial regularisation parameter of $\lambda_x = 0.002$.

6.4 Results

6.4.1 Overview of Physiological Traces used in Simulations

As expected, the evaluated sampling probability of different motion states varied strongly for different respiratory and cardiac motion signals. On average, the evaluated motion signals had a length of 104±45 s with a mean respiratory rate of 14±4 bpm and an average diaphragm amplitude of 15.9±3.3 mm. The end-expiration position varied with a standard deviation of 0.5 mm, whereas the end-inspiration position varied with a standard deviation of 3.1 mm. An example data set with a normal respiratory and cardiac motion pattern is shown in Figure 6.7.

The sampling probabilities of cardiac phases during end-expiration had a mean coefficient of variation of 9.3%, where one data set had a coefficient of variation of up to 25%, introducing a large amount of variation between cardiac phases in the end-expiration bin. An average sampling probability ratio of cardiac phases of 4.7 was calculated between the end-expiration bin and end-inspiration bin. Strong and irregular breathing pattern increased the probability ratio between respiratory states. Irregular and large inhalations were observed in two data sets form the same volunteer, which have led to probability ratios of 8.3 and 11.1 in these data sets.

The effect of respiratory induced sinus arrhythmia (RSA) was present in all data sets, leading to a shortening of the cardiac cycle length during inspiration. The heart rate variability was higher in subject groups with lower resting heart rate (<60 bpm), with an average standard deviation of 130 ms, compared to subjects with a higher resting heart rate (>=60 bpm), with an average standard deviation of 55 ms.

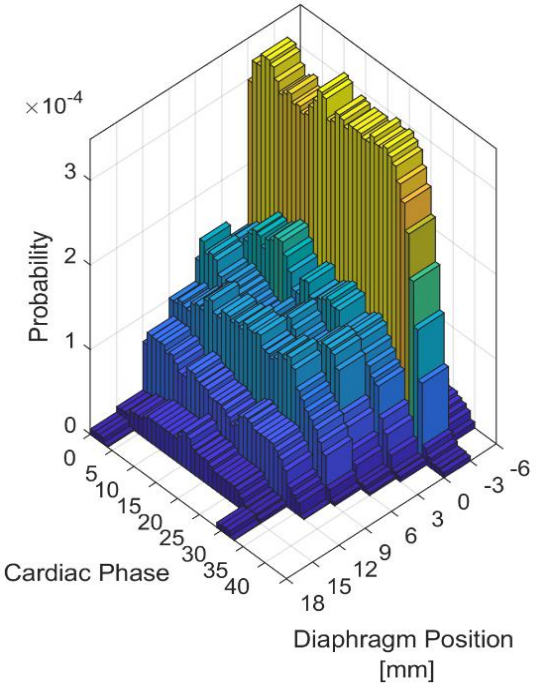


Figure 6.7: Example data set and motion state evaluation with little variation in the sampling probabilities. The normalised sampling probability is shown for all motion states in the respiratory (diaphragm position) and cardiac phase dimension. The effect of respiratory induced sinus arrhythmia can be observed with a shortening of the length of the cardiac cycle during inspiration.

6.4.2 Simulations of *K*-Space Trajectories in the Presence of Motion

The length of the simulated image acquisitions varied strongly according to the underlying motion pattern. A mean acquisition time of 41.8 ± 10.9 minutes and 21.2 ± 5.5 minutes for a targeted undersampling factor of $R = 2$ and $R = 4$ respectively was simulated. The respiratory and cardiac variations within each subject defined the time spent in each motion state and thus the respective undersampling factor R. The side-lobe-to-peak ratio (SPR) increased with a higher undersampling factor R, whereas the incoherence ratio decreased. A mean incoherence ratio of 194.0, 194.0, 193.3, 192.4, 191.8, and 193.2 was calculated for CLOCK trajectories at end-expiration with a targeted undersampling of $R = 2$ and with 6, 7, 9, 11, 14, and 16 clusters, respectively. For a full random trajectory, a mean incoherence ratio at end-expiration of 194.1 was calculated. The golden angle spiral-like trajectory (CASPR-Tiger) had a mean incoherence ratio of 164.7 and the prospective random ordered adaptation (CASPR-pro) an incoherence ratio of 181.5 at end-expiration. The mean SPR ratio at end-expiration was 0.023 for a full randomly sampled trajectory. CLOCK trajectories had a mean SPR of 0.0222, 0.0227, 0.0222, 0.0226, 0.0225, 0.022, using 6, 7, 9, 11, 14, and 16 clusters, respectively. CASPR-Tiger and CASPR-pro had a mean SPR of 0.0313 and 0.0243, respectively. Figure 6.8 shows an example of normalised point-spread-functions (PSF) and the respective *k*-space sampling patterns, which were calculated for different motion states using a 3D CLOCK trajectory with 6 cluster.

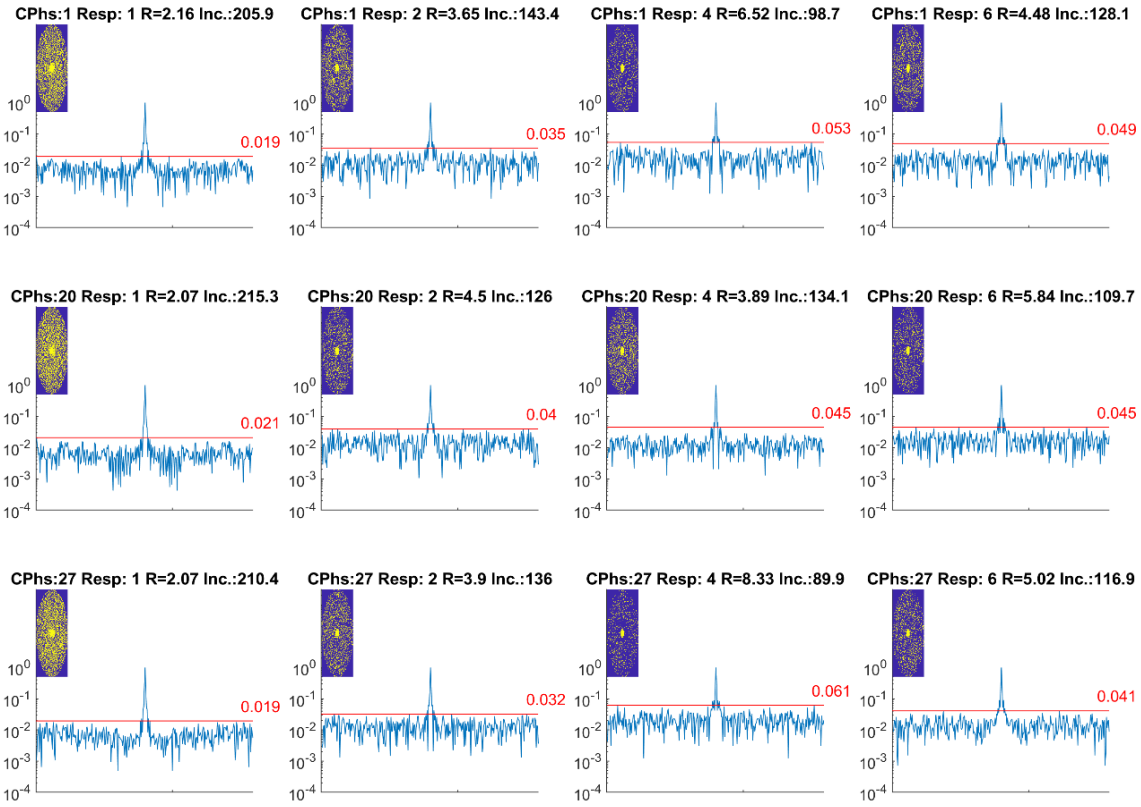


Figure 6.8: Calculated and normalised Point-Spread-Functions (PSF) and incoherence measures for different cardiac (CPhs) and respiratory (Resp) motion states, as simulated in one subject, using a CLOCK trajectory with 6 clusters. The central lines through the 2D PSF are shown with the respective undersampled *k*-space pattern in the upper left corner of each PSF image. Different rows show the *k*-space sampling and PSF for the cardiac phases 1, 20, and 27 within the respiratory bins 1, 2, 4, and 6 shown in the different columns, respectively. The red lines indicate the peak side-lobes in the PSF, with the calculated maximum side-lobe-to-peak ratios (SPR) in red.

A statistically significant difference ($p<0.001$) was calculated for the incoherence and SPR measures at end-expiration of CASPR-Tiger and CASPR-Pro when compared to the clustered random methods using paired-sample t-tests. No statistical difference was calculated between different clustered random trajectories. Figure 6.9 and Figure 6.10 show boxplots of all SPRs and

incoherence ratios, grouped into different respiratory bins and different *k*-space trajectories using target undersampling factors of R = 2 and R = 4, respectively.

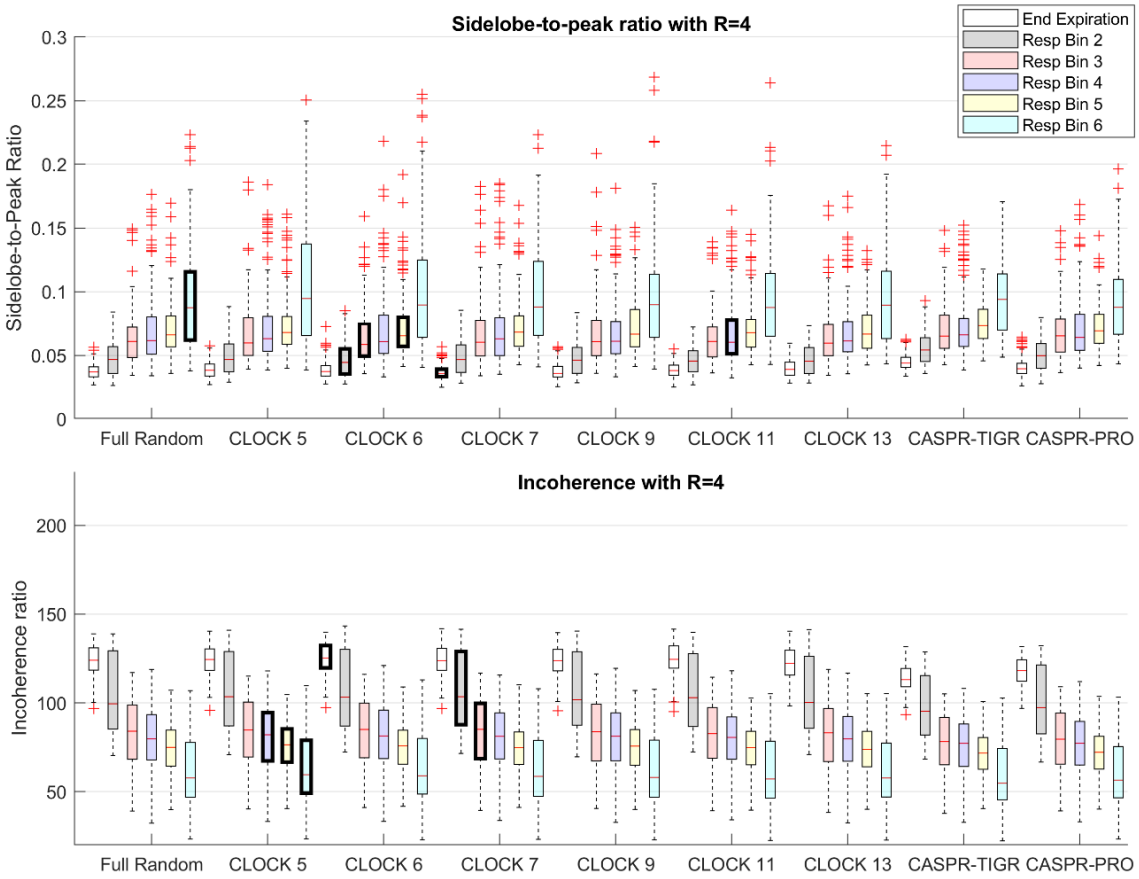


Figure 6.9: Boxplots of the SPRs and incoherence ratios for each motion state, grouped into different respiratory bins and different *k*-space trajectories. A target undersampling factor of R = 4 was used. The lowest SPRs and highest incoherence ratios for each respiratory bin are highlighted with thickened boxes.

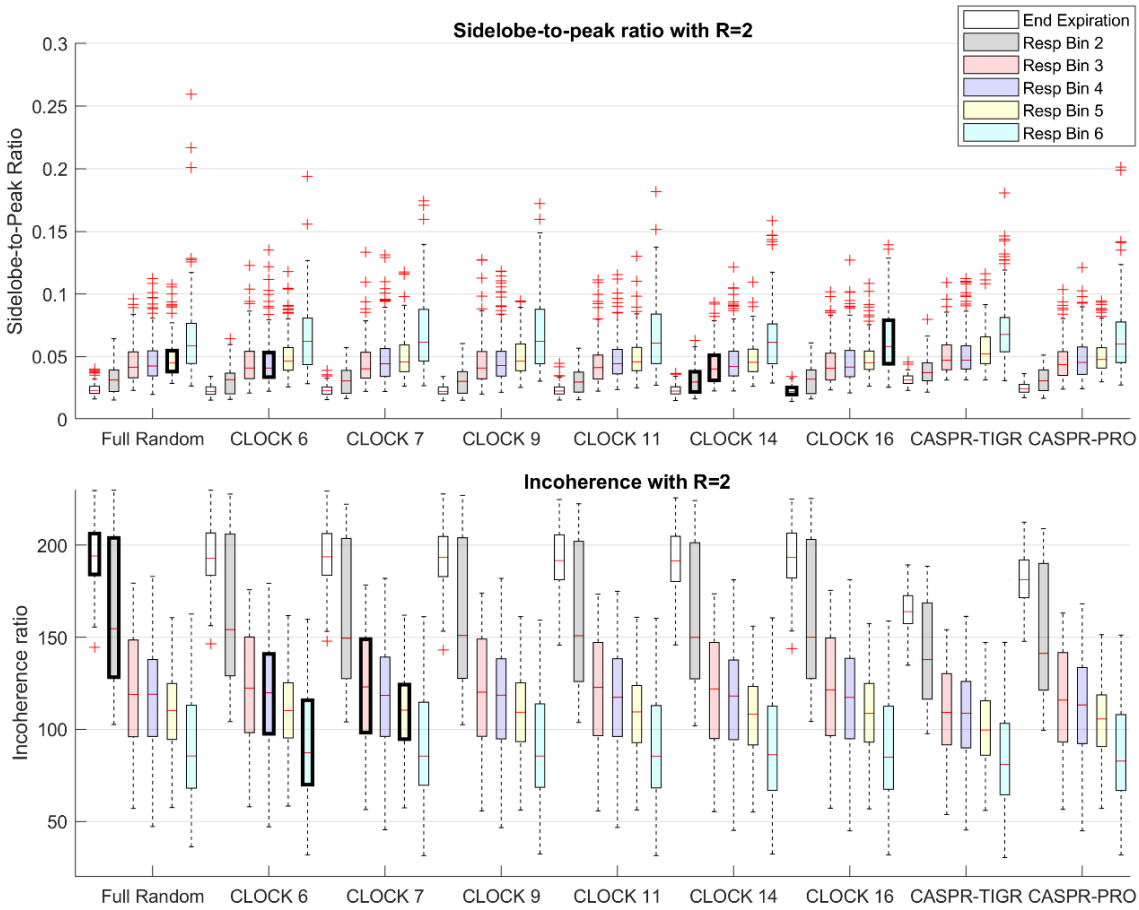


Figure 6.10: Boxplots of the SPRs and incoherence ratios for each motion state, grouped into different respiratory bins and different *k*-space trajectories. A target undersampling factor of R = 2 was used. The lowest SPRs and highest incoherence ratios for each respiratory bin are highlighted with thickened boxes.

By definition, all simulated CLOCK trajectories had a sampling efficiency of *k*-space of 100%, with no *k*-space line acquired twice for a given motion state. An average efficiency of 82.6±1.9% and 90.1±1.7% was calculated for CASPR-Tiger and of 92.6±0.66% and 92.6±0.61% for CASPR-pro for target undersampling factors of 2 and 4, respectively. A comparison of CASPR-Tiger, CASPR-Pro, and CLOCK with 7 clusters is shown in Figure 6.11 with an example of a simulated, undersampled *k*-space pattern (320×48, R = 2), calculated PSFs, and respective incoherence ratios.

A higher undersampling ratio *R* in CASPR-Tiger and CASPR-pro trajectories can be observed due to an oversampling of the centre *k*-space region.

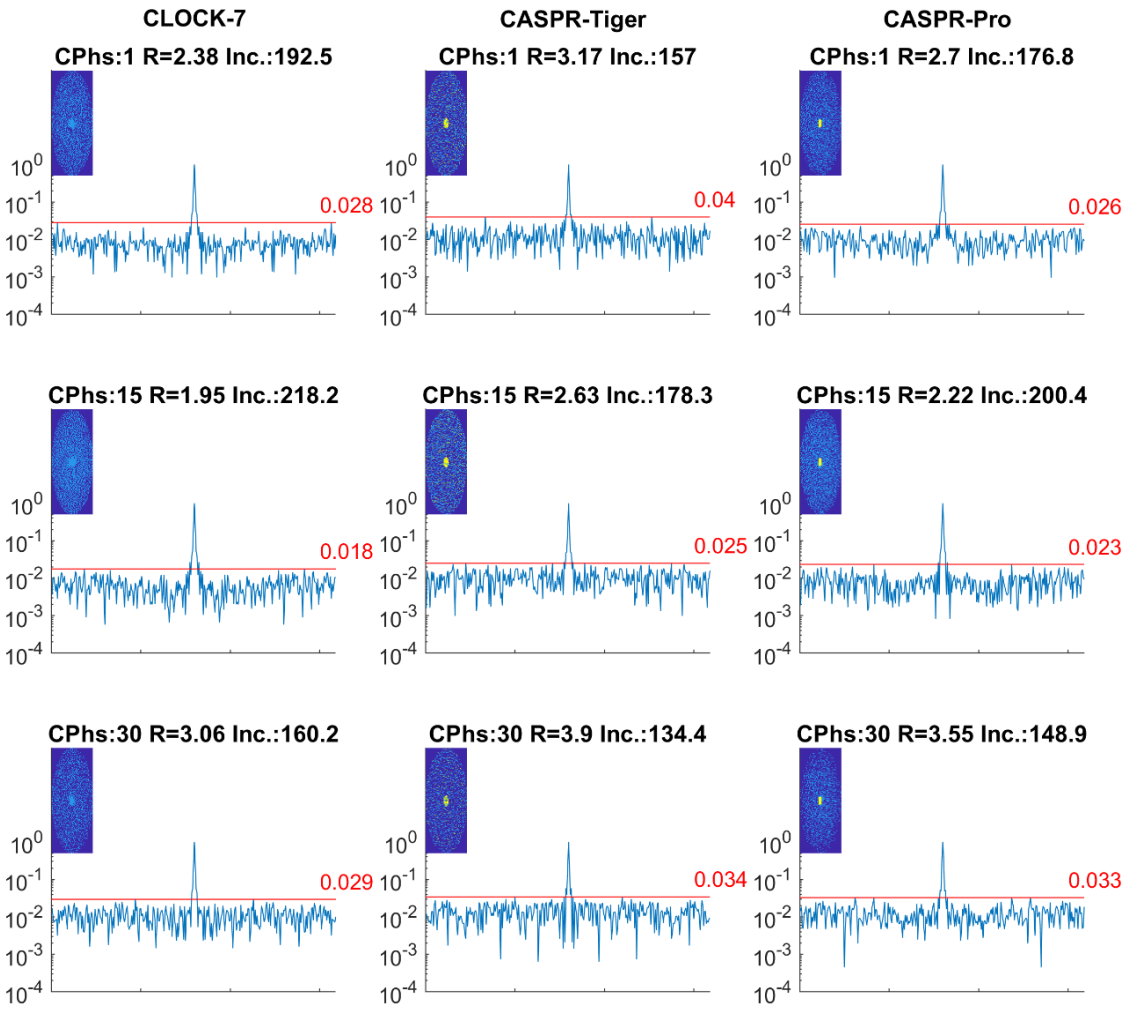


Figure 6.11: Comparison of *k*-space pattern using a simulated CLOCK trajectory with 7 clusters and CASPR-like trajectories at end-expiration. A central line of the 2D PSF is shown. Red lines indicate the peak side-lobes in the PSF, with the calculated maximum side-lobe-to-peak ration in red.

6.4.3 Phantom Measurements and Eddy Current Effects

Figure 6.12 shows fully sampled 2D GRE images that were acquired by either randomly select phase encoding lines, 2D CLOCK trajectories using 3, 5, 7 or 9 clusters or by using a standard linear phase encoding trajectory. The introduction of clusters to restrict the traverse distances in *k*-space reduces the occurrence of image artefacts and the calculated RMSEs when compared to a full-random trajectory. An RMSE of 0.027, 0.013, 0.014, 0.015, and 0.013 was calculated for fully random selected phase encoding lines and with the use of 3, 5, 7, and 9 clusters, respectively.

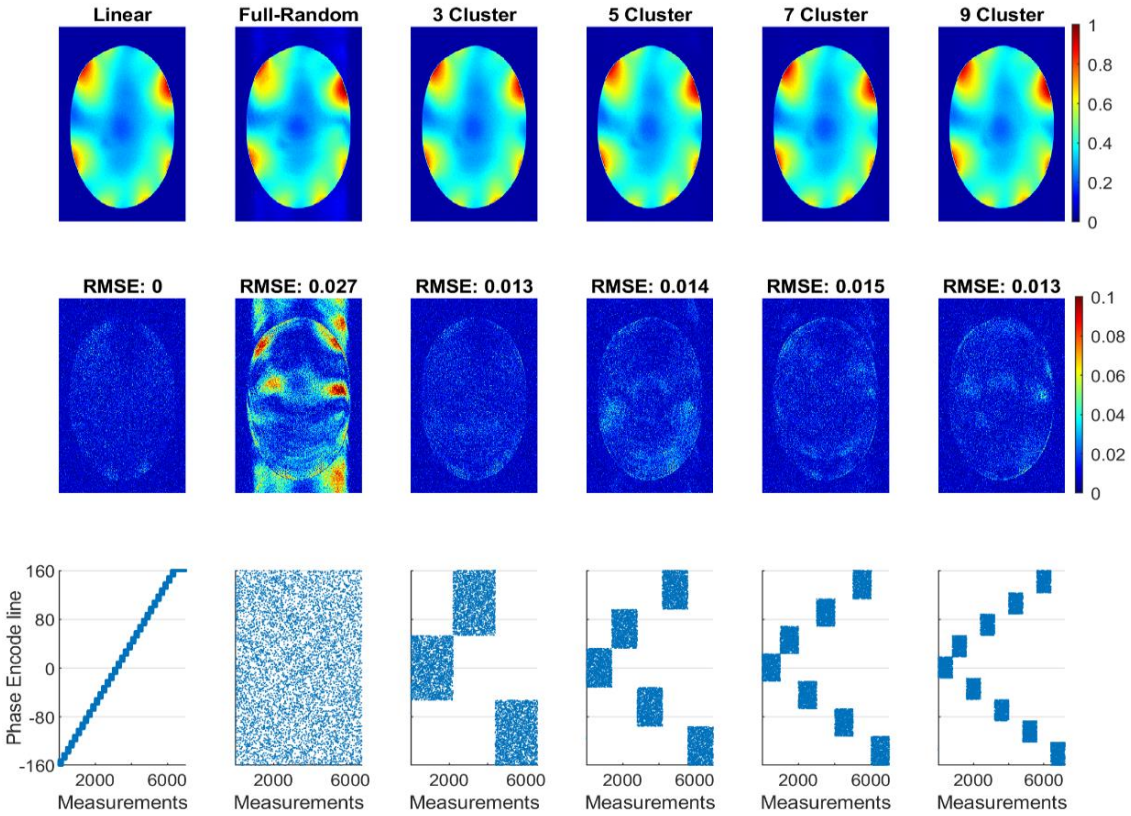


Figure 6.12: Phantom measurements using different 2D CLOCK trajectories. Images for one cardiac phase are shown in the upper row. The difference images to a reference image with linear encoded *k*-space trajectory are shown in the middle row. A reduction of eddy current induced artefacts can be seen with the introduction of clustered *k*-space compared to a fully random trajectory. The lower row shows the *k*-space trajectories used to acquire the images.

6.4.4 High Resolution Cardiac CINE

3D high-resolution, free breathing cardiac cine images were successfully reconstructed at end-expiration and demonstrated no observable reconstruction artefacts in the heart for volunteer 1 and 2 using the prospective, dual cardiac-respiratory S-matrix monitoring and 3D CLOCK trajectory. Some residual image artefacts were observed in the abdomen and in the image data set acquired on volunteer 3. Image wrapping effects were observed in all data sets in the anterior-posterior direction resulting from the 3D thin-slab excitation volume (see Figure 6.13). The 3D image acquisition times were 16.9 minutes, 24.6 minutes, and 18.4 minutes for volunteer 1-3, respectively. Re-binning of end-expiration was necessary for volunteer 2 and volunteer 3. The mean image reconstruction time was 34 minutes for the cardiac-resolved 3D image data sets at end-expiration. Representative coronal images of the cardiac-resolved, high-resolution 3D image data set at end-expiration are shown during end-systole and end-diastole for volunteer 1 in Figure 6.13, for volunteer 2 in Figure 6.14, and for volunteer 3 in Figure 6.15.



Figure 6.13: Representative coronal images acquired in volunteer 1 using the proposed prospective motion navigation and the 3D CLOCK trajectory with 9 clusters and a targeted undersampling of R = 2. High-resolution (1.0 × 1.0 × 1.0 mm^3) images with a slab-thickness of 24 mm are shown at end-expiration during systole and diastole in the upper and lower row, from posterior (left) to anterior (right), respectively. Image wrapping artefacts are present in posterior images and indicated with white arrows.

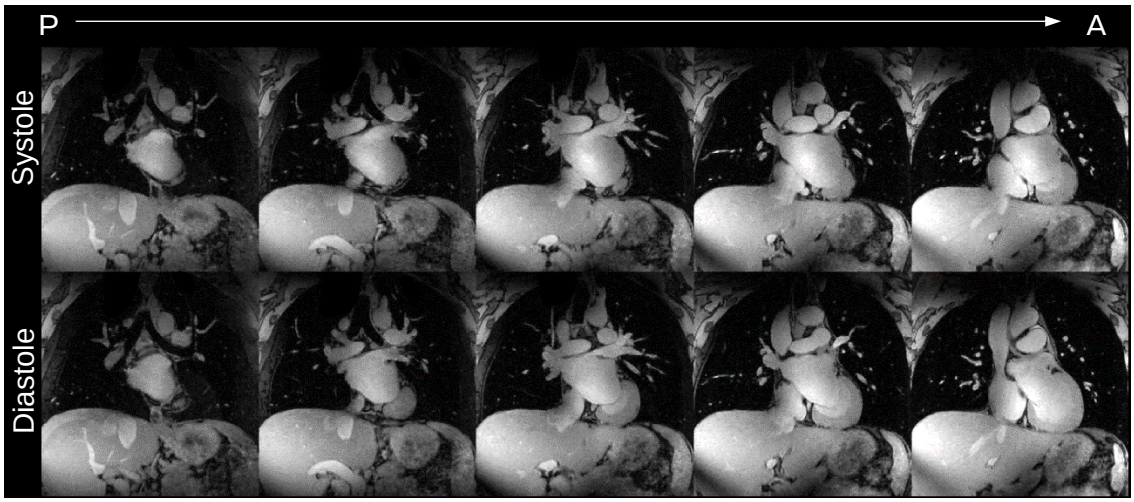


Figure 6.14: Representative coronal images acquired in volunteer 2 using the proposed prospective motion navigation and the 3D CLOCK trajectory with 9 clusters and a targeted undersampling of R = 2. High-resolution (1.0 × 1.0 × 1.0 mm^3) images with a 3D slab thickness of 48 mm are shown at end-expiration during systole and diastole in the upper and lower row, from posterior (left) to anterior (right), respectively.



Figure 6.15: Coronal image set acquired in volunteer 3 using the proposed prospective motion navigation and a 3D-CLOCK trajectory with 7 clusters and a targeted undersampling of R = 4. Reconstructed, high-resolution (1.0 × 1.0 × 1.0 mm^3) images with a 3D slab thickness of 42 mm are shown at end-expiration during systole and diastole in the upper and lower row, from posterior (left) to anterior (right), respectively. Residual image artefacts can be observed in all images and are indicated with white arrows.

Transversal images through the atrium are shown in Figure 6.16 during atrial systole and atrial diastole, as acquired on volunteer 2. The atrial wall can be resolved during atrial diastole.

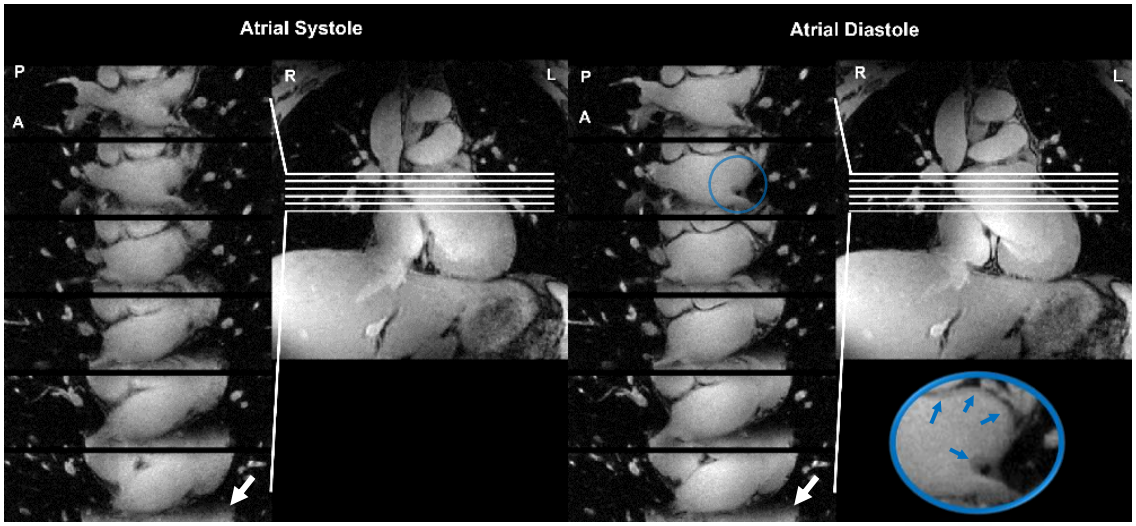


Figure 6.16: Example, transverseal views of the 3D image data set acquired on volunteer 2 through the left atrium are shown at atrial systole (left) and atrial diastole (right). Wrapping artefacts can be observed in inferior slices in the anterior part of the images. The atrial wall can be resolved during atrial diastole (blue arrows) and is shown in a magnified image region.

Representative image intensity line profiles at systole and diastole are shown for volunteer 2 in Figure 6.17.

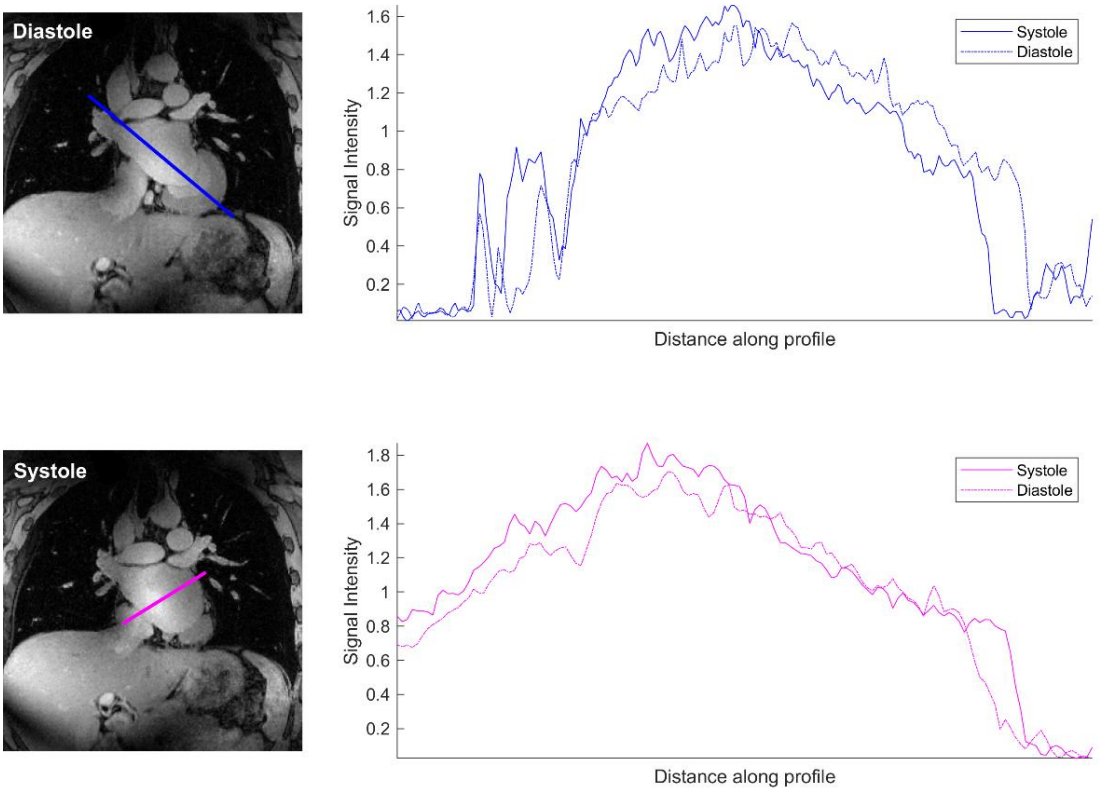


Figure 6.17: Line profiles of example coronal images at end-expiration during diastole and systole, showing good tissue contrast and high SNR in the 3D data set of volunteer 2.

The data set of volunteer 1 - 3 had respiratory drifts of 2.5 mm, 0.8 mm, and 4.3 mm over the duration of the scan that have caused variations in the sampling pattern for different motion states. The resulting *k*-space sampling pattern are shown in the Appendix C in Figure 10.1, Figure 10.2, and Figure 10.5, respectively. Retrospective, respiratory re-binning reduced the sampling efficiency to ~89% for volunteer 2 and to ~93% for volunteer 3, with reduced undersampling rates of $R \approx 2.1$ from previously $R \approx 2.8$ for volunteer 2, and of $R \approx 3.8$ from previously $R \approx 4.1$ at end-expiration (see Figure 10.3 and Figure

10.5 in Appendix C, respectively). No retrospective re-binning was necessary for volunteer 1.

2D cine GRE images, acquired on volunteer 3, were reconstructed with an additional respiratory dimension. Example cine images are shown in Figure 6.18. Blurring at end-inspiration can be observed with an undersampling factor of $R \approx 6$ for those motion states. Retrospective re-binning of end-inspiration motion states reduced the sampling efficiency to ~82% (see Figure 10.6 in Appendix C). The data from all motion states were used for image reconstruction.

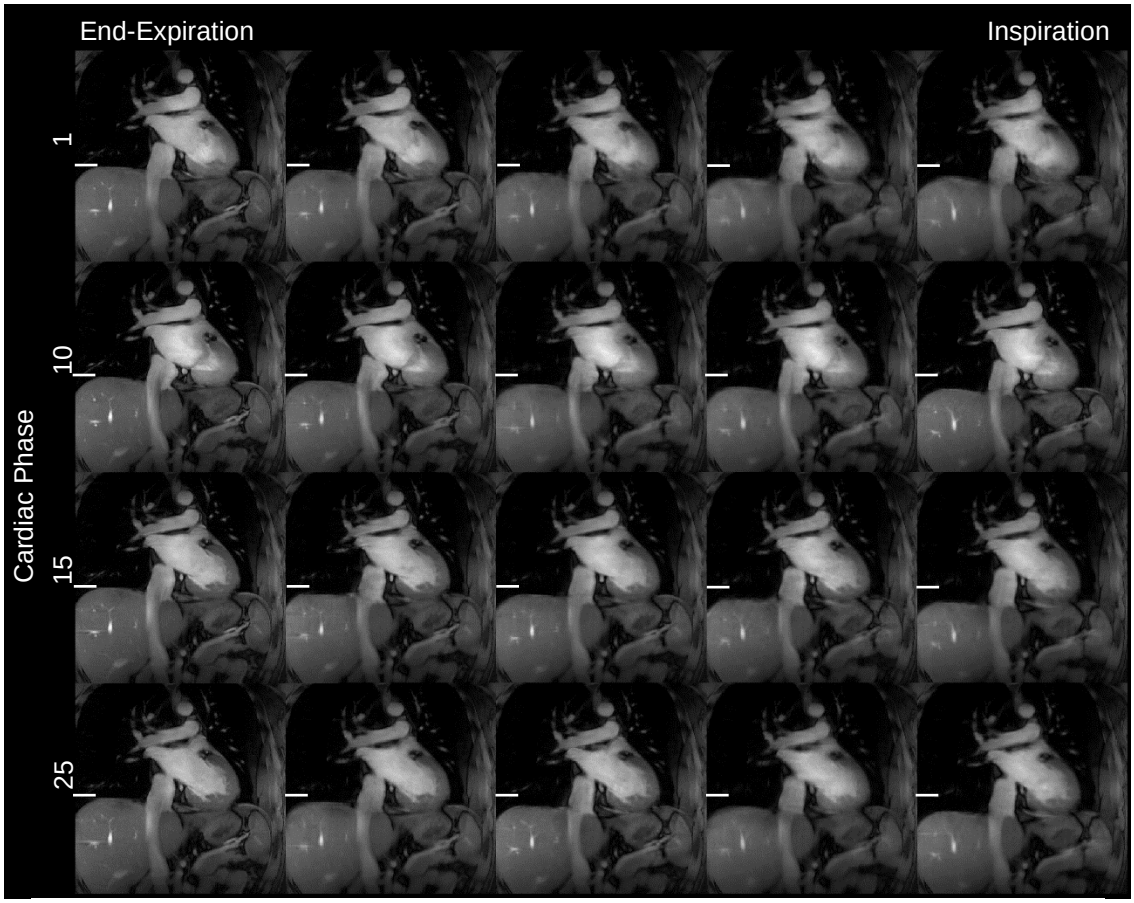


Figure 6.18: Respiratory and cardiac resolved 2D cine images from volunteer 3. High-resolution (1.1 × 1.1 × 3 mm^3) images at end-expiration were reconstructed with high quality, whereas residual blurring can be observed for inspiration motion states. White bars mark the diaphragm end-expiration position

6.5 Discussion and Conclusion

This work evaluated a wide range of physiological motion signals and their influence on different, clustered Cartesian *k*-space trajectories to develop a novel *k*-space trajectory for 3D, high-resolution cardiac imaging during free breathing.

Motion Simulation and k-Space Patterns

The simulations highlighted the strong influence of the respiratory pattern and cardiac variations on free breathing image acquisitions and the need for motion robust *k*-space sampling strategies. The simulations of the proposed clustered random trajectories and the comparison to spiral-like acquisition have shown that the prospectively navigated image acquisition is highly efficient and acquires *k*-space pattern with higher incoherence and better side-lobe-to-peak ratio than in ungated approaches that use retrospective data ordering and uniformly weighted *k*-space pattern. The number of clusters used in the sampling trajectory had only little effect on the median incoherence and side-lobe-to-peak ratios. The preservation of the centre *k*-space calibration region was highly effective for most motion states. However, the simulations as well as image experiments have shown that in highly undersampled motion states, i.e. during end-inspiration, the incoherence and random sampling of the centre region decreases when a higher number of clusters is used. This effect is driven by the fact that higher clustered trajectories have fewer samples per cluster and thus less flexibility in the trade-off between the prioritisation of the calibration region and uniform *k*-space sampling. Therefore, a high ratio R_{cluster} is preferable when all respiratory motion states will be reconstructed.

The simulations carried out in this work have further confirmed that underlying variable-density weighted *k*-space pattern are advantageous and can improve the incoherence measures and the expected reconstruction quality of spiral-like trajectories, as proposed by Cheng et al. for VD-RAD [171] and recently implemented for CASPR by Bustin et al. [187] and Correia et al. [174].

The phantom measurements have shown that additional *k*-space segmentation, i.e. clustering, can significantly reduce image artefacts that are caused by eddy currents. A restriction to a maximum transverse distance of 106 *k*-space phase encoding lines was sufficient. No further improvement in RMSE was found for a larger number of clusters when compared to images acquired with a linear trajectory (see Figure 6.12). Potentially, the centric view ordering of the cluster in the 2D *k*-space trajectory has leveraged the advantage of a further reduction in traverse distances for each cluster by enforcing bigger changes between consecutive clusters. This may have led to a re-introduction of eddy current artefacts. However, for 2D CLOCK acquisition, a linear ordering of clusters and a minimal number of clusters is preferable.

3D High-Resolution Cardiac CINE Framework

The proposed 3D **cl**ustered, random **o**rdered **C**artesian ***k***-space (CLOCK) trajectory combines the advantages of Cartesian *k*-space sampling and the high flexibility of radial or spiral-like trajectories for retrospective adjustments. The motion resolved approach and the multidimensional compressed sensing reconstruction enabled a high image resolution (1 mm isotropic) with high temporal resolution (~ 35-40 ms per cardiac phase). No further cooperation was required from the volunteer other than generally lying still.

Image quality was degraded for volunteer 3, using a higher target undersampling factor *R* and fewer clusters. The large FOV, necessary to capture the entire atrium, has reduced the contrast between the myocardium and an increasingly saturated blood pool.

The 3D thin-slab data sets for volunteer 1 and volunteer 2 enabled high quality cine image reconstruction and a good, myocardial tissue contrast at end-expiration. The high resolution, good tissue contrast and high SNR led to an identification of the atrial wall, which could be used to measure its thickness and investigate the influence atrial arrhythmias, e.g. atrial fibrillation in future work. High-resolution, 3D images of the whole heart, however, would require higher undersampling factors to keep the image acquisition within in a clinically feasable scan time.

Efficiency and Flexibility

The prospective, ECG-free, navigator-free acquisition is highly efficient by sampling individual and randomly arranged *k*-space patterns according to each motion state, without the need for additional hardware to monitor the physiological motion. The resulting random measurements in the time domains (cardiac and respiratory domain) enabled retrospective reordering of data with only little loss of sampling efficiency. This would allow for higher undersampling factors than tested in this work, because of an increased sampling incoherence in the additional cardiac/respiratory dimensional space.

The simulations have confirmed the high flexibility in re-binning end-inspiration bins using CLOCK trajectories, CASPR-Tiger, and the prospective and random

ordered adaptation (CASPR-pro) by containing a sampling efficiency of >90% (see Figure 6.19).

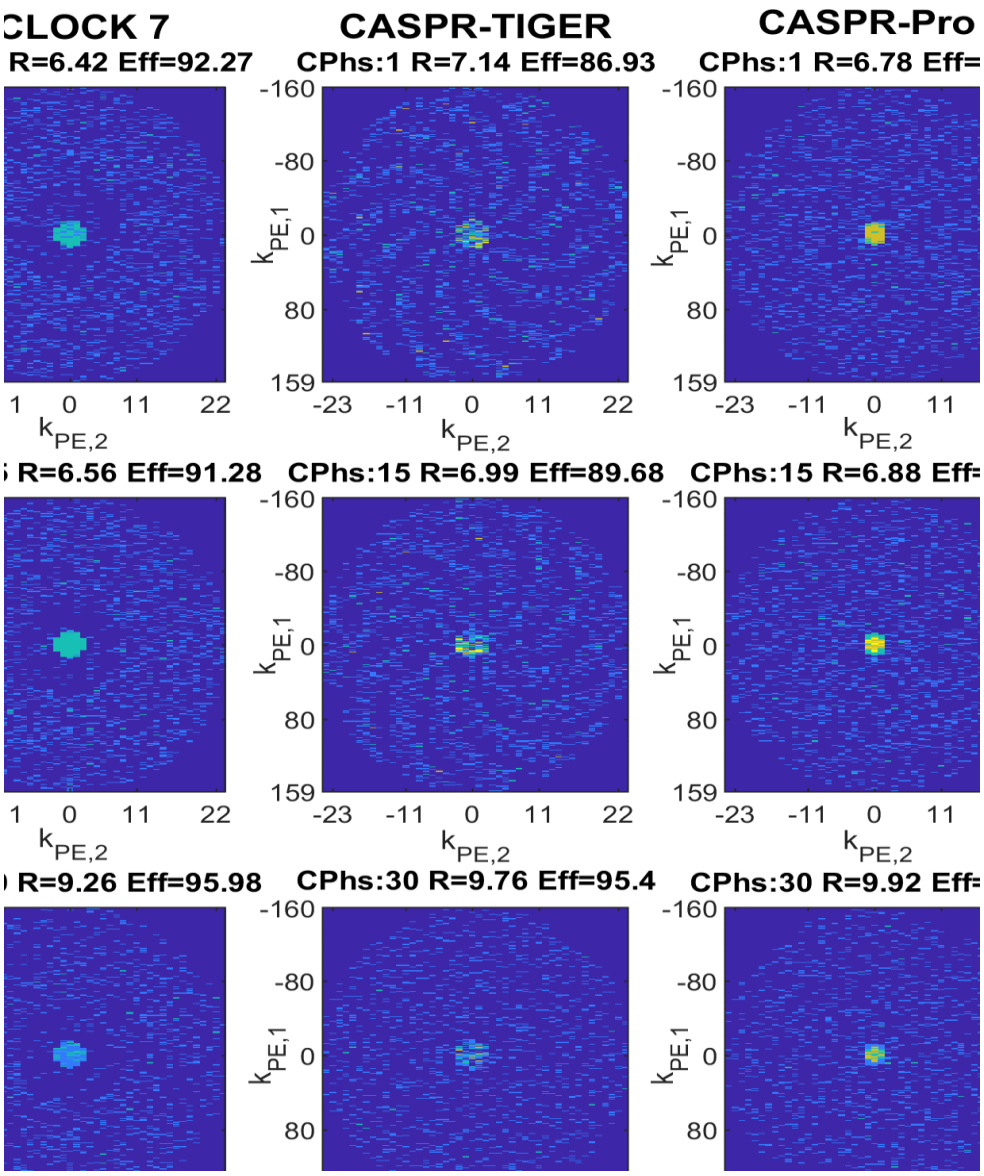


Figure 6.19: Retrospective, respiratory re-binning of two end-inspiration respiratory bins. Simulated 3D *k*-space pattern (320x44 phase encoding lines) are shown for different cardiac phases (CPhs) using a CLOCK trajectory with 7 clusters, CASPR-Tiger, and a CASPR-Pro trajectory.

For acquired image data, however, changes in end-expiration position, as observed in volunteer 2 and volunteer 3 (see Figure 10.1 and Figure 10.5 in Appendix C), limit the flexibility to recover all motion states with a uniformly

sampled *k*-space. Changes in end-expiration position that were close to the edge of an respiratory bin (volunteer 2) or had a magnitude in the scale of the bin size (volunteer 3) have introduced new motion states throughout the scan that were left out during the acquisition of previous cluster of *k*-space and consequently missed those *k*-space lines and led to holes. Fewer clusters, adaptive respiratory bin edges, or larger respiratory bin sizes could minimise these effects and would increase the flexibility in retrospective re-binning and/or correction of respiratory drifts. Multiple rotations of the CLOCK trajectory, i.e. multiple visits of each cluster, could also increase the robustness towards respiratory drifts or sudden motion changes during the scan. Nevertheless, retrospective respiratory re-binning in volunteer 2 and volunteer 3 was still highly efficient in *k*-space sampling (>90% efficiency) for all cardiac phases at end-expiration.

Compared to continuously running acquisition schemes, which use radial [30], [180], spiral [188] or spiral-like trajectories [113], [171], [179] with golden-angle view ordering, the CLOCK *k*-space trajectories cannot be used for a completely arbitrary reconstruction and resorting of *k*-space data, as proposed by Cheng et al. [179] to reconstruct cardiac cines, contrast enhancement scans, and 4D flow images from a single data acquisition. However, it is well suited for all cardiac triggered, clinically used image acquisitions and has a superior efficiency in *k*-space sampling when compared to radial, spiral or spiral-like trajectories with golden-angle view ordering.

6.6 Summary

The work in this chapter has presented a prospectively navigated Cartesian *k*-space trajectory with restricted random sampling for high-resolution, undersampled 3D cardiac cine during free breathing. Simulations have compared the sampling efficiency, reconstruction ability for compressed sensing, and the flexibility for retrospective binning of the proposed sampling trajectory to a free-running spiral-like trajectory with tiny golden-angle view ordering and a herein presented adaptation for prospective gating.

High quality, 3D thin-slab atrial images were reconstructed on two out of three healthy volunteers with a high sampling efficiency and good flexibility for retrospective motion adaptation, whilst minimising eddy-current and cardiac-respiratory induced image artefacts. No external devices (e.g. ECG, respiratory bellows) were required.

CHAPTER 7
SUMMARY AND RECOMMENDATIONS

7.1 Summary of Contributions

This thesis has presented new methods for cardiac and respiratory motion estimation to acquire high-resolution cardiac images at 7T MRI. The proposed methods are independent of the electrical activity of the heart and have the potential to replace the ECG as a gating device in cardiac MRI at ultrahigh magnetic field strengths. The major contributions of this work are summarised below.

A new cardiac gating method, which is based on RF scattering measurements of a pTx MR coil, was presented and evaluated in chapter 4. The cardiac motion signal was calculated from S-matrix measurements with no additional hardware other than the commercially available pTx system of the MRI scanner. No skin contact or patient preparation was required. In comparison to ECG, the cardiac motion signal is derived directly from the heart motion rather than from the electrical activity of the heart.

A new, integrated RF pulse design was developed and presented in chapter 5, which enabled simultaneous S-matrix measurements during MR imaging. A cardiac signal with high SNR was calculated with only a little, extra

SAR burden. The RF pulse design is independent of the *k*-space sampling trajectory and does not alternate or prolong the image sequence timing.

The integrated S-matrix measurements were used to estimate the diaphragm position and the cardiac motion signal during free breathing cardiac imaging in real time on the MR scanner. A prospective, cardiac-respiratory dual-gating framework was implemented and was validated in a group of N = 7 healthy volunteers.

Chapter 6 has presented a **CL**ustered, randomly **O**rdered **C**artesian ***K***-space (CLOCK) sampling trajectory to acquire prospectively gated, high-resolution (1 × 1 × 1 mm^3 isotropic) 3D thin-slab images of the heart. The proposed trajectory has a high sampling efficiency and is designed for accelerated acquisitions and multi-dimensional, physiological motion state image reconstruction using compressed sensing.

7.2 Recommendations for Future Work

There are three main areas for future work; 1) advanced cardiac-respiratory motion modelling and reconstruction methods based on S-matrix measurements, 2) the application in a clinical setting, and 3) S-matrix-based motion correction for MR imaging of other body parts. The more detailed recommendations are given below.

7.2.1 Advanced Cardiac Gating and Motion Adaptation

- **Adaptive (re-)binning of cardiac phases**:

  The S-matrix is a multi-dimensional measurement that reflects the motion of the heart. Compared to the ECG, the S-matrix-based motion signal is non-binary and can be used to identify many different gating features that correlate well with different cardiac phases, as shown in chapter 4. Those features can be used to acquire or resort *k*-space data according to specific cardiac phases that are detected with the motion measurements. For example, *k*-space data can only be acquired when the heart is at rest, with no need for pre-defined and fixed ECG trigger delay window. Additional information about the start of the atrial systole could be used to (re-)sort *k*-space data accordingly and reduce blurring of cardiac phases at end-diastole/early systole that result from physiologically varying heart intervals.

- **(Un-)supervised Machine Learning to identify motion states**:

  Respiratory induced changes of the heart position are not linear. Nehrke et al. [79] have shown that some patients have a strong hysteresis effects

with a non-linear translation of the heart position during expiration. This limits the application of simple respiratory gating on diaphragm positions as they correspond to different heart positions during inspiration and expiration. The S-matrix measurements, consisting of 2×N×N motion signals with N the number of pTx channels, could capture the hysteresis motion of the heart and an unsupervised machine learning method, e.g. *k*-means cluster, could be able to identify the correct heart position during free breathing and sort the data accordingly.

7.2.2 Application in Lower Field Strengths and Patients

- **Application in lower field strengths:**

  The motion estimation methods presented in this thesis were developed and tested at 7T MRI using an 8-channel pTx system. Most MRI scanners in clinical practice, however, have a field strength of 1.5 T or 3.0 T and no parallel transmit capacity. Only some of the modern clinical MRI scanner are equipped with a parallel transmit system consisting of a 2-channel pTx body/volume coil, which could be used to measure motion by monitoring its RF scattering. The application of the presented methods on those systems would allow for a wider clinical application of ECG-free and navigator-free imaging.

  An increased field-of-view, fewer coil array elements, and a lower resonance frequency have the potential to decrease the RF scattering variations that reflect physiological motion. It is expected that a higher RF monitoring power would be needed to achieve a similar cardiac SNR as presented in this work.

- **Application for Arrhythmic Patients:**

  The herein developed framework for S-matrix-based and ECG-free cardiac gating is independent of the electrical activity of the heart. This can be particularly useful for those patients that suffer from irregular electrical patterns of the heart muscle and arrhythmias, which further degenerates the ECG R-wave detection. The direct measurement of heart motion could enable cardiac MRI examinations on those patient that otherwise cannot be scanned effectively. It could also be used to identify and reconstruct or exclude data from abnormal heart cycles and patterns.

7.2.3 Motion Monitoring beyond Cardiac MRI

- **Breath hold monitoring tool**:

  The monitoring of respiratory-induced changes in the S-matrix measurements can be utilised as a tool to assess the compliance of patients to hold their breath during image acquisitions. Such a monitoring tool would not require signal calibration and can be derived directly from the changes in the S-matrix measurements and/or single coil elements.

- **Respiratory motion monitoring in abdominal imaging**:

  Respiration affects the position and the shape of many organs in the abdomen. Predominantly those of the liver and the heart but also from the lungs themselves. As the proposed methods are based on the changes of the conductive tissue distribution in the field-of-view of the RF coil elements, the presented methods could be extended to monitor respiratory-induced motion changes in other organs. This could be used

to respiratory gate abdominal imaging sequences and/or correct for B_0/B_1 field changes.

- **Motion monitoring in the brain:**

  Motion during imaging of the brain is a problem for the daily routine in clinical practice and clinical research. Many methods have been developed to estimate and correct for rigid motion (translation, rotation) and non-rigid motion (cardiac and respiratory pulsation) [189], including optical tracking systems. Functional MRI of the brain is particularly sensitive to small signal changes and physiological noise (cardiac and respiratory pulsation) that degrade functional sensitivity and reduce temporal resolution [190]. The S-matrix measurements could be used to detect motion with no extra costs in time and without image navigators or additional tracking hardware. Preliminary work has shown that S-matrix measurements of an 8Tx/32Rx head coil were able to extract cardiac and respiratory pulsation and to predict head motion in two healthy volunteers at 7T MRI. Those results were presented at the annual meeting of the international society of magnetic resonance in medicine (ISMRM) in 2018 [191]. More work is needed to evaluate the derived physiological motion signals and their potential to correct for physiological noise in functional MRI of the brain.

APPENDIX A

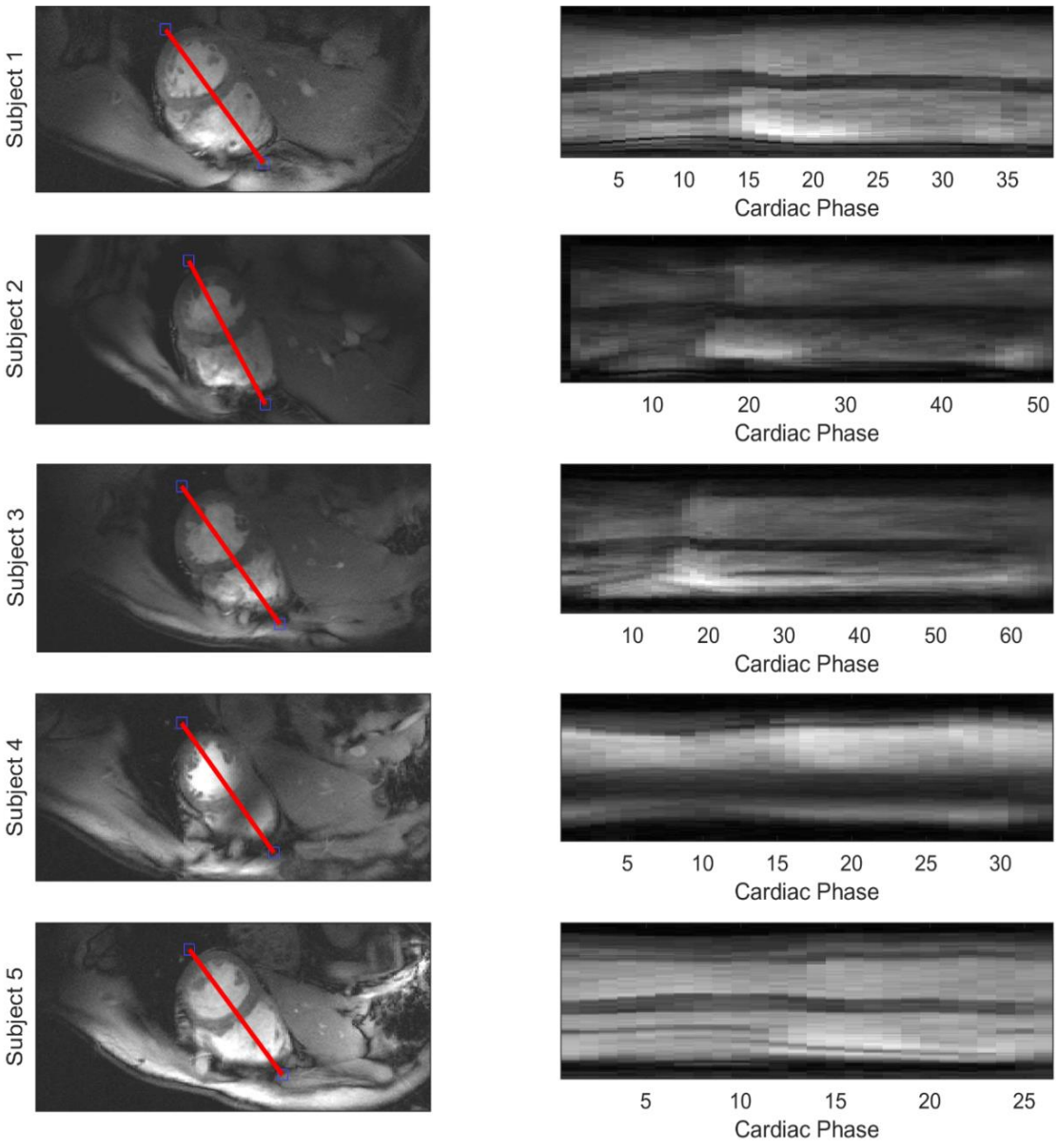


Figure 8.1: Mid-ventricular, short-axis view (diastole) and temporal profiles of all breath hold cine sequences reconstructed using the scattering coefficients, which were measured during transmit RF pulses, are shown. The main peak detection (end-systole) of the proposed method was used for cardiac gating and retrospective re-binning of the *k*-space data.

APPENDIX B

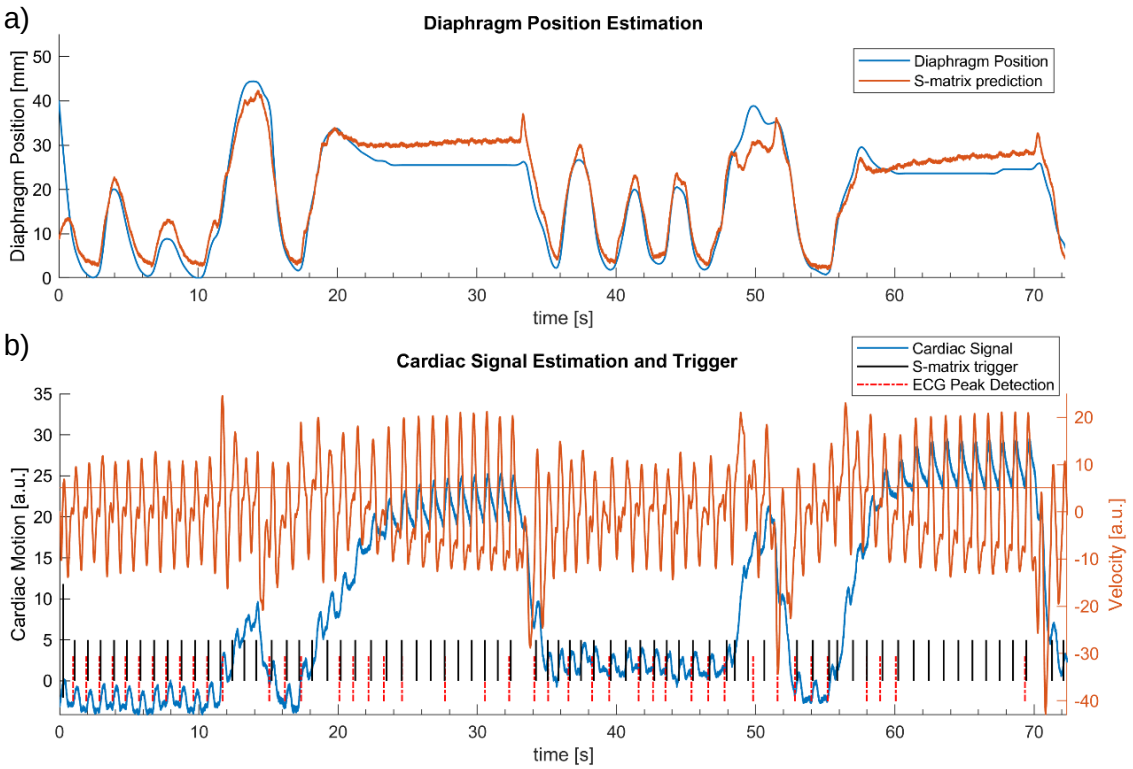


Figure 9.1: Example of strong inspiration/expiration events with two breath holds at end-inspiration. Estimated and extracted diaphragm positions are shown in A). Cardiac signal estimation, S-matrix trigger and ECG peak detection are shown in B). S-matrix trigger were identified at all respiratory positions but during rapid expiration. ECG peak detection was not reliable at end-inspiration and during rapid expiration.

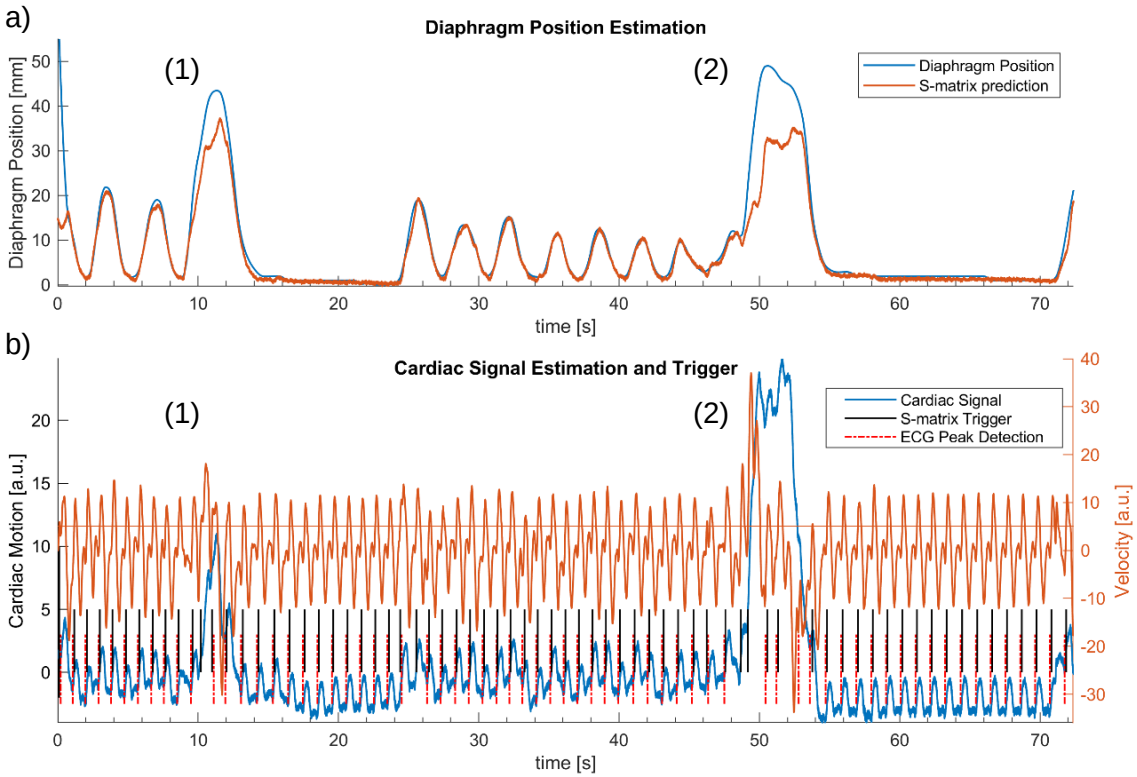


Figure 9.2: Example of two, very strong inhalation events before breath holds at end-expiration. Estimated and extracted diaphragm positions are shown in A). Cardiac signal estimation, S-matrix trigger and ECG peak detection are shown in B). S-matrix trigger were identified correctly during event 1 but unregularly during event 2. The diaphragm position was underestimated for both events.

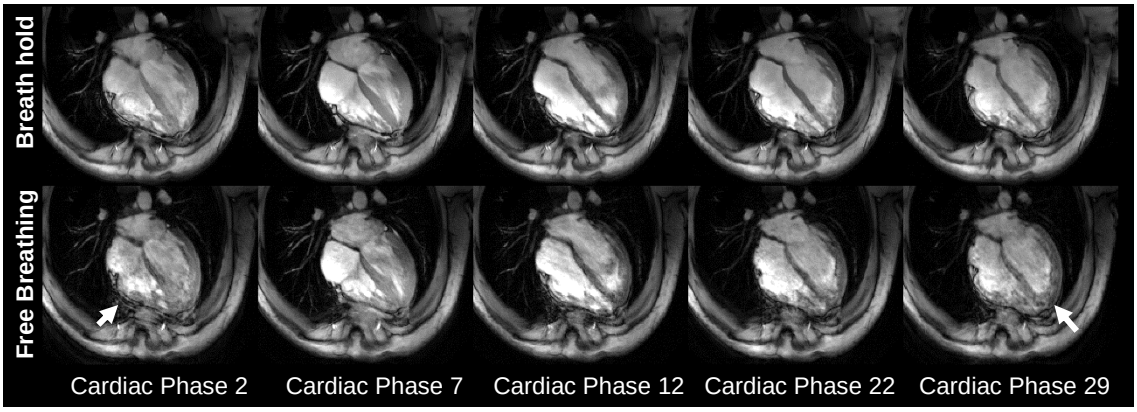


Figure 9.3: Example images in volunteer 1 using the proposed dual respiratory-cardiac S-matrix navigation. Images with a four-chamber view during breath hold and free breathing are shown with five cardiac phases, each capturing a time window of 33 ms of the cardiac cycle. From left to right, the images show early ventricular systole to end-diastole of the cardiac cycle. Blurring can be observed around the apex in free breathing images.

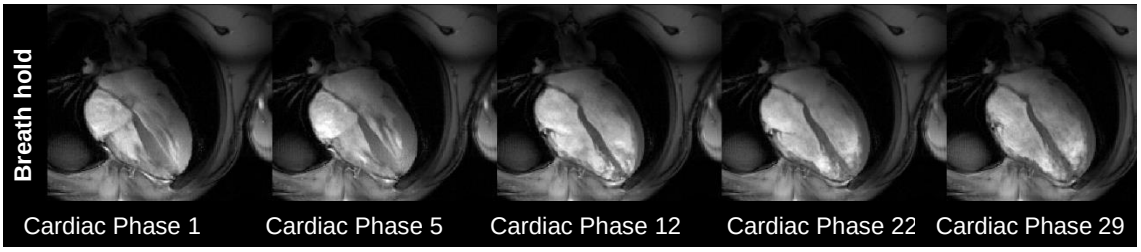


Figure 9.4: Example images of a four-chamber view in volunteer 2 using the prospective cardiac S-matrix triggering during breath hold. Five cardiac phases, each capturing a time window of 33 ms of the cardiac cycle, are shown from systole (left) to end-diastole (right).

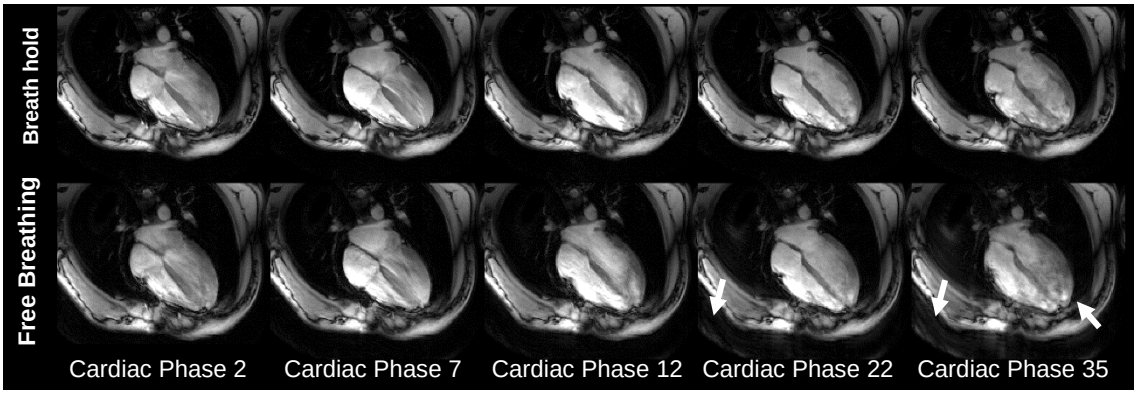


Figure 9.5: Example images in volunteer 3 using the proposed dual respiratory-cardiac S-matrix navigation. Images with a four-chamber view during breath hold and free breathing are shown with five cardiac phases, each capturing a time window of 33 ms, from systole (left) to end-diastole (right). Slight blurring and small residual chest movements can be observed at end-diastole in free breathing images.

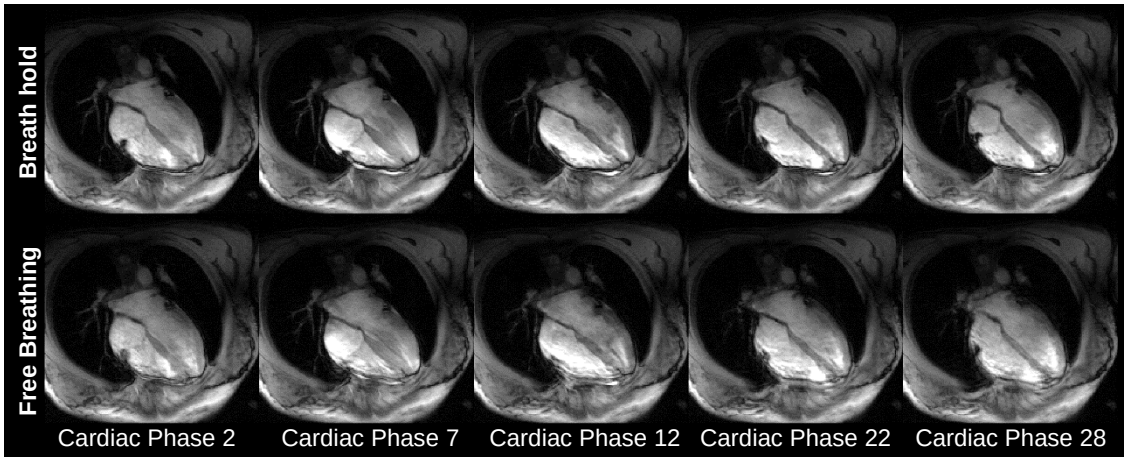


Figure 9.6: Example images in volunteer 4 using the proposed dual respiratory-cardiac S-matrix navigation. Images with a four-chamber view during breath hold and free breathing are shown with five cardiac phases, each capturing a time window of 33 ms of the cardiac cycle. From left to right, the images show early ventricular systole to end-diastole of the cardiac cycle.

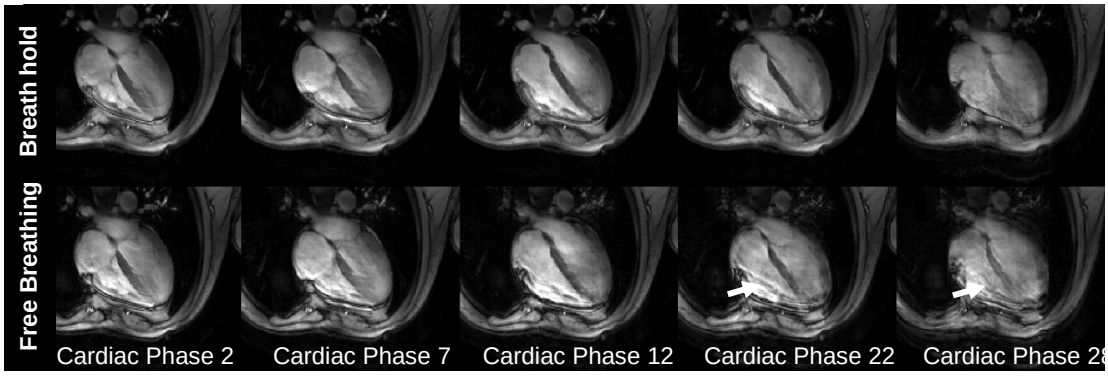


Figure 9.7: Example images in volunteer 5 using the proposed dual respiratory-cardiac S-matrix navigation. Images with a four-chamber view during breath hold and free breathing are shown with five cardiac phases, each capturing a time window of 33 ms of the cardiac cycle, are shown from systole (left) to end-diastole (right). Residual chest movements can be observed at end-diastole in free breathing images.

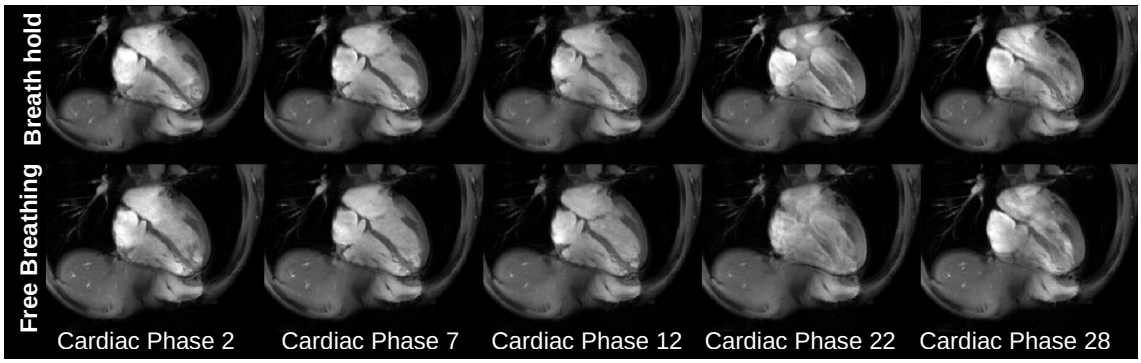


Figure 9.8: Example images in volunteer 6 using the proposed dual respiratory-cardiac S-matrix navigation. Images with a four-chamber view during breath hold and free breathing are shown with five cardiac phases, each capturing a time window of 33 ms of the cardiac cycle. From left to right, the images show early ventricular systole to end-diastole of the cardiac cycle.

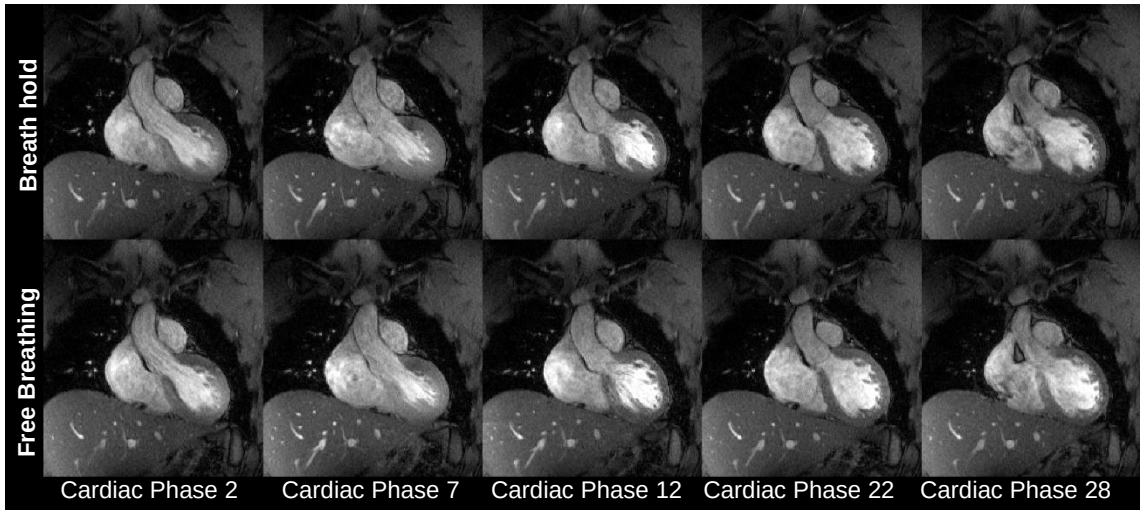


Figure 9.9: Example images in volunteer 7 using the proposed dual respiratory-cardiac S-matrix navigation. Images in sagittal view during breath hold and free breathing are shown with five cardiac phases, each capturing a time window of 33 ms of the cardiac cycle. From left to right, the images show early ventricular systole to end-diastole of the cardiac cycle. No residual respiratory artefacts are present in the images.

APPENDIX C

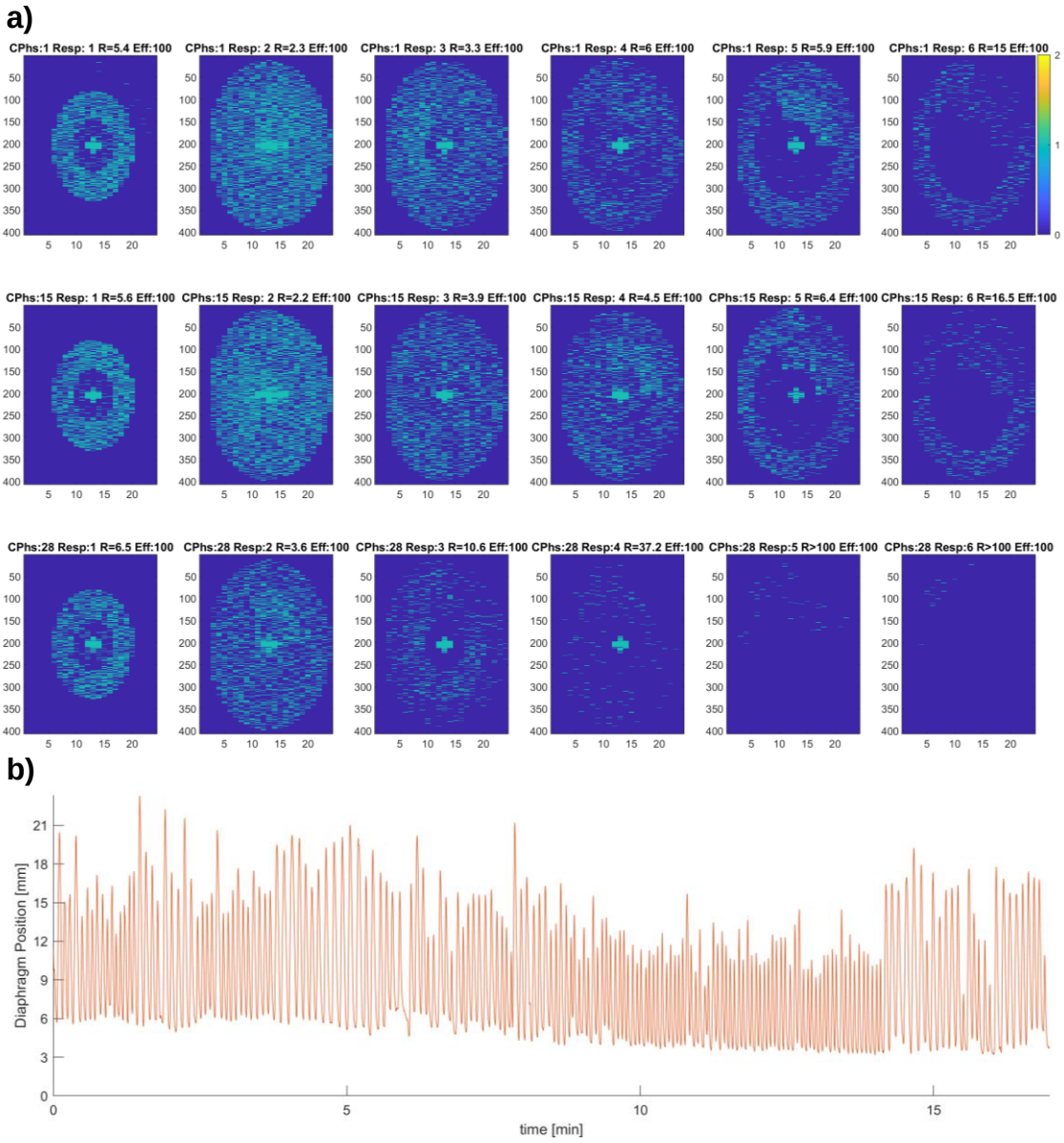


Figure 9.1: A) Prospectively gated and acquired 3D *k*-space sampling pattern for different motion states in volunteer 1. B) Estimated diaphragm position with a drift in end-expiration position and changing respiratory amplitudes.

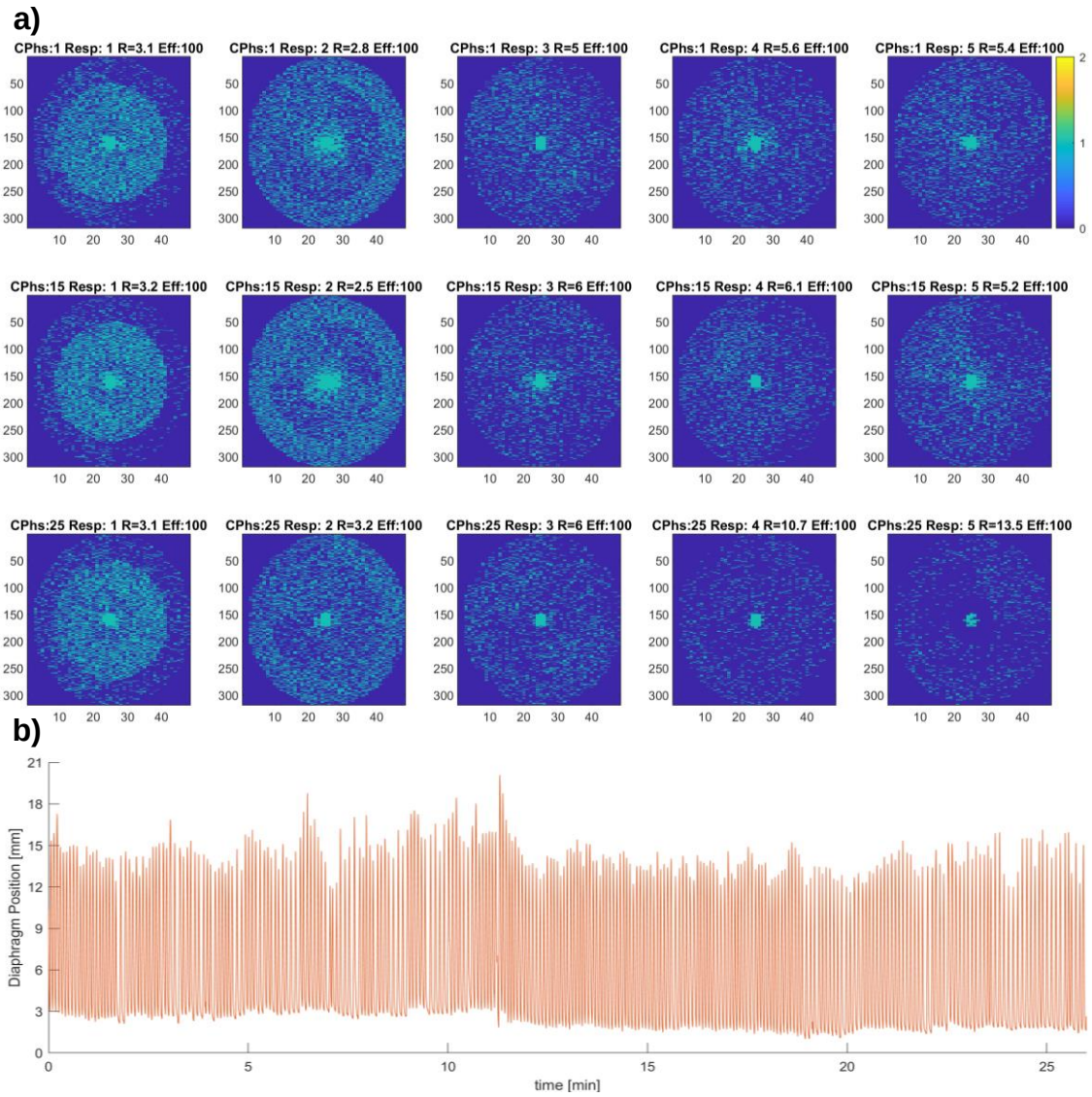


Figure 10.2: A) Prospectively acquired 3D *k*-space sampling pattern for different motion states in volunteer 2. B) Estimated diaphragm position with the slight respiratory drift during the scan.

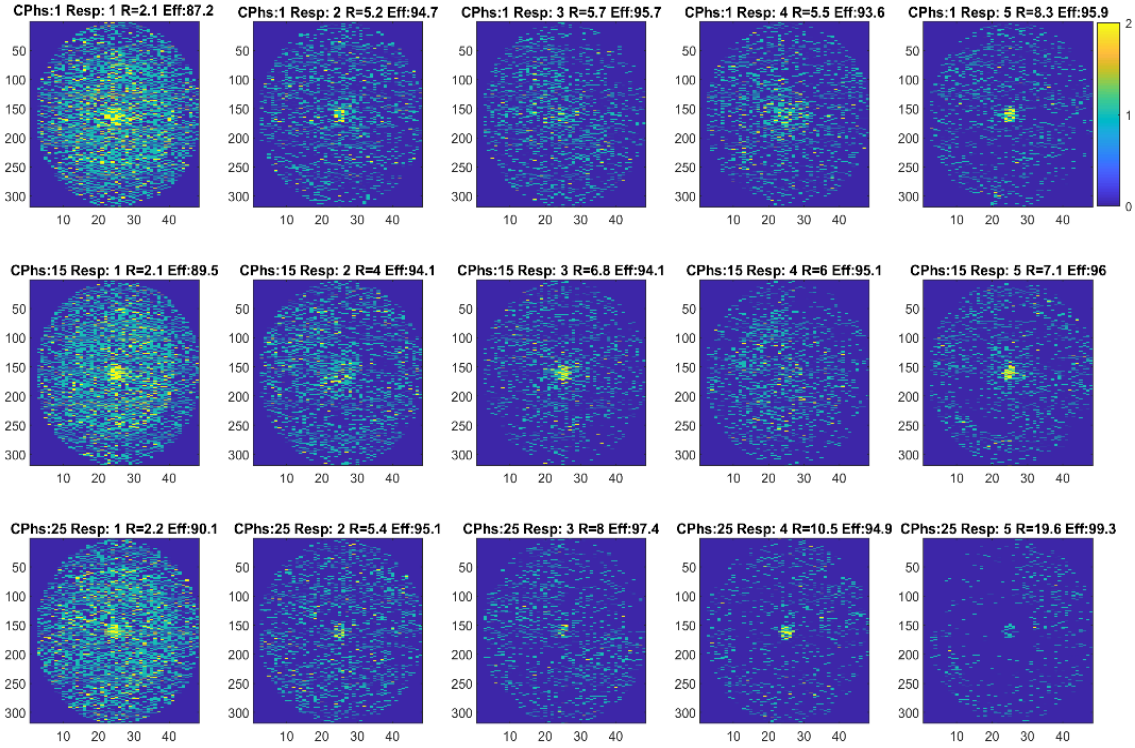


Figure 10.3: Retrospectively, respiratory re-binning and the resulting 3D *k*-space pattern for different motion states from volunteer 2. Random undersampling in the temporal dimension allows for retrospective binning with only little reduction in sampling efficiency.

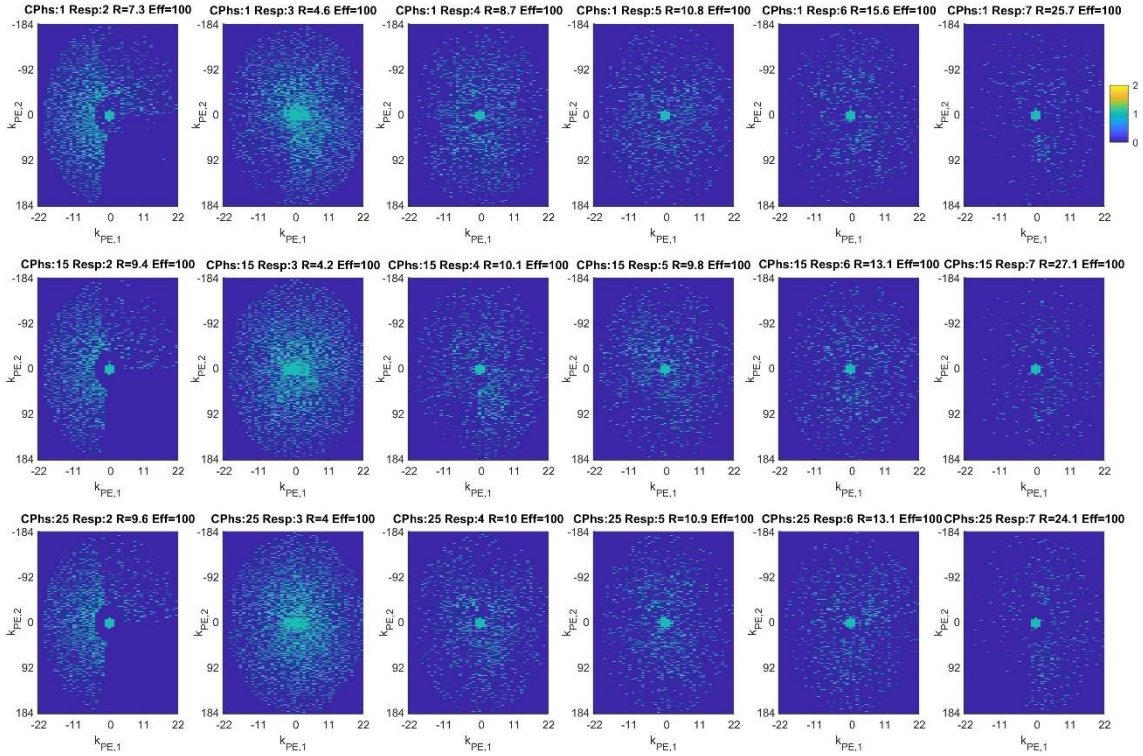


Figure 10.4: Prospectively gated and acquired 3D *k*-space sampling pattern for different motion states in volunteer 3.

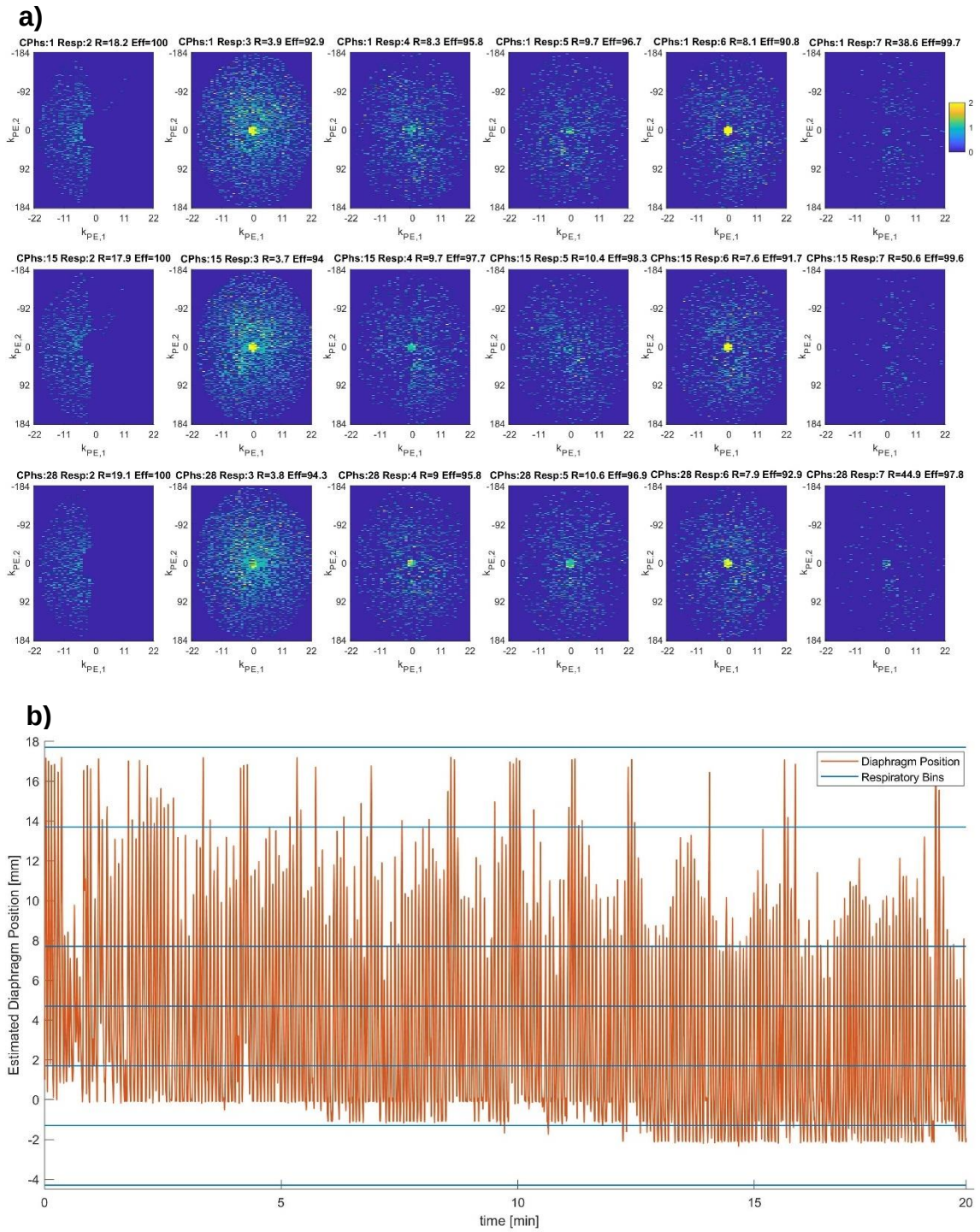


Figure 10.5: A) 3D *k*-space pattern for different cardiac (CPhs) and respiratory (Resp) motion states, acquired on volunteer 3, after retrospective re-binning in the respiratory domain. The end-expiration bin was re-positioned and two end-inspiration bins were joint. Strong inspiration data was rejected. B) The estimated diaphragm position shows strong drifts at end-expiration positions and changing breathing patterns. Retrospectively adjusted respiratory bin edges are indicated with blue lines.

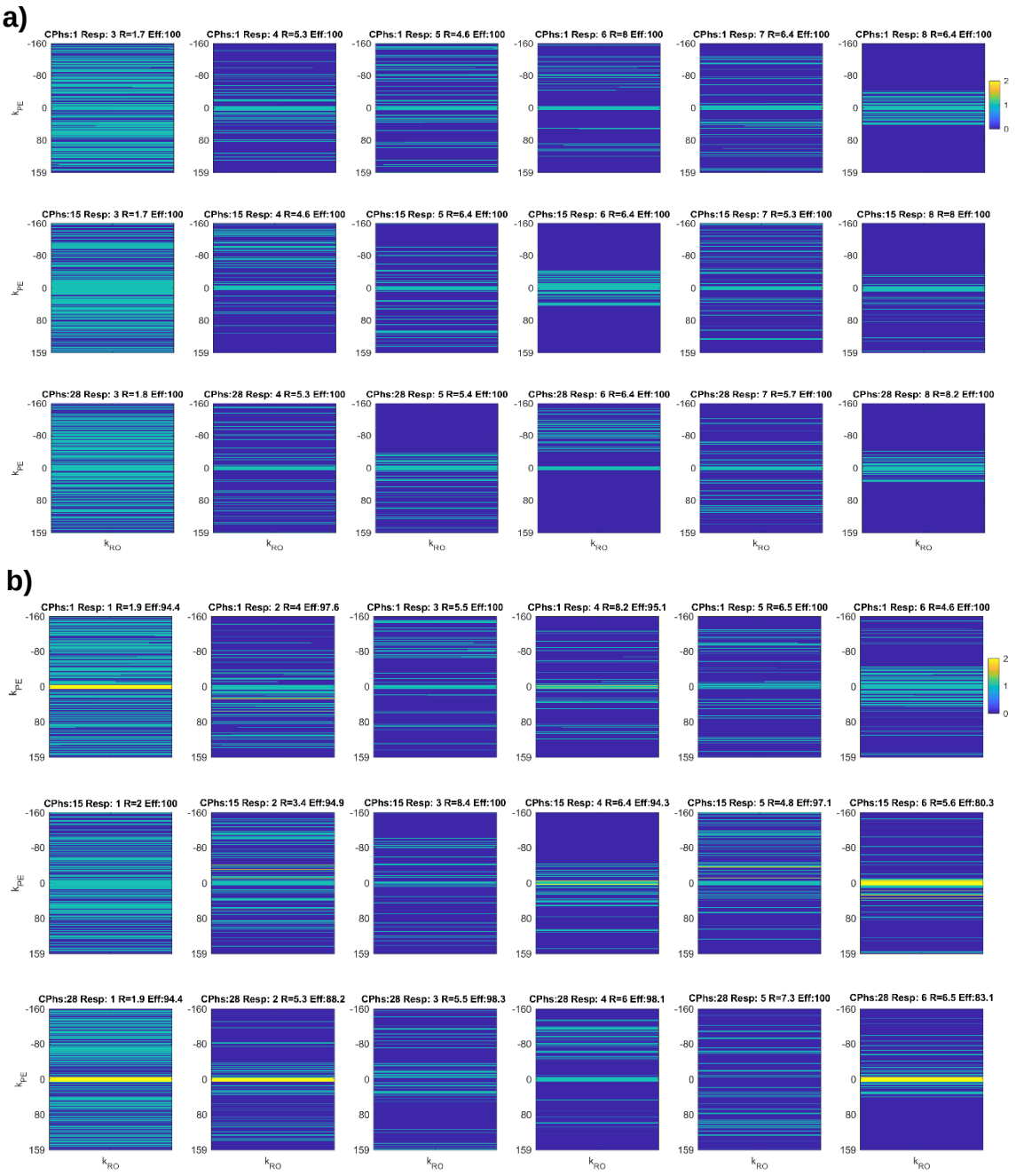


Figure 10.6: 2D *k*-space sampling pattern for different cardiac (CPhs) and respiratory (Resp) motion states obtained from volunteer 3. A) After prospective image acquisition and B) after retrospective, respiratory re-binning to decrease the undersampling factor R for end-inspiration bins. A high *k*-space sampling efficiency can be sustained.

Bibliography

[1] M. N. Levy, A. J. Pappano, and R. M. Berne, *Cardiovascular Physiology*, 9th ed. Mosby Elsevier, 2007.

[2] D. J. Pennell, “Cardiovascular magnetic resonance imaging,” *Circulation*, vol. 121, pp. 692–705, 2010.

[3] R. Y. Kwong, *Cardiovascular magnetic resonance imaging*. Totowa, N.J.: Humana, 2008.

[4] M. Salerno *et al.*, “Recent advances in cardiovascular magnetic resonance: Techniques and applications,” *Circ Cardiovasc. Imaging*, vol. 10, no. 6, p. e003951, 2017.

[5] Y. Wang, S. J. Riederer, and R. L. Ehman, “Respiratory Motion of the Heart: Kinematics and the Implications for the Spatial Resolution in Coronary Imaging,” *Magn. Reson. Med.*, vol. 33, no. 5, pp. 713–719, 1995.

[6] Y. Wang, R. C. Grimm, P. J. Rossman, J. P. Debbins, S. J. Riederer, and R. L. Ehman, “3D Coronary MR Angiography in Multiple Breath-Holds Using a Respiratory Feedback Monitor,” vol. 34, pp. 11–16, 1995.

[7] A. C. Larson, R. D. White, G. Laub, E. R. McVeigh, D. Li, and O. P. Simonetti, “Self-Gated Cardiac Cine MRI,” *Magn. Reson. Med.*, vol. 51, no. 1, pp. 93–102, 2004.

[8] T. A. Spraggins, “Wireless retrospective gating: Application to cine cardiac imaging,” *Magn. Reson. Imaging*, vol. 8, no. 6, pp. 675–681, 1990.

[9] M. Pallack, H. Hricak, C. Higgins, M. McNamara, and R. Ehman, “Magnetic resonance imaging with respiratory gating: techniques and advantages,” *Am. J. Roentgenol.*, vol. 143, no. 6, pp. 1175–1182, 1984.

[10] C. Santelli *et al.*, “Respiratory bellows revisited for motion compensation: Preliminary experience for cardiovascular MR,” *Magn. Reson. Med.*, vol. 65, no. 4, pp. 1098–1103, 2011.

[11] J. R. Keltner, M. S. Roos, P. R. Brakeman, and T. F. Budinger, “Magnetohydrodynamics of blood flow,” *Magn. Reson. Med.*, vol. 16, no. 1, pp. 139–49, 1990.

[12] S. E. Fischer, S. A. Wickline, and C. H. Lorenz, “Novel real-time R-wave detection algorithm based on the vectorcardiogram for accurate gated magnetic resonance acquisitions,” *Magn. Reson. Med.*, vol. 42, no. 2, pp. 361–370, 1999.

[13] J. J. Suttie *et al.*, “7 Tesla (T) human cardiovascular magnetic resonance imaging using FLASH and SSFP to assess cardiac function: Validation against 1.5T and 3T,” *NMR Biomed.*, vol. 25, no. 1, pp. 27–34, 2012.

[14] F. Bloch, “Nuclear induction,” *Phys. Rev.*, vol. 70, no. 7, pp. 460–474, 1946.

[15] E. M. Purcell, H. C. Torrey, and R. V Pound, “Resonance Absorption by Nuclear Magnetic Moments in a Solid,” *Phys. Rev.*, vol. 69, no. 1–2, pp. 37–38, Jan. 1946.

[16] L. G. Hanson, “Is Quantum Mechanics Necessary for Understanding Magnetic Resonance?,” *Concepts Magn. Reson. Part A Bridg. Educ. Res.*, vol. 32, pp. 329–340, 2008.

[17] M. a Bernstein, K. E. King, X. J. Zhou, and W. Fong, *Handbook of MRI Pulse Sequences*, vol. 32, no. 5. 2005.
[18] D. W. McRobbie, E. A. Moore, M. J. Graves, and M. R. Prince, *MRI from picture to proton*, 2nd ed. Cambridge: Cambridge University Press, 2007.
[19] R. H. Hashemi, W. G. Bradley, and C. J. Lisanti, *MRI : the basics*, Third. Philadelphia, PA: Wolters Kluwer : Lippincott Williams & Wilkins, 2010.
[20] M. H. Levitt, *Spin dynamics : basics of nuclear magnetic resonance*, Second. Chichester, England : John Wiley & Sons, Ltd, 2008.
[21] E. L. Hahn, “Spin Echoes,” *Phys. Today*, vol. 3, no. 12, p. 21, 1950.
[22] P. van der Meulen, J. P. Groen, and J. J. M. Cuppen, “Very fast MR imaging by field echoes and small angle excitation,” *Magn. Reson. Imaging*, vol. 3, no. 3, pp. 297–299, 1985.
[23] “Translate 7T research power into clinical care,” *Magnetom Terra brochure*, 2019. [Online]. Available: https://www.siemens-healthineers.com/en-uk/magnetic-resonance-imaging/7t-mri-scanner/magnetom-terra/technical-details. [Accessed: 10-Sep-2019].
[24] V. M. Runge, M. L. Wood, D. M. Kaufman, and M. S. Silver, “MR imaging section profile optimization: improved contrast and detection of lesions.,” *Radiology*, vol. 167, no. 3, pp. 831–834, 1988.
[25] Lauterbur, P.C., “Image formation by induced local interactions: examples employing nuclear magnetic resonance,” *Nature*, vol. 242, no. 5394, pp. 190–191, 1973.
[26] P. Mansfield, “Multi-planar image formation using NMR spin echoes,” *J. Phys. C Solid State Phys.*, vol. 10, no. 3, pp. L55–L58, 1977.
[27] K. K. Kwong *et al.*, “Dynamic magnetic resonance imaging of human brain activity during primary sensory stimulation,” vol. 89, no. 12, pp. 5675–5679, 1992.
[28] G. H. Glover and J. M. Pauly, “Projection Reconstruction Techniques for Reduction of Motion Effects in MRI,” *Magn. Reson. Med.*, vol. 28, no. 2, pp. 275–289, 1992.
[29] D. C. Peters *et al.*, “Undersampled projection reconstruction applied to MR angiography,” *Magn. Reson. Med.*, vol. 43, no. 1, pp. 91–101, 2000.
[30] L. Feng, L. Axel, H. Chandarana, K. T. Block, D. K. Sodickson, and R. Otazo, “XD-GRASP: Golden-Angle Radial MRI with Reconstruction of Extra Motion-State Dimensions Using Compressed Sensing,” *Magn Reson Med*, vol. 75, no. 2, pp. 775–788, 2016.
[31] A. Macovski, C. H. Meyerm, B. S. Hu, and D. G. Nishimura, “Fast spiral coronary artery imaging,” *Magn. Reson. Med.*, vol. 28, pp. 202–213, 1992.
[32] J. I. Jackson, C. H. Meyer, D. G. Nishimura, and A. Macovski, “Selection of a convolution function for Fourier inversion using gridding (computerised tomography application),” *IEEE Trans. Med. Imaging*, vol. 10, no. 3, pp. 473–478, 1991.
[33] C. Y. Jong, S. Tak, Y. Han, and W. P. Hyun, “Projection reconstruction MR imaging using FOCUSS,” *Magn. Reson. Med.*, vol. 57, no. 4, pp. 764–775, 2007.
[34] J. T. Vaughan *et al.*, “7T vs. 4T: RF power, homogeneity, and signal-to-noise comparison in head images,” *Magn. Reson. Med.*, vol. 46, no. 1, pp. 24–30, 2001.

[35] C. J. Snyder *et al.*, “Initial results of cardiac imaging at 7 Tesla,” *Magn. Reson. Med.*, vol. 61, no. 3, pp. 517–524, 2009.
[36] T. Niendorf, D. K. Sodickson, G. A. Krombach, and J. Schulz-menger, “Toward cardiovascular MRI at 7 T: clinical needs, technical solutions and research promises,” *Eur Radiol*, vol. 20, no. 12, pp. 2806–2816, 2011.
[37] T. Niendorf *et al.*, “W(h)ither human cardiac and body magnetic resonance at ultrahigh fields? Technical advances, practical considerations, applications, and clinical opportunities,” *NMR Biomed.*, vol. I, no. October 2014, 2015.
[38] Q. X. Yang *et al.*, “Analysis of wave behavior in lossy dielectric samples at high field,” *Magn. Reson. Med.*, vol. 47, no. 5, pp. 982–989, 2002.
[39] P. A. Bottomley and E. R. Andrew, “RF magnetic field penetration, phase shift and power dissipation in biological tissue: Implications for NMR imaging,” *Phys. Med. Biol.*, vol. 23, no. 4, pp. 630–643, 1978.
[40] U. Katscher, P. Börnert, C. Leussler, and J. S. Van den Brink, “Transmit SENSE,” *Magn. Reson. Med.*, vol. 49, no. 1, pp. 144–150, 2003.
[41] L. Wald and E. Adalsteinsson, “Parallel transmit technology for high field MRI,” *MAGNETOM Flash*, pp. 124–135, 2009.
[42] G. J. Metzger, C. Snyder, C. Akgun, T. Vaughan, K. Ugurbil, and P. F. Van De Moortele, “Local B1+ shimming for prostate imaging with transceiver arrays at 7T based on subject-dependent transmit phase measurements,” *Magn. Reson. Med.*, vol. 59, no. 2, pp. 396–409, 2008.
[43] F. Badalà, K. Nouri-mahdavi, and D. A. Raoof, “Maximum Efficiency RF Shimming: Theory and Initial Application for Hip Imaging at 7 Tesla,” *Magn. Reson. Imaging*, vol. 144, no. 5, pp. 724–732, 2008.
[44] S. Saekho, C. Y. Yip, D. C. Noll, F. E. Boada, and V. A. Stenger, “Fast-kz three-dimensional tailored radiofrequency pulse for reduced B1 inhomogeneity,” *Magn. Reson. Med.*, vol. 55, no. 4, pp. 719–724, 2006.
[45] S. Schmitter *et al.*, “Cardiac imaging at 7 Tesla: Single- and two-spoke radiofrequency pulse design with 16-channel parallel excitation,” *Magn. Reson. Med.*, vol. 70, no. 5, pp. 1210–1219, Nov. 2013.
[46] M. A. Cloos *et al.*, “K T-points: Short three-dimensional tailored RF pulses for flip-angle homogenization over an extended volume,” *Magn. Reson. Med.*, vol. 67, no. 1, pp. 72–80, 2012.
[47] P. B. Roemer, W. A. Edelstein, C. E. Hayes, S. P. Souza, and O. M. Mueller, “The NMR phased array,” *Magn. Reson. Med.*, vol. 16, no. 2, pp. 192–225, 1990.
[48] J. T. Vaughan *et al.*, “Efficient high-frequency body coil for high-field MRI,” *Magn. Reson. Med.*, vol. 52, no. 4, pp. 851–859, 2004.
[49] J. T. Vaughan, H. P. Hetherington, J. Otu, J. W. Pan, and G. M. Pohost, “High Frequency Volume Coils for Clinical NMR Imaging and Spectroscopy,” *Spectroscopy*, pp. 206–218, 1994.
[50] X. Zhang, K. Ugurbil, and W. Chen, “Microstrip RF Surface Coil Design for Extremely High-Field MRI and Spectroscopy,” vol. 450, pp. 443–450, 2001.
[51] J. T. Vaughan *et al.*, “Detunable transverse electromagnetic (TEM) volume coil for high-field NMR,” *Magn. Reson. Med.*, vol. 47, no. 5, pp. 990–1000, 2002.

[52] A. J. E. Raaijmakers *et al.*, “Design of a radiative surface coil array element at 7 T: The single-side adapted dipole antenna,” *Magn. Reson. Med.*, vol. 66, no. 5, pp. 1488–1497, 2011.
[53] A. J. E. Raaijmakers *et al.*, “The fractionated dipole antenna: A new antenna for body imaging at 7 Tesla,” *Magn. Reson. Med.*, vol. 75, no. 3, pp. 1366–1374, 2016.
[54] D. Klomp *et al.*, “Radio-Frequency coil design: Practical design of RF transmit and receiver coil arrays,” *ESMRMB 2011 Congr.*, 2011.
[55] B. Keil and L. L. Wald, “Massively parallel MRI detector arrays,” *J. Magn. Reson.*, 2013.
[56] K. Kurokawa, “Power Waves and the Scattering Matrix,” *IEEE Trans. Microw. Theory Tech.*, vol. 13, no. 2, pp. 194–202, 1965.
[57] A. T. Hess, E. M. Tunnicliffe, C. T. Rodgers, and M. D. Robson, “Diaphragm position can be accurately estimated from the scattering of a parallel transmit RF coil at 7 T,” *Magn. Reson. Med.*, vol. 00, 2017.
[58] A. Andreychenko *et al.*, “Thermal noise variance of a receive radiofrequency coil as a respiratory motion sensor.,” *Magn. Reson. Med.*, vol. 00, pp. 1–8, 2016.
[59] A. Kuehne *et al.*, “Power balance and loss mechanism analysis in RF transmit coil arrays,” *Magn. Reson. Med.*, vol. 74, no. 4, pp. 1165–1176, 2015.
[60] D. M. Pozar, *Microwave engineering*, 4th ed. Hoboken, N.J.: Wiley, 2012.
[61] J. E. Hall and A. C. Guyton, *Guyton and Hall Textbook of Medical Physiology*, 12th ed. Saunders/Elsevier, 2011.
[62] S. Hirschfeld, R. Meyer, J. Korfhagen, S. Kaplan, and J. Liebman, “The isovolumic contraction time of the left ventricle. An echographic study.,” *Circulation*, vol. 54, no. 5, pp. 751–756, Nov. 1976.
[63] H. C. BAZETT, “An Analysis of the Time-Relations of Electrocardiograms.,” *Ann. Noninvasive Electrocardiol.*, vol. 2, no. 2, pp. 177–194, 1997.
[64] M. S. Ruttley, D. F. Adams, P. F. Cohn, and H. L. Abrams, “Shape and volume changes during ‘isovolumetric relaxation’ in normal and synergic ventricles,” *Circulation*, vol. 50, no. 2, pp. 306–316, 1974.
[65] B. F. M. Groedel and M. A. X. Miller, “By FRANZ M. GROEDEL and MAX MILLER. The electrocardiogram is generally used for the,” *Cardiologia*, vol. 1, no. 2, pp. 1–10, 1951.
[66] W. R. Milnor, *Cardiovascular physiology*. New York : Oxford University Press, 1990.
[67] R. E. Klabunde, *Cardiovascular physiology concepts*, 2nd ed. Philadelphia, Pa. : Wolters Kluwer/Lippincott Williams & Wilkins, 2012.
[68] WHO, “Global Health estimates 2016: Disease burden by cause, age, sex, by country, and by region, 2000-2016.,” Geneva, 2018.
[69] W. B. KANNEL, T. R. DAWBER, A. KAGAN, N. REVOTSKIE, and I. I. I. STOKES JOSEPH, “Factors of Risk in the Development of Coronary Heart Disease—Six-Year Follow-up Experience: The Framingham Study,” *Ann. Intern. Med.*, vol. 55, no. 1, pp. 33–50, 1961.

[70] D. L. Mann, D. P. Zipes, P. Libby, R. O. Bonow, and E. Braunwald, *Braunwald's heart disease : a textbook of cardiovascular medicine*, Tenth. Philadelphia: Saunders, 2015.
[71] N. Herring, D. J. Paterson, J. R. Levick, and (J. Rodney), *Levick's introduction to cardiovascular physiology*, 6th ed. Oxford: Taylore & Francis Group, LLC, 2018.
[72] F. Yasuma and J. Hayano, "Respiratory Sinus Arrhythmia - Why Does the Heartbeat Synchronize With Respiratory Rhythm," *Chest*, vol. 125, no. 2, pp. 683–690, 2004.
[73] R. J. Simpson, W. E. Cascio, P. J. Schreiner, R. S. Crow, P. M. Rautaharju, and G. Heiss, "Prevalence of premature ventricular contractions in a population of African American and white men and women: The Atherosclerosis Risk In Communities (ARIC) study," *Am. Heart J.*, vol. 143, no. 3, pp. 535–540, 2002.
[74] W. B. Kannel and E. J. Benjamin, "Current perceptions of the epidemiology of atrial fibrillation," *Cardiol. Clin.*, vol. 27, no. 1, pp. 13–vii, Feb. 2009.
[75] T. Niendorf *et al.*, "High Field Cardiac Magnetic Resonance Imaging: A Case for Ultrahigh Field Cardiac Magnetic Resonance," *Controv. IMAGING*, vol. 10(6), pp. 1–13, 2017.
[76] A. D. Scott, J. Keegan, and D. N. Firmin, "Motion in Cardiovascular MR Imaging," *Radiology*, vol. 250, no. 2, pp. 331–351, 2009.
[77] K. McLeish, D. L. G. Hill, D. Atkinson, J. M. Blackall, and R. Razavi, "A study of the motion and deformation of the heart due to respiration," *IEEE Trans. Med. Imaging*, vol. 21, no. 9, pp. 1142–1150, 2002.
[78] T. D. Nguyen, A. Nuval, S. Mulukutla, and Y. Wang, "Direct monitoring of coronary artery motion with cardiac fat navigator echoes," *Magn. Reson. Med.*, vol. 50, no. 2, pp. 235–241, 2003.
[79] K. Nehrke, P. Börnert, D. Manke, and J. C. Böck, "Free-breathing Cardiac MR Imaging: Study of Implications of Respiratory Motion—Initial Results," *Radiology*, vol. 220, no. 3, pp. 810–815, 2007.
[80] C. Petitjean, N. Rougon, and P. Cluzel, "Assessment of myocardial function: A review of quantification methods and results using tagged MRI," *J. Cardiovasc. Magn. Reson.*, vol. 7, no. 2, pp. 501–516, 2005.
[81] H. Sakuma *et al.*, "Effect of breath holding on blood flow measurement using fast velocity encoded cine MRI," *Magn. Reson. Med.*, vol. 45, no. 2, pp. 346–348, 2001.
[82] A. E. Holland, J. W. Goldfarb, and R. R. Edelman, "Diaphragmatic and cardiac motion during suspended breathing: preliminary experience and implications for breath-hold MR imaging.," *Radiology*, vol. 209, no. 2, pp. 483–489, 2014.
[83] D. J. Atkinson and R. R. Edelman, "Cineangiography of the heart in a single breath hold with a segmented turboFLASH sequence.," *Radiology*, vol. 178, no. 2, pp. 357–360, 1991.
[84] C. B. Higgins, W. Holt, P. Pflugfelder, and U. Sechtem, "Functional evaluation of the heart with magnetic resonance imaging," *Magn. Reson. Med.*, vol. 6, no. 2, pp. 121–139, 1988.

[85] U. Sechtem, P. W. Pflugfelder, R. G. Gould, M. M. Cassidy, and C. B. Higgins, “Measurement of right and left ventricular volumes in healthy individuals with cine MR imaging.,” *Radiology*, vol. 163, no. 3, pp. 697–702, Jun. 1987.

[86] P. Lanzer, C. Barta, E. H. Botvinick, H. U. Wiesendanger, G. Modin, and C. B. Higgins, “ECG-synchronized cardiac MR imaging: method and evaluation.,” *Radiology*, vol. 155, no. 3, pp. 681–686, 1985.

[87] F. ERNEST, “An Accurate, Clinically Practical System For Spatial Vectorcardiography,” *Circulation*, vol. 13, no. 5, pp. 737–749, May 1956.

[88] F. S. E. Chia JM Wickline SA, Lorenz CH, “Performance of QRS detection for cardiac magnetic resonance imaging with a novel vector cardiographic triggering method,” *J Magn Reson Imaging*, vol. 688, pp. 678–688, 2000.

[89] T. Niendorf, L. Winter, and T. Frauenrath, “Electrocardiogram in an MRI Environment: Clinical Needs, Practical Considerations, Safety Implications, Technical Solutions and Future Directions,” in *Advances in Electrocardiograms - Methods and Analysis*, 2012, pp. 309–324.

[90] T. Togawa, O. Okai, and M. Oshima, “Observation of blood flow E.M.F. in externally applied strong magnetic field by surface electrodes,” *Med. Biol. Eng.*, vol. 5, no. 2, pp. 169–170, 1967.

[91] V. Martin, A. Drochon, O. Fokapu, and J.-F. Gerbeau, “MagnetoHemoDynamics Effect on Electrocardiograms,” in *Functional Imaging and Modeling of the Heart*, 2011, pp. 325–332.

[92] J. Krug and G. Rose, “Magnetohydrodynamic distortions of the ECG in different MR scanner configurations,” *Comput. Cardiol. (2010).*, pp. 769–772, 2011.

[93] D. Stäb, J. Roessler, K. O. Brien, C. Hamilton-craig, and M. Barth, “ECG Triggering in Ultra-High Field Cardiovascular MRI,” *Tomography*, vol. 2, no. 3, pp. 167–174, 2016.

[94] J. Krug, G. Rose, D. Stucht, G. Clifford, and J. Oster, “Limitations of VCG based gating methods in ultra high field cardiac MRI,” *J. Cardiovasc. Magn. Reson.*, vol. 15, no. Suppl 1, p. W19, 2013.

[95] Y. Wang, R. C. Grimm, J. P. Felmlee, S. J. Riederer, and R. L. Ehman, “Algorithms for extracting motion information from navigator echoes,” *Magn. Reson. Med.*, vol. 36, no. 1, pp. 117–123, 1996.

[96] J. Y. Cheng, M. T. Alley, C. H. Cunningham, S. S. Vasanawala, J. M. Pauly, and M. Lustig, “Nonrigid motion correction in 3D using autofocusing withlocalized linear translations,” *Magn. Reson. Med.*, vol. 68, no. 6, pp. 1785–1797, 2012.

[97] T. S. Sachs, C. H. Meyer, B. S. Hu, J. Kohli, D. G. Nishimura, and A. Macovski, “Real-time motion detection in spiral MRI using navigators,” *Magn. Reson. Med.*, vol. 32, no. 5, pp. 639–645, 1994.

[98] R. L. Ehman and J. P. Felmlee, “Adaptive technique for high-definition MR imaging of moving structures.,” *Radiology*, vol. 173, no. 1, pp. 255–263, 1989.

[99] W. S. Kim, C. W. Mun, D. J. Kim, and Z. H. Cho, “Extraction of cardiac and respiratory motion cycles by use of projection data and its applications to nmr imaging,” *Magn. Reson. Med.*, vol. 13, no. 1, pp. 25–37, Jan. 1990.

[100] M. E. Crowe *et al.*, “Automated rectilinear self-gated cardiac cine imaging,” *Magn. Reson. Med.*, vol. 52, no. 4, pp. 782–788, 2004.
[101] A. C. S. Brau and J. H. Brittain, “Generalized self-navigated motion detection technique: Preliminary investigation in abdominal imaging,” *Magn. Reson. Med.*, vol. 55, no. 2, pp. 263–270, 2006.
[102] M. Lustig, C. H. Cunningham, E. Daniyalzade, and J. M. Pauly, “Butterfly: a self navigating Cartesian trajectory.,” *Proc. Jt. Annu. Meet. ISMRM-ESMRMB*, vol. 15, no. d, p. 865, 2007.
[103] D. Rigie *et al.*, “Cardiorespiratory motion-tracking via self-refocused rosette navigators,” *Magn. Reson. Med.*, no. April 2018, pp. 1–12, 2018.
[104] P. Lai, X. Bi, R. Jerecic, and D. Li, “A respiratory self-gating technique with 3D-translation compensation for free-breathing whole-heart coronary MRA,” *Magn. Reson. Med.*, vol. 62, no. 3, pp. 731–738, 2009.
[105] Y. Liu, S. J. Riederer, P. J. Rossman, R. C. Grimm, J. P. Debbins, and R. L. Ehman, “Monitoring, Feedback, and Triggering System for Reproducible Breath-Hold MR Imaging,” *Magn. Reson. Med.*, no. 30, pp. 507–511, 1993.
[106] Y. Wang, P. J. Rossman, R. C. Grimm, S. J. Riederer, and R. L. Ehman, “Navigator-echo-based real-time respiratory gating and triggering for reduction of respiration effects in three-dimensional coronary MR angiography.,” *Card. Radiol.*, vol. 198, no. 1, pp. 55–60, 1996.
[107] M. V. McConnell *et al.*, “Prospective adaptive navigator correction for breath-hold MR coronary angiography,” *Magn. Reson. Med.*, vol. 37, no. 1, pp. 148–152, 1997.
[108] M. Buehrer, J. Curcic, P. Boesiger, and S. Kozerke, “Prospective self-gating for simultaneous compensation of cardiac and respiratory motion,” *Magn. Reson. Med.*, vol. 60, no. 3, pp. 683–690, 2008.
[109] J. Liu, P. Spincemaille, N. C. F. Codella, T. D. Nguyen, M. R. Prince, and Y. Wang, “Respiratory and cardiac self-gated free-breathing cardiac CINE imaging with multiecho 3D hybrid radial SSFP acquisition,” *Magn. Reson. Med.*, vol. 63, no. 5, pp. 1230–1237, 2010.
[110] L. Feng *et al.*, “Golden-angle radial sparse parallel MRI: combination of compressed sensing, parallel imaging, and golden-angle radial sampling for fast and flexible dynamic volumetric MRI,” *Magn. Reson. Med.*, vol. 72, no. 3, pp. 707–717, 2014.
[111] L. Feng, L. Axel, H. Chandarana, K. T. Block, D. K. Sodickson, and R. Otazo, “XD-GRASP: Golden-angle radial MRI with reconstruction of extra motion-state dimensions using compressed sensing,” *Magn. Reson. Med.*, vol. 75, no. 2, pp. 775–788, 2016.
[112] C. Prieto *et al.*, “Highly efficient respiratory motion compensated free-breathing coronary MRA using golden-step Cartesian acquisition,” *J. Magn. Reson. Imaging*, vol. 41, no. 3, pp. 738–746, 2015.
[113] M. Usman, B. Ruijsink, M. S. Nazir, G. Cruz, and C. Prieto, “Free breathing whole-heart 3D CINE MRI with self-gated Cartesian trajectory,” *Magn. Reson. Imaging*, vol. 38, pp. 129–137, 2017.
[114] C. Stehning, P. Börnert, K. Nehrke, H. Eggers, and M. Stuber, “Free-breathing whole-heart coronary MRA with 3D radial SSFP and self-navigated image reconstruction,” *Magn. Reson. Med.*, vol. 54, no. 2, pp. 476–480, 2005.

[115] P. Hu *et al.*, “Motion correction using coil arrays (MOCCA) for free-breathing cardiac cine MRI,” *Magn. Reson. Med.*, vol. 66, no. 2, pp. 467–475, 2011.
[116] T. Zhang, J. Y. Cheng, Y. Chen, D. G. Nishimura, J. M. Pauly, and S. S. Vasanawala, “Robust self-navigated body MRI using dense coil arrays,” *Magn. Reson. Med.*, vol. 76, no. Note, pp. 197–205, 2016.
[117] F. Han, Z. Zhou, M. Cao, Y. Yang, K. Sheng, and P. Hu, “Respiratory motion-resolved, self-gated 4D-MRI using rotating cartesian k-space (ROCK):,” *Med. Phys.*, vol. 44, no. 4, pp. 1359–1368, 2017.
[118] N. White *et al.*, “PROMO: Real-time prospective motion correction in MRI using image-based tracking,” *Magn. Reson. Med.*, vol. 63, no. 1, pp. 91–105, 2010.
[119] A. T. Hess, M. Dylan Tisdall, O. C. Andronesi, E. M. Meintjes, and A. J. W. Van Der Kouwe, “Real-time motion and B 0 corrected single voxel spectroscopy using volumetric navigators,” *Magn. Reson. Med.*, vol. 66, no. 2, pp. 314–323, 2011.
[120] M. Henningsson, P. Koken, C. Stehning, R. Razavi, C. Prieto, and R. M. Botnar, “Whole-heart coronary MR angiography with 2D self-navigated image reconstruction,” *Magn. Reson. Med.*, vol. 67, no. 2, pp. 437–445, 2012.
[121] M. Henningsson, J. Smink, R. Razavi, and R. M. Botnar, “Prospective respiratory motion correction for coronary MR angiography using a 2D image navigator,” *Magn. Reson. Med.*, vol. 69, no. 2, pp. 486–494, 2013.
[122] M. Usman *et al.*, “Motion corrected compressed sensing for free-breathing dynamic cardiac MRI,” *Magn. Reson. Med.*, vol. 70, no. 2, pp. 504–516, 2013.
[123] M. A. Bush and O. P. Simonetti, “Patient specific prospective respiratory motion correction for efficient , free - breathing cardiovascular MRI,” no. August 2018, pp. 1–13, 2019.
[124] H. H. Wu, P. T. Gurney, B. S. Hu, D. G. Nishimura, and M. V. McConnell, “Free-breathing multiphase whole-heart coronary MR angiography using image-based navigators and three-dimensional cones imaging,” *Magn. Reson. Med.*, vol. 69, no. 4, pp. 1083–1093, 2013.
[125] A. C. Larson *et al.*, “Preliminary investigation of respiratory self-gating for free-breathing segmented cine MRI,” *Magn. Reson. Med.*, vol. 53, no. 1, pp. 159–168, 2005.
[126] K. Kawaji *et al.*, “Direct coronary motion extraction from a 2D fat image navigator for prospectively gated coronary MR angiography,” *Magn. Reson. Med.*, vol. 71, no. 2, pp. 599–607, 2014.
[127] S. Denslow and D. S. Buckles, “Pulse oximetry-gated acquisition of cardiac MR images in patients with congenital cardiac abnormalities,” *Am. J. Roentgenol.*, vol. 160, no. 4, pp. 831–833, 1993.
[128] P. Lanzer *et al.*, “Cardiac imaging using gated magnetic resonance.,” *Radiology*, vol. 150, no. 1, pp. 121–127, 1984.
[129] J. M. Rubin, J. Brian Fowlkes, M. R. Prince, R. T. Rhee, and T. L. Chenevert, “Doppler US gating of cardiac MR imaging,” *Acad. Radiol.*, vol. 7, no. 12, pp. 1116–1122, 2000.

[130] T. Frauenrath *et al.*, “Acoustic cardiac triggering: a practical solution for synchronization and gating of cardiovascular magnetic resonance at 7 Tesla.,” *J. Cardiovasc. Magn. Reson.*, vol. 12, no. 1, p. 67, 2010.
[131] A. Andreychenko, B. Denis de Senneville, R. J. M. Navest, R. H. N. Tijssen, J. J. W. Lagendijk, and C. A. T. van den Berg, “Respiratory motion model based on the noise covariance matrix of a receive array,” *Magn. Reson. Med.*, vol. 79, no. 3, pp. 1730–1735, 2018.
[132] P. Speier, M. Fenchel, and R. Rehner, “PT-Nav: a novel respiratory navigation method for continuous acquisitions based on modulation of a pilot tone in the MR-receiver,” in *ESMRMB, 129:97–98*, 2015.
[133] L. Schroeder *et al.*, “A Novel Method for Contact-Free Cardiac Synchronization Using the Pilot Tone Navigator,” in *Proc. Intl. Soc. Mag. Reson. Med. 24*, 2016, p. 0410.
[134] L. Schroeder, J. Wetzl, A. Maier, R. R. Rehner, M. Fenchel, and P. Speier, “Two-Dimensional Respiratory-Motion Characterization for Continuous MR Measurements Using Pilot Tone Navigation,” in *Proc. Intl. Soc. Mag. Reson. Med. 24*, 2016, p. 3103.
[135] J. Wetzl *et al.*, “Feasibility Study: Free-Breathing 3-D CINE Imaging with Respiratory Gating Based on Pilot Tone Navigation,” *ISMRM 24th Annu. Meet. Exhib.*, p. 2613, 2016.
[136] D. Buikman, T. Helzel, and P. Roeschmann, “The rf coil as a sensitive motion detector for magnetic resonance imaging,” *Magn. Reson. Imaging*, vol. 6, no. 3, pp. 281–289, 1988.
[137] I. Graesslin *et al.*, “Advancements in Contact-free Respiration Monitoring using RF Pick-up coils,” *Proc. 18th Sci. Meet. Int. Soc. Magn. Reson. Med.*, no. 2, p. 3045, 2010.
[138] I. Graesslin *et al.*, “An Alternative Concept for Non-Sequence Interfering, Contact-free Respiration Monitoring,” *Proc. 17th Sci. Meet. Int. Soc. Magn. Reson. Med.*, vol. 17, p. 753, 2009.
[139] V. Martin, A. Drochon, O. Fokapu, and J. F. Gerbeau, “Magnetohemodynamics effect on electrocardiograms,” *Lect. Notes Comput. Sci. (including Subser. Lect. Notes Artif. Intell. Lect. Notes Bioinformatics)*, vol. 6666 LNCS, pp. 325–332, 2011.
[140] S. H. F. Jaeschke, M. D. Robson, and A. T. Hess, “Cardiac gating using scattering of an 8-channel parallel transmit coil at 7T,” *Magn. Reson. Med.*, vol. 80, no. 2, pp. 633–640, 2018.
[141] J. T. V. Snyder, “Remotely Adjustable Reactive and Resistive Electrical Elements and Method,” 2004.
[142] J. I. M. X. Ji, J. B. U. M. Son, and S. D. Rane, “PULSAR : A MATLAB Toolbox for Parallel Magnetic Resonance Imaging Using Array Coils and Multiple Channel Receivers,” vol. 1, pp. 24–36.
[143] S. Butterworth, “On the theory of filter amplifiers,” in *Experimental Wireless and the Wireless Engineer*, 1930, pp. 536–541.
[144] A. Hyvärinen, “Fast and Robust Fixed-Point Algorithm for Independent Component Analysis,” *IEEE Trans. Neur. Net.*, vol. 10, no. 3, pp. 626–634, 1999.
[145] H. Gävert, J. Hurri, J. Särelä, and A. Hyvärinen, “FastICA package for MATLAB.” Helsinki University of Technology, Helsinki, 2005.

[146] D. B. Percival and A. T. Walden, *Wavelet methods for time series analysis*. Cambridge University Press, 2000.
[147] A. Savitzky and M. J. E. Golay, “Smoothing and Differentiation of Data by Simplified Least Squares Procedures,” *Anal. Chem.*, vol. 36, no. 8, pp. 1627–1639, 1964.
[148] J. L. Caplin, W. D. Flatman, L. Dyke, M. Wiseman, and D. S. Dymond, “Influence of respiratory variations on right ventricular function,” *Br Hear. J*, vol. 62, no. April, pp. 253–259, 1989.
[149] F. Padormo *et al.*, “Large dynamic range relative B1+ mapping,” *Magn. Reson. Med.*, vol. 76, no. 2, pp. 490–499, 2016.
[150] S. H. F. Jaeschke, M. D. Robson, and A. T. Hess, “Scattering matrix imaging pulse design for real-time respiration and cardiac motion monitoring,” *Magn. Reson. Med.*, vol. 82, no. 6, pp. 2169–2177, 2019.
[151] N. S. Higano *et al.*, “Retrospective respiratory self-gating and removal of bulk motion in pulmonary UTE MRI of neonates and adults,” *Magn. Reson. Med.*, vol. 1295, no. March 2016, pp. 1284–1295, 2016.
[152] H. Seo, D. Kim, C. Oh, and H. Park, “Self-gated cardiac cine imaging using phase information,” *Magn. Reson. Med.*, vol. 1222, pp. 1216–1222, 2016.
[153] M. H. Moghari, R. Komarlu, D. Annese, T. Geva, and A. J. Powell, “Free-breathing steady-state free precession cine cardiac magnetic resonance with respiratory navigator gating,” *Magn. Reson. Med.*, vol. 73, no. 4, pp. 1555–1561, 2015.
[154] M. H. Moghari, T. Geva, and A. J. Powell, “Prospective heart tracking for whole-heart magnetic resonance angiography,” *Magn. Reson. Med.*, vol. 765, pp. 759–765, 2016.
[155] V. L. Granatstein, *Physical principles of wireless communications*, 2nd ed. Place of publication not identified: CRC Press, 2012.
[156] R. E. Kalman, “A New Approach to Linear Filtering and Prediction Problems,” *J. Basic Eng.*, vol. 82, no. 1, p. 35, 1960.
[157] M. Doyle, E. G. Walsh, G. G. Blackwell, and G. M. Pohost, “Block Regional Interpolation Scheme for k-Space (BRISK): A Rapid Cardiac Imaging Technique,” *Magn. Reson. Med.*, vol. 33, no. 2, pp. 163–170, 1995.
[158] T. Parrish and X. Hu, “Continuous Update with Random Encoding (CURE): A New Strategy for Dynamic Imaging,” *Magn. Reson. Med.*, vol. 33, no. 3, pp. 326–336, 1995.
[159] F. R. Korosec, R. Frayne, T. M. Grist, and C. A. Mistretta, “Time-resolved contrast-enhanced 3D MR angiography,” *Magn. Reson. Med.*, vol. 36, no. 3, pp. 345–351, 1996.
[160] R. P. Lim *et al.*, “3D time-resolved MR angiography (MRA) of the carotid arteries with time-resolved imaging with stochastic trajectories: Comparison with 3D contrast-enhanced bolus-chase MRA and 3D time-of-flight MRA,” *Am. J. Neuroradiol.*, vol. 29, no. 10, pp. 1847–1854, 2008.
[161] Z. P. Liang and P. C. Lauterbur, “An Efficient Method for Dynamic Magnetic Resonance Imaging,” *IEEE Trans. Med. Imaging*, vol. 13, no. 4, pp. 677–686, 1994.
[162] J. J. Van Vaals *et al.*, “‘Keyhole’ method for accelerating imaging of contrast agent uptake,” *J. Magn. Reson. Imaging*, vol. 3, no. 4, pp. 671–675, 1993.

[163] A. V. Barger, W. F. Block, Y. Toropov, T. M. Grist, and C. A. Mistretta, “Time-resolved contrast-enhanced imaging with isotropic resolution and broad coverage using an undersampled 3D projection trajectory,” *Magn. Reson. Med.*, vol. 48, no. 2, pp. 297–305, 2002.
[164] P. Kellman, F. H. Epstein, and E. R. Mcveigh, “Adaptive Sensitivity Encoding Incorporating Temporal Filtering (TSENSE),” *Magn Reson Med*, vol. 852, pp. 846–852, 2001.
[165] F. A. Breuer, P. Kellman, M. A. Griswold, and P. M. Jakob, “Dynamic autocalibrated parallel imaging using temporal GRAPPA (TGRAPPA),” *Magn. Reson. Med.*, vol. 53, no. 4, pp. 981–985, 2005.
[166] J. Tsao, P. Boesiger, and K. P. Pruessmann, “k-t BLAST and k-t SENSE: Dynamic MRI With High Frame Rate Exploiting Spatiotemporal Correlations,” *Magn. Reson. Med.*, vol. 50, no. 5, pp. 1031–1042, 2003.
[167] F. Huang, J. Akao, S. Vijayakumar, G. R. Duensing, and M. Limkeman, “K-t GRAPPA: A k-space implementation for dynamic MRI with high reduction factor,” *Magn. Reson. Med.*, vol. 54, no. 5, pp. 1172–1184, 2005.
[168] H. Pedersen, S. Kozerke, S. Ringgaard, K. Nehrke, and Y. K. Won, “K-t PCA: Temporally constrained k-t BLAST reconstruction using principal component analysis,” *Magn. Reson. Med.*, vol. 62, no. 3, pp. 706–716, 2009.
[169] M. Lustig, D. Donoho, and J. M. Pauly, “Sparse MRI: The application of compressed sensing for rapid MR imaging,” *Magn. Reson. Med.*, vol. 58, no. 6, pp. 1182–1195, 2007.
[170] D. Piccini, A. Littmann, S. Nielles-vallespin, and M. O. Zenge, “Spiral Phyllotaxis : The Natural Way to Construct a 3D Radial Trajectory in MRI,” vol. 1056, pp. 1049–1056, 2011.
[171] J. Y. Cheng *et al.*, “Free-breathing pediatric MRI with nonrigid motion correction and acceleration,” *J. Magn. Reson. Imaging*, vol. 42, no. 2, pp. 407–420, 2015.
[172] Y. Zhu, Y. Guo, S. G. Lingala, R. M. Lebel, M. Law, and K. S. Nayak, “GOCART: GOlden-angle CArtesian randomized time-resolved 3D MRI,” *Magn. Reson. Imaging*, vol. 34, no. 7, pp. 940–950, 2016.
[173] J. Liu and D. Saloner, “Accelerated MRI with CIRcular Cartesian UnderSampling (CIRCUS): a variable density Cartesian sampling strategy for compressed sensing and parallel imaging,” *Quant. Imaging Med. Surg.*, vol. 4, no. 1, pp. 57–67, 2014.
[174] T. Correia, G. Cruz, T. Schneider, R. M. Botnar, and C. Prieto, “Technical note: Accelerated nonrigid motion-compensated isotropic 3D coronary MR angiography,” *Med. Phys.*, vol. 45, no. 1, pp. 214–222, 2018.
[175] M. Lustig, J. M. Santos, D. Donoho, and J. M. Pauly, “k-t SPARSE: High frame rate dynamic MRI exploiting spatio-temporal sparsity,” *Proc. 14th Annu. Meet. Int. Soc. Magn. Reson. Med.*, vol. 50, no. 5, p. 2420, 2006.
[176] L. Feng *et al.*, “Highly accelerated real-time cardiac cine MRI using k-t SPARSE-SENSE,” *Magn. Reson. Med.*, vol. 70, no. 1, pp. 64–74, 2013.

[177] M. Saranathan, D. W. Rettmann, B. A. Hargreaves, S. E. Clarke, and S. S. Vasanawala, “DIfferential Subsampling With Cartesian Ordering (DISCO): A High Spatio-temporal Resolution Dixon Imaging Sequence for Multiphasic Contrast Enhanced Abdominal Imaging,” *J. Magn. Reson. Imaging*, vol. 1492, pp. 1484–1492, 2012.
[178] J. Y. Cheng *et al.*, “Comprehensive Motion-Compensated Highly-Accelerated 4D Flow MRI with Ferumoxytol Enhancement for Pediatric Congenital Heart Disease,” *J Magn Reson Imaging*, vol. 43, no. 6, pp. 1355–1368, 2017.
[179] J. Y. Cheng *et al.*, “Comprehensive Multi-Dimensional MRI for the Simultaneous Assessment of Cardiopulmonary Anatomy and Physiology,” *Sci. Rep.*, vol. 7, no. 1, pp. 1–15, 2017.
[180] L. Feng *et al.*, “5D whole-heart sparse MRI,” *Magn. Reson. Med.*, vol. 79, no. 2, pp. 826–838, 2018.
[181] D. Piccini *et al.*, “Four-dimensional respiratory motion-resolved whole heart coronary MR angiography,” *Magn. Reson. Med.*, vol. 77, no. 4, pp. 1473–1484, 2017.
[182] R. Bridson, “Fast Poisson Disk Sampling in Arbitrary Dimensions,” in *ACM SIGGRAPH 2007 Sketches*, 2007.
[183] F. Krahmer and R. Ward, “Stable and robust sampling strategies for compressive imaging,” *IEEE Trans. Image Process.*, vol. 23, no. 2, pp. 612–622, 2014.
[184] O. Bieri, M. Markl, and K. Scheffler, “Analysis and compensation of eddy currents in balanced SSFP,” *Magn. Reson. Med.*, vol. 54, no. 1, pp. 129–137, 2005.
[185] “BART Toolbox for Computational Magnetic Resonance Imaging.” .
[186] M. Uecker *et al.*, “ESPIRiT - An eigenvalue approach to autocalibrating parallel MRI: Where SENSE meets GRAPPA,” *Magn. Reson. Med.*, vol. 71, no. 3, pp. 990–1001, 2014.
[187] A. Bustin *et al.*, “Five-minute whole-heart coronary MRA with sub-millimeter isotropic resolution, 100% respiratory scan efficiency, and 3D-PROST reconstruction,” *Magn. Reson. Med.*, vol. 81, no. 1, pp. 102–115, 2019.
[188] R. Zhou *et al.*, “Free-breathing cine imaging with motion-corrected reconstruction at 3T using SPiral Acquisition with Respiratory correction and Cardiac Self-gating (SPARCS),” *Magn. Reson. Med.*, vol. 82, no. 2, pp. 706–720, 2019.
[189] F. Godenschweger *et al.*, “Motion correction in MRI of the brain,” *Phys. Med. Biol.*, vol. 61, no. 5, pp. R32–R56, 2016.
[190] C. Hutton *et al.*, “The impact of physiological noise correction on fMRI at 7 T,” *Neuroimage*, vol. 57, no. 1, pp. 101–112, Jul. 2011.
[191] D. Papp, S. H. F. Jaeschke, S. W. Rieger, S. Clare, and A. T. Hess, “Simultaneous detection of cardiac respiratory and rigid body head motion,” in *Proc. Intl. Soc. Mag. Reson. Med. 26*, 2018, p. 1168.
[192] J. G. Betts *et al.*, “Anatomy & Physiology,” 2017, p. 1335.